Investigation of local chemistry, orientation relationship and mechanical properties in martensitic Fe-Ni-C-(Si) steels

Von der Fakultät für Georessourcen und Materialtechnik der
Rheinisch-Westfälischen Technischen Hochschule Aachen

zur Erlangung des akademischen Grades eines

Doktors der Ingenieurwissenschaften

genehmigte Dissertation

vorgelegt von

Mattis Seehaus, M. Sc. RWTH

Berichter: Univ.-Prof. Dr. Sandra Korte-Kerzel
Univ.-Prof. Dr.-Ing. Hauke Springer

Tag der mündlichen Prüfung: 16.02.2024

Paper 1:
DOI: 10.1016/j.matdes.2023.111875
Materials & Design 229 (2023), 111875

Paper 2:
DOI: 10.3390/cryst13040663
Crystals 13 (2023), 663

Paper 3:
DOI: 10.1016/j.matdes.2023.112296
Materials & Design 234 (2023), 112296

D 82 (Diss. RWTH Aachen University, 2024)

Acknowledgments

An dieser Stelle möchte ich mich für die außerordentliche Mithilfe an der Ausfertigung der Doktorarbeit bei allen Beteiligten bedanken. Besonderer Dank gebührt dabei der Institutsdirektorin Frau Prof. Dr. S. Korte-Kerzel und der Nanostruktur-Fachgruppenleiterin Frau Dr.-Ing. S. Sandlöbes-Haut für die Bereitschaft mich auf diesem Weg zu unterstützen und die Promotion im Rahmen des Forschungsprojekts CTRAM (ANR-DFG 2018) möglich zu machen. Des Weiteren möchte ich mich für die vielen fachlichen Diskurse, die intensive Betreuung und auch die Korrekturrunden bedanken.
Die Finanzierung über die Dauer des Projekts wurde durch die Deutsche Forschungsgemeinschaft (DFG) ermöglicht, bei der ich mich ebenso bedanken möchte. Dadurch konnte ich mir ein fundiertes Wissen aneignen, mich persönlich weiterbilden und uneingeschränkt forschen.

Ein außerordentlicher Dank gilt unweigerlich allen Mitarbeitenden am Institut für Metallkunde und Materialphysik, die mir auf dem Weg zu meiner Dissertation durch lebhafte Diskussionen, motivierende Worte und auch ihre Verlässlichkeit stets geholfen haben. Dabei möchte ich besonders Risheng Pei und Fatim-Zahra Mouhib für ihre oft spontane Hilfe und Diskussionen hervorheben. Ebenso möchte ich mich bei meiner Bürokollegin Setareh Medghalchi und meinen Kollegen Kevin Bissa sowie Wassilios Delis und Maximilian Wollenweber bedanken, die immer für eine gute Atmosphäre, eine Vielzahl an Gesprächen und sportlicher Ablenkung durch Volleyball gesorgt haben. Zudem bedanke ich mich auch bei Doreen Andre und Martin Heller für die zahlreichen konstruktiven Wortwechsel und Hilfestellungen. Ich möchte mich ebenso bei meinen Hilfswissenschaftler/-innen Marlies Reher und Sang-Hyeok Lee für ihre tatkräftige Unterstützung bedanken.
Desweiteren gilt mein Dank auch Matthias Loeck, Sergey Laiko, Arndt Ziemons, David Beckers, Thomas Burlet und dem Team der mechanischen Werkstatt für die Unterstützung hinsichtlich Softwares und Technik, Metallopgrahie, Probenvorbereitung und Sicherheitsaspekten, wodurch ein reibungsfreier und optimal bedingter Ablauf ermöglicht werden konnte.
Zuletzt möchte ich mich insbesondere bei meiner Freundin, Annika Meuser, meiner und ihrer Familie für die abseits des wissenschaftlichen Bereichs stattgefundene Unterstützung bedanken, die mir während der Promotionszeit entgegebengebracht wurde.

Vielen Dank euch allen!

Declaration on publications

This thesis includes the following research articles that have been published in international peer-reviewed journals:

Publication 1: *"Influence of Si on the microstructure and C redistribution in martensitic steels"* **Seehaus, M.** and Korte-Kerzel, S. and Sandlöbes-Haut, S.
Materials & Design, vol. 229, 2023 [1]

Publication 2: *"Orientation relationship of FeNiC and FeNiCSi from variant detection in EBSD data"* **Seehaus, M.** and Pei, R. and Korte-Kerzel, S. and Sandlöbes-Haut, S.
Crystals, vol. 13, no. 4, 2023 [2]

Publication 3: *"Estimation of directional single crystal elastic properties nano-indentation by correlation with EBSD and first-principle calculations"* **Seehaus, M. and Lee, S.-H.** and Stollenwerk, T. and Wheeler, J.M. and Korte-Kerzel, S.
Materials & Design, vol. 234, 2023 [3]

Table of Contents

List of Figures

List of Tables

List of Abbreviations

α'	(lencticular) martensite
APT	Atom probe tomography
B	Bain
bcc	Body-centered cubic
bct	Body-centered tetragonal
BSE	Backscattered electron imaging
C	Carbon
CCE	Constrained carbon equilibrium
CRSS	Critical resolved shear stress
DFT	Density functional theory
EBSD	Electron backscatter diffraction
EDS	Energy-dispersive X-ray spectroscopy
fcc	Face-centered cubic
Fe	Iron
FIB	Focused ion beam
FLAPW	Full-potential linearised augmented plane-wave
γ	Austenite
GT	Greninger-Troiano
GGA	Generalized gradient approximation
HK	Hohenberg-Kohn theorem
HR-TEM	High-resolution transmission electron microscopy
KS	Kurdjumov-Sachs
LDA	Local density approximation

Mn	Manganese
MD	Molecular dynamics
M_S **temperature**	Martensite start temperature
Ni	Nickel
ND	Normal direction
NW	Nishiyama-Wasserman
OR	Orientation relationship
P	Pitsch
PAW	Projector augmented wave
PBE	Perdew-Burke-Ernzerhof
PF	Pole figure
RD	Rolling direction
RT	Room temperature
SAD	Selective area diffraction
SEM	Scanning electron microscopy
Si	Silicon
STEM	Scanning transmission electron microscopy
TD	Transverse direction
TEM	Transmission electron microscopy
TKD	Transmission Kikuchi diffraction
TB	Twin boundary
VASP	Vienna Ab-Initio Package
VN	Vlassak and Nix
XRD	X-ray diffraction

Zusammenfassung

In Stählen ist die martensitische Phasenumwandlung eine der bekanntesten Umwandlungen aufgrund ihres Beitrags in der Entwicklung der modernen Stahlindustrie. Diese findet von einer kubisch-flächenzentrierten Hochtemperaturphase, dem Austenit, in eine metastabile kubisch-raumzentrierte Niedrigtemperaturphase, den Martensit, statt. Insbesondere in der industriellen Verarbeitung von Stählen ist die martensitische Phasenumwandlung von entscheidender Bedeutung, da die Festigkeit des Werkstoffs davon determiniert wird. Trotz zahlreicher Studien sind die detaillierten Vorgänge während dieser Phasenumwandlung und jeweilige Orientierungsbeziehungen zwischen den Phasen jedoch noch nicht vollends verstanden.

Zu Beginn der Arbeit wird der Einfluss von Silizium auf die Kohlenstoffumverteilung in martensitischen Stählen bei einer Alterungszeit von 2 Jahren untersucht. Dabei wurden Proben zur Hälfte in flüssigem Stickstoff abgeschreckt, um die Orientierungsbeziehung zwischen Austenit und Martensit nach der Martensitumwandlung noch untersuchen zu können. Im Vergleich der beiden Legierungen Fe-24wt%Ni-0.4wt%C und Fe-24wt%Ni-0.4wt%C-2wt%Si führte der Siliziumeinfluss zu kleineren, initialen Austenitkörnern und demzufolge auch kleineren Martensitlamellen, hatte aber keine größere Auswirkung auf das c/a-Verhältnis des Martensitgitters. Bei den Ergebnissen der Atomsondentomographie zeigte sich ein unterschiedliches Segregationsverhalten im Grenzphasengebiet zwischen Austenit und Martensit. In der Legierung ohne Silizium reicherte sich Eisen im Martensit leicht an, während Nickel und Kohlenstoff abnahmen. Dieser Trend zeigte sich hingegen in der Legierung mit Silizium nicht, wo lediglich innerhalb des Grenzphasengebiets eine Zunahme von Kohlenstoff und Nickel bzw. ein sigmoidales Verhalten von Silizium beobachtet werden konnten. In Korrelation mit transmissionselektronmikroskopischen Aufnahmen zeigte sich, dass sich Kohlenstoff-Cluster entlang feiner {112}<111> Zwillingsgrenzen im Martensit ausgebildet haben. Die Determinierung der vorherrschenden Orientierungsbeziehung zwischen Martensit und Austenit wurde anhand von Elektronenrückstreubugungsaufnahmen ermittelt.

Dazu wurde ein auf der MTEX toolbox basierender Matlab Code entwickelt, der verschiede Untersuchungsmodi bietet. In transmissionselektronenmikroskopischen Untersuchungen können nur einzelne, individuelle Orientierungsbeziehungen analysiert werden, wohingegen mit Elektronenrückstreubugungsaufnahmen statistische Messungen an einer Vielzahl an Körnern möglich sind. Im Vergleich der resultierenden Polfiguren und auf Basis von theoretisch erzeugten Polfiguren bereits gefundener Orientierungsbeziehungen aus der Literatur konnte sowohl durch einen Bildvergleichsalgorithmus als auch Rotationswinkelabweichung und Misorientierungswinkelverteilung die Hauptorientierungs-

beziehung zu Greninger-Troiano festgestellt werden.
Des Weiteren wird ein zweistufiger Optimierungsprozess für die Abschätzung des Einkristallsteifigkeitstensors aus dem Eindringmodul vorgestellt, was durch eine korrelative, multiskalige Analyse möglich gemacht wurde, die Ergebnisse auf Basis von first-principle Berechnungen und Nanoindentationsexperimenten mit Charakterisierungsmethoden, wie SEM, EDS oder EBSD kombiniert. Die Möglichkeiten und Grenzen wurden dabei anhand von rein austenitischem FeNiC-Stahl und einem mehrphasigen Seymchan Meteoriten untersucht. Es konnte hierbei gezeigt werden, dass die Vorhersage des winkelabhängigen Elastizitätsmoduls auf der Basis von entweder direkt DFT-simulierten oder experimentell ermittelten Steifigkeitstensoren möglich ist, sowie unterschiedliche Phasenbereiche in einem korrelierten Indentationsmodul-Härte-Orientierungs-Diagramm beobachtet werden konnten.

Abstract

In steels, martensitic phase transformation is one of the best known transformations due to its contribution in the development of the modern steel industry. It takes place from a face-centred cubic high-temperature phase, austenite, to a metastable body-centred cubic low-temperature phase, martensite. Especially in the industrial processing of steels, the martensitic phase transformation is of crucial importance, as it determines the strength of the material. Despite numerous investigations, the detailed processes during this phase transformation and the respective orientation relationships between the phases are not yet fully understood.

In this work, the influence of silicon (Si) on the carbon (C) redistribution in martensitic steels at an ageing time of 2 years is investigated. One half of each sample was quenched in liquid nitrogen in order to be able to investigate the orientation relationship between austenite and martensite after the martensitic transformation. In comparison of the two alloys Fe-24wt%Ni-0.4wt%C and Fe-24wt%Ni-0.4wt%C-2wt%Si, the Si influence led to smaller initial austenite grains and consequently smaller martensite lenses, but had no major effect on the c/a ratio of the martensite lattice. The results of the atom probe tomography (APT) showed a different segregation behaviour within the interface region between austenite and martensite. In the alloy without silicon, iron (Fe) enriched slightly in the martensite, while nickel (Ni) and C depleted. This trend was not observed in the alloy with Si, where only an increase of C and Ni and a sigmoidal behaviour of silicon could be observed within the interfacial region. Correlation with transmission electron micrographs showed that carbon clusters formed along fine {112}<111> twin boundaries in the martensite. The determination of the predominant orientation relationship between martensite and austenite was identified using electron backscatter diffraction patterns.

For this purpose, a Matlab code based on the MTEX toolbox was developed, which offers different modes of investigation. In transmission electron microscopy, only single, individual orientation relationships (ORs) can be analysed, whereas electron backscatter diffraction (EBSD) images allow statistical measurements on a large number of grains. In comparison of the resulting pole figures (PFs) and on the basis of theoretically generated PFs of ORs discovered in the literature, the main OR could be identified as Greninger-Troiano (GT) by means of an image comparison algorithm as well as rotation angle deviation and misorientation angle distribution.

Furthermore, a two-step optimisation process for the estimation of the single crystal stiffness tensor from the indentation modulus is presented, achieved by a correlative multiscale analysis combining results based on first-principle calculations and nanoindentation experiments with characterisation methods such as SEM, EDS or EBSD. The possibilities

and limitations were investigated using pure austenitic FeNiC steel and a multiphase Seymchan meteorite. It was shown that the prediction of the anglular dependent elastic modulus is possible on the basis of either directly DFT-simulated or experimentally determined stiffness tensors, and that different phase regions could be distinguished in a correlated indentation modulus-hardness orientation plot.

Chapter 1

Motivation and Objectives

Martensitic steels are used in many technical applications due to their high strength and excellent toughness. However, their mechanical properties can be strongly influenced by the distribution of C in the microstructure. The redistribution of C during heat treatment, deformation or ageing time can lead to significant changes in the microstructure and mechanical properties of martensitic steels. The study of C redistribution in martensitic steels is also crucial for the optimisation of heat treatment processes and the development of advanced steels with improved properties for long-term service.
In this work, the influence of Si on C redistribution in steels with lenticular martensite is elaborated by a multi-scale experimental approach that correlates the partitioning of alloying elements revealed by APT with the nanoscopic transmission electron microscopy (TEM) micrographs and analyses the orientation relationships based on the microstructural EBSD observations. Furthermore, a correlative multi-scale analysis by nano-indentation with combined EBSD measurement and first principle calculations, respectively, is presented using the initial austenitic microstructure and a multiphase Seymchan meteorite to estimate directional elastic single crystal properties. A general overview of the dissertation is illustrated in Figure 1.1 and the main research objectives are outlined below:

1. *How can advanced experimental techniques contribute to the understanding of orientation-dependent materials properties?*

2. *How can orientation relationships be identified and represented in the investigated materials based on EBSD measurements?*

3. *What influence does Si addition have on the microstructure before and after martensitic transformation as well as on the C redistribution?*

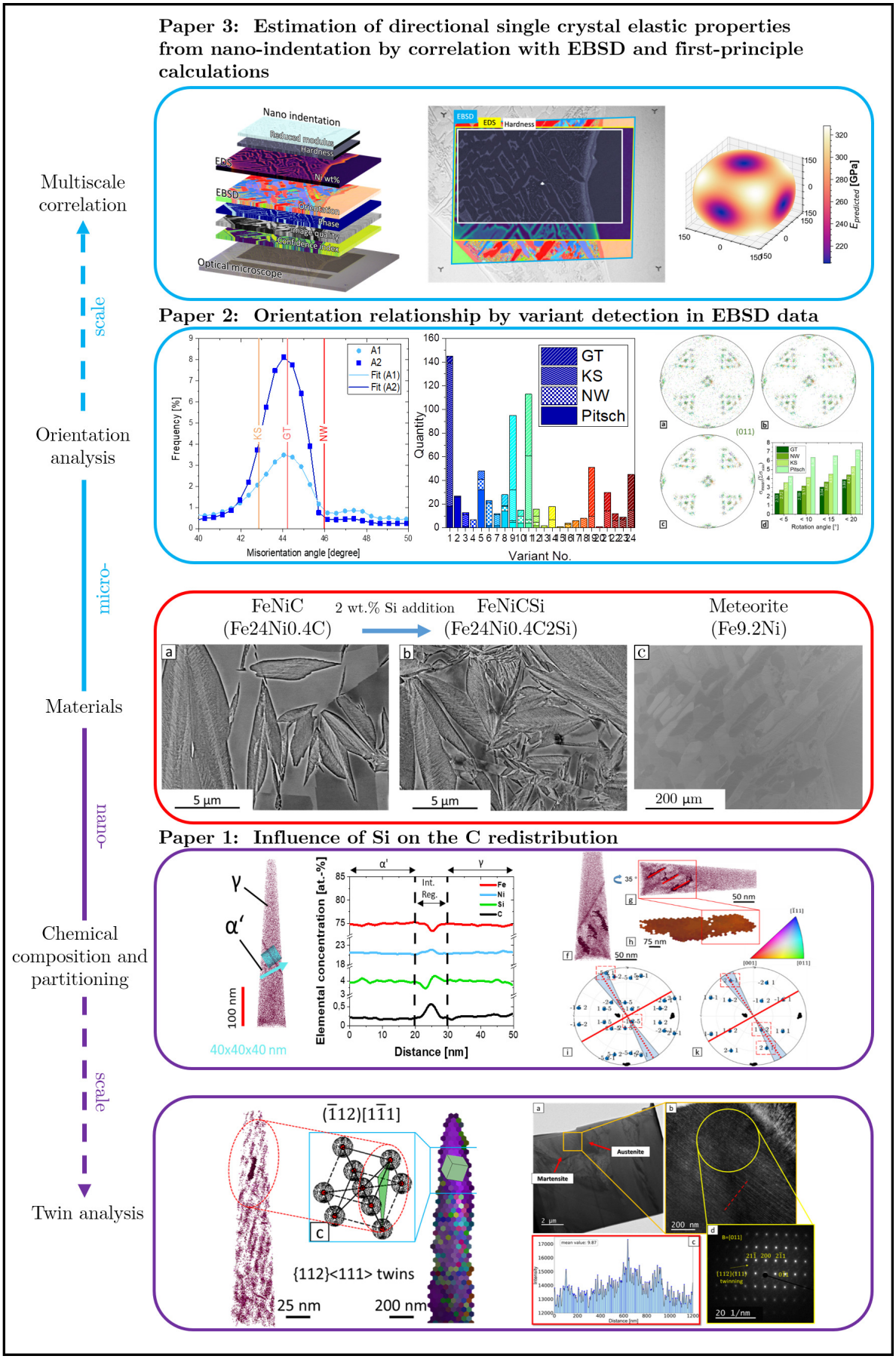

Figure 1.1: Graphical abstract of the dissertation.

Chapter 2

Materials & Methods

The materials used in this study were samples of martensitic steels, FeNiC and FeNiCSi, and a Seymchan meteorite. Table 2.1 represents the compositions of the materials.

Table 2.1: Chemical composition of the investigated materials from EDS.

	Fe [wt.-%]	Ni [wt.-%]	C [wt.-%]	Si [wt.-%]	Co [wt.-%]
FeNiC	76.33	22.74	0.93	-	1.04185
FeNiCSi	75.37	21.10	2.39	0.93	1.10755
Seymchan meteorite	90.02	9.2	-	-	0.78

The characterisation of the microstructure of these samples was carried out using different analytical techniques. First the specimens were prepared by polishing metallographically to a very fine surface in order to investigate the morphological features. Subsequently, the samples were examined using scanning electron microscopy (SEM) to investigate the grain structure, phase fractions and microstructural features within the martensite and meteorite. The microstructures were investigated in terms of their elemental composition and lattice parameters (c/a ratio of the martensite) by means of energy-dispersive X-ray spectroscopy (EDS) and X-ray diffraction (XRD). Further, backscattered electron imaging (BSE) was used to complement the results obtained from the other characterization techniques in order to provide additional insights into the microstructural features. The crystallographic orientations of the samples were investigated by EBSD and on a smaller scale by transmission Kikuchi diffraction (TKD) on TEM lamellae. Thereby, information about the orientation of the grains and the orientation relationships between the phases could be obtained. The material properties, such as hardness or Young's modulus, were determined on the basis of the nano-indentation method and correlated with the aforementioned characterisation methods and density functional theory (DFT). APT was used to study the composition of the samples at the atomic scale, which provided information about the distribution and concentration of the various elements present in the samples. Further nanoscale investigations were carried out using TEM, yielding insights on the crystallographic features, such as the formation of defects and nano-twins. Further details are described in the respective chapters or publications (Chapters 5 to 7).

Chapter 3

Fundamentals

In this chapter, the basic theory is briefly presented, covering the various martensite morphologies (Sec. 3.1), in particular lenticular martensite and its substructures, the general description of representation of microtexture data (Sec. 3.2) or orientation relationships (Sec. 3.3) and the interface between austenite and the transformed martensite in terms of variants (Sec. 3.4) or C redistribution (Sec. 3.5). Further, the fundamentals of first-principle calculations (Sec. 3.6) and nanoindentation (Sec. 3.7) are introduced.

3.1 Martensite formation

The martensitic transformation is characterised by the fact that the initial phase undergoes a structure and shape change induced by cooling or deformation, which takes place through successive nucleation by means of autocatalysis [18, 19]. In this diffusionless process the nuclei cannot cross high-angle boundaries during this displacive transformation and are therefore restricted to the grains in which they are formed [20, 21]. In this transformation process, the face-centered cubic (fcc) lattice of austenite (γ) changes into a body-centered cubic (bcc) lattice of martensite, which is tetragonally distorted depending on the carbon content [22]. Since no diffusion takes place, there is no change of position of individual atoms, but a coupled cooperative shear movement of groups of atoms. In this process, one atomic plane remains unrotated and undistorted, the so-called invariant habit plane [23]. The phase transformation from austenite to martensite occurs in FeNiCSi by quenching below 0 °C and leads to body-centered tetragonal (bct) (lencticular) martensite (α'). Figure 3.1 shows the theoretical axial c/a ratio in tetragonal martensite and the lattice parameter of austenite as a function of the C content in quenched C steels.

3.1.1 Morphology of martensite in ferrous alloys

The morphology of α'-martensite has different characteristics depending on the C content and the M_S temperature. In steels, lath, butterfly, plate, lenticular and thin plate martensite are known to occur, of which lath martensite forms at the highest temperatures, while thin plate martensite transforms at the lowest temperatures [7]. Figure 3.2 shows an example of the different martensite morphologies in ferrous alloys.

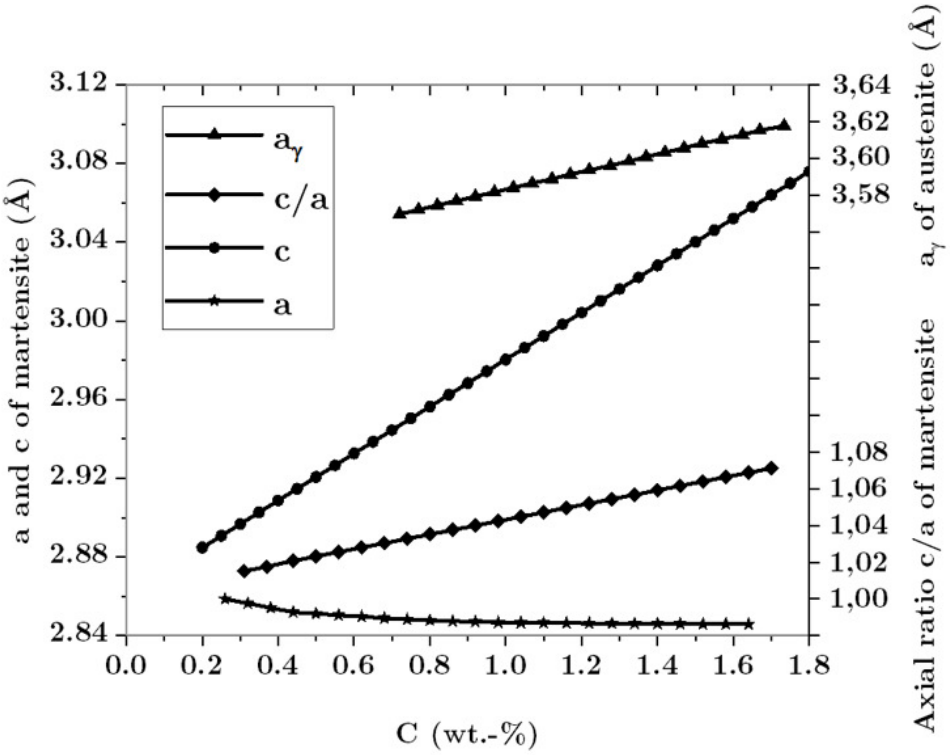

Figure 3.1: Lattice parameters a and c of austenite and tetragonal martensite in quenched C steels. (Redrawn from [4])

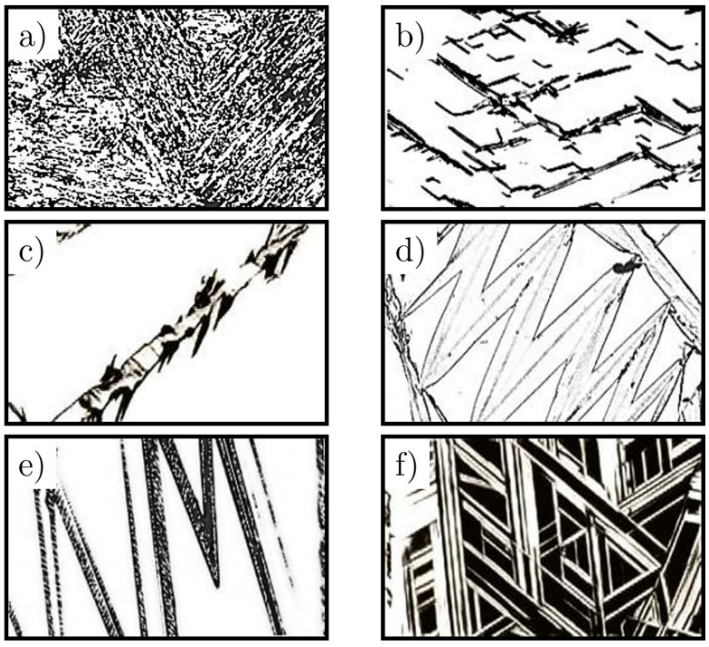

Figure 3.2: Various martensite morphologies in ferrous alloys. a) lath; b) butterfly; c) plate; d) lenticular; e) thin plate and f) ϵ martensite (Modified from [5])

Each of these morphologies has its own transformation temperature. Figure 3.3a) illustrates the martensite start temperature (M_S temperature) of martensite as a function of

C and Ni content in Fe-Ni-C alloys.

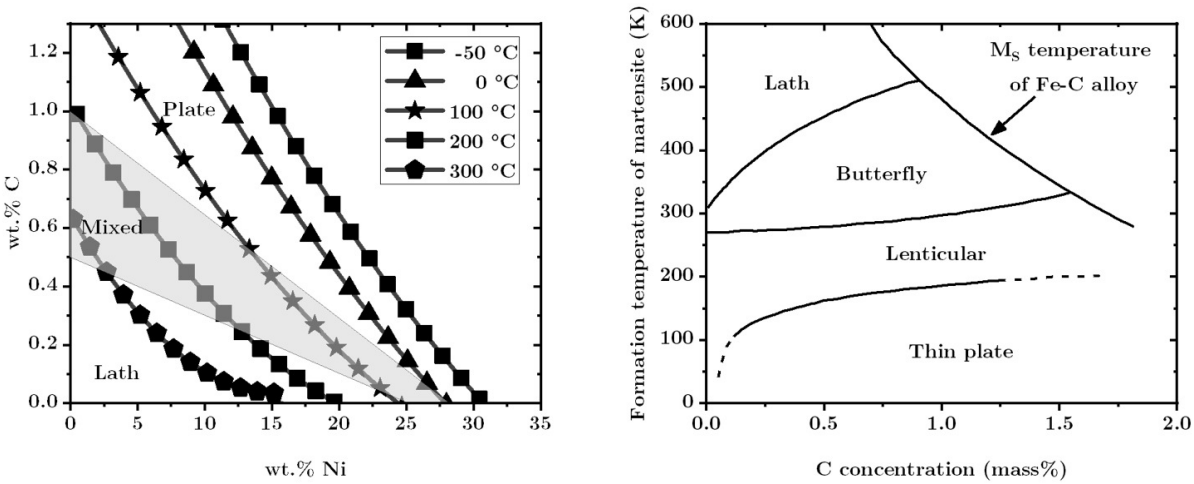

Figure 3.3: a) M_s temperatures and structure of FeNiC alloys in correlation to C and Ni content; b) Dependence of the formation temperature on the C concentration. (Redrawn from [6] and [7, 8]))

The α'-martensite morphology changes with decreasing M_S temperature from dislocated lath martensite to twinned thin-plate martensite, likewise the OR of lath martensite with nearly satisfying Kurdjumov-Sachs (KS) changes to Nishiyama-Wasserman (NW) and GT (see Sec. 3.3) of thin-plate martensite. Important factors determining the morphology and substructure of α' martensite are, in addition to the M_S temperature, the strengths of parent austenite and product martensite, the stacking fault energy of the austenite and the critical resolved shear stress (CRSS) for slip and twinning in the martensite [24–27]. Lath and lenticular are the two main morphologies of α'-martensite, with lath martensite being formed in most heat treatable steels and being of major industrial importance due to its high strength [28, 29]. In comparison to lath and thin plate martensite, the substructure and crystallography of lenticular martensite forming in an intermediate temperature range is very complex (Sec. 3.1.2).

3.1.2 Intricate morphology of lenticular martensite

Lenticular martensite reveals manifold zonal differences in its structure, whose details and formation are discussed in the following subchapters.

3.1.2.1 Micro- and substructure

In lenticular martensite, after impingement with an obstacle such as a grain boundary or other martensite plates, the formed martensite plate can nucleate a series of plates, probably as a result of stress concentrations due to the impingement. This burst transformation forms lenticular martensite in the form of a zigzag arrangement of plates (Figure 3.4).

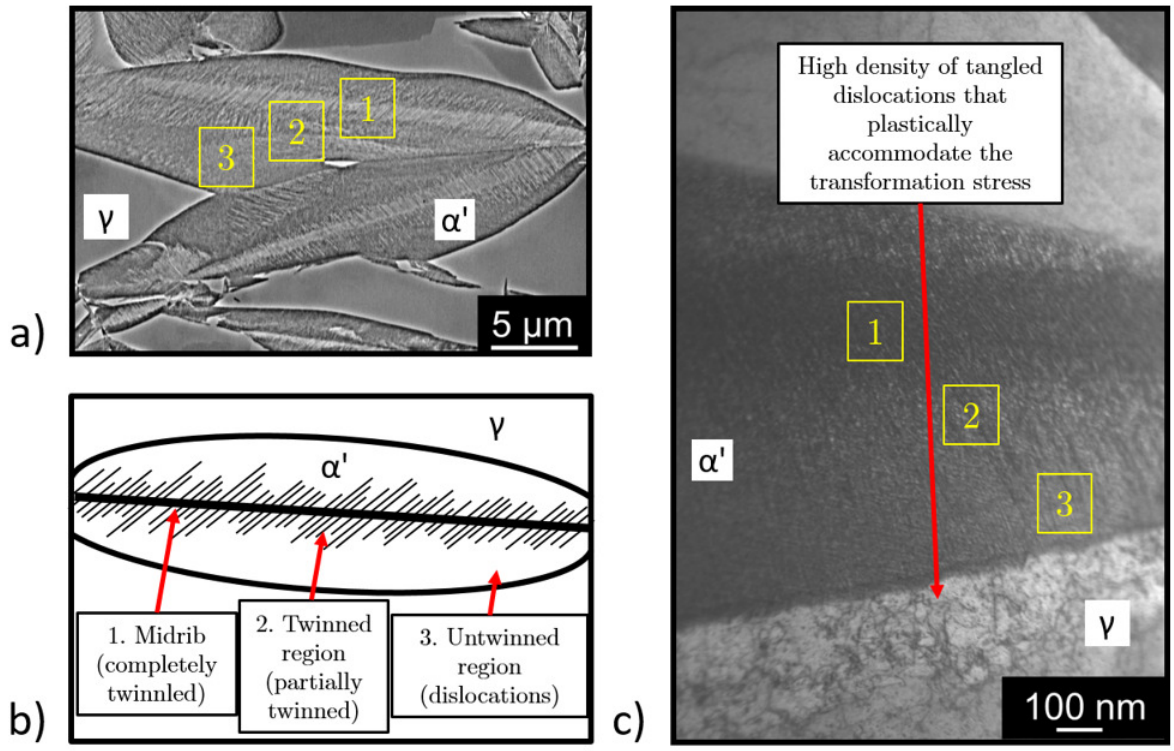

Figure 3.4: a) Substructure of lenticular martensite ovbserved by means of BSE; b) Schematic representation of the internal structure of lenticular martensite; c) FIB-STEM image showing a close-up of an interface area.

The straight line, which is technically a plane, is the initial part of a plate that is formed, the so-called "midrib" [30, 31]. However, because the α'/γ interface is not flat, it does not have a distinct habit plane. Therefore, the midrib plane is used to represent the habit plane of the lenticular martensite, lying in the proximity of $\{2\ 5\ 9\}_\gamma$ or $\{3\ 10\ 15\}_\gamma$ [26, 28]. The complex microstructure of lenticular martensite can principally be divided into three regions. Primarily, it consists of the central twinned midrib. Certain twins extend from the midrib into the surrounding second region, where they coexist with dislocations and in the third region there remains a high density of tangled dislocations [32–37].

3.1.2.2 Development of the α'-γ interface

In the midrib, partially twins grow at the onset and a series of screw dislocations form, which accompanies the formation of the twin region. These screw dislocations are subsequently dissociated from the transformation twins and are decomposed. The unwtinned region of lenticular martensite forms during plate growth due to the complete transition of lattice invariant deformation from twinning to slip, which is probably caused by an increasing local temperature resulting from latent heat during the martensite transformation [38]. The austenite near the α'/γ phase boundary also contains a high density

of entangled dislocations as a result of plastic deformation. These austenite dislocations probably resulted from slip deformation to accommodate the transformation strain and transitioned to the lenticular martensite adjacent to the phase boundary during growth [39]. The stages during the development of the lenticular martensite substructure are shown in Figure 3.5.

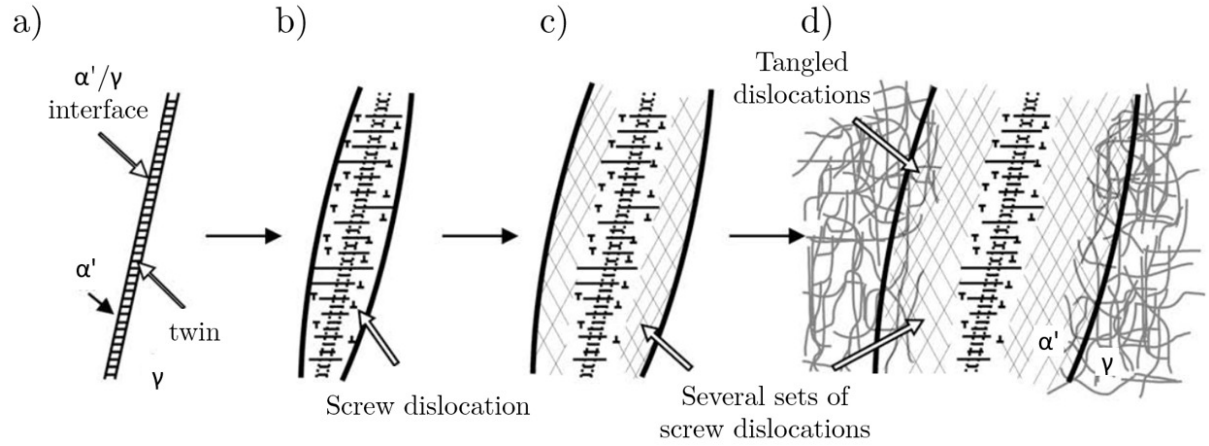

Figure 3.5: Illustration of the evolution of the substructure during the growth of lenticular martensite. a) midrib with high densitiy of transformation twins (twin plate martensite); b) partially twins grow in the midrib accompanied by screw dislocations; c) formation of untwinned region with screw dislocation sets; d) martensite inherits tangled and non-linear accomodation dislocations during growth from the parent austenite. (Adapted from [9])

3.2 Representation of microtexture data

The microtexture is composed of individual orientations that can be assigned to the position in a sample and that are usually obtained by an electron diffraction method such as EBSD. This leads to a very comprehensive and complex possibility for data evaluation and representation. The main objective is simply to represent and quantify the orientation distribution in a region of interest in the microstructure as a microtexture provides a direct correlation between orientation and microstructure. Typically, the collection of orientation data is accompanied by a record of the sample coordinates in the microstructure and the location of these individual orientation data points can then be represented in the form of PFs [10].

Usually the location of a pole projected from a reference sphere is characterised by two angles, α and β [40]. On the one hand, the angle alpha denotes the azimuth of the pole and, on the other hand, represents the north pole of the unit sphere at $\alpha = 0°$. The angle β, on the other hand, characterises the rotation of the pole around the polar axis Figure 3.6.

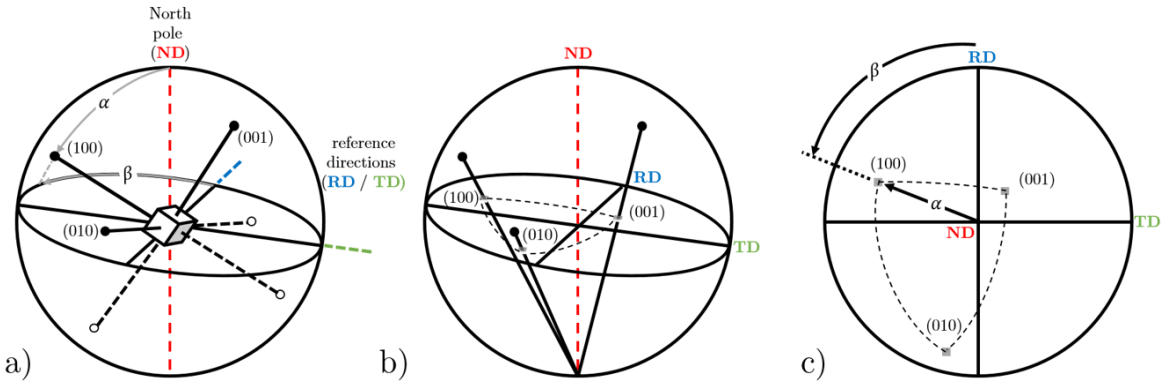

Figure 3.6: Illustration of the {100} poles in the stereographic projection of a cubic crystal. a) Crystal in the unit sphere and its intersections with the plane normals; b) Projections of the {100}-poles onto the equatorial plane; c) Definition of α and β according to the {100} pole figure. (Redrawn from [10])

According to the crystallographic orientation, the crystal is characterised in terms of the spatial distribution of the corresponding poles in relation to the angles α and β with respect to an external reference system, the sample coordinate system S. The crystal orientation, given by the axes of the crystal coordinate system $\mathrm{C} = \{c_1, c_2, c_3\}$, is projected into the reference frame S of the PF, given by the sample axes $\mathrm{S} = \{s_1, s_2, s_3\}$. Given that R is a vector parallel to a specific pole, it can be described in both coordinate systems S and C using (Eq. 3.1) and (Eq. 3.2).

$$R = s_1 \sin\alpha \cos\beta + s_2 \sin\alpha \sin\beta + s_3 \cos\alpha \qquad \text{(Eq. 3.1)}$$

$$R = \frac{1}{N}(c_1 X + c_2 Y + c3_Z) \qquad \text{(Eq. 3.2)}$$

where:

X,Y,Z = coordinates of the pole in the crystal frame
N = normalization factor $\sqrt{X^2 + Y^2 + Z^2}$

The transformation of the coordinate system of the crystal to the specimen coordinate system can be accomplished by a rotation of the crystal coordinate system through a single angle when this is carried out about a specific axis. In this context, the rotation angle and the axes of rotation are referred to as an axis-angle pair and are represented as an example <100>/50° misorientation axis/angle in Figure 3.7.
This orientation description allows the misorientation (between two grains of the same phase) or the OR (between different phases) to be characterised [41, 42]. In the former case, misorientation enables the grain boundary crystallography to be unravelled, which is a very important subset of microtexture [43]. A misorientation is thereby defined as a rotation matrix between two coordinate systems (Eq. 3.3) of e.g. two different grains.

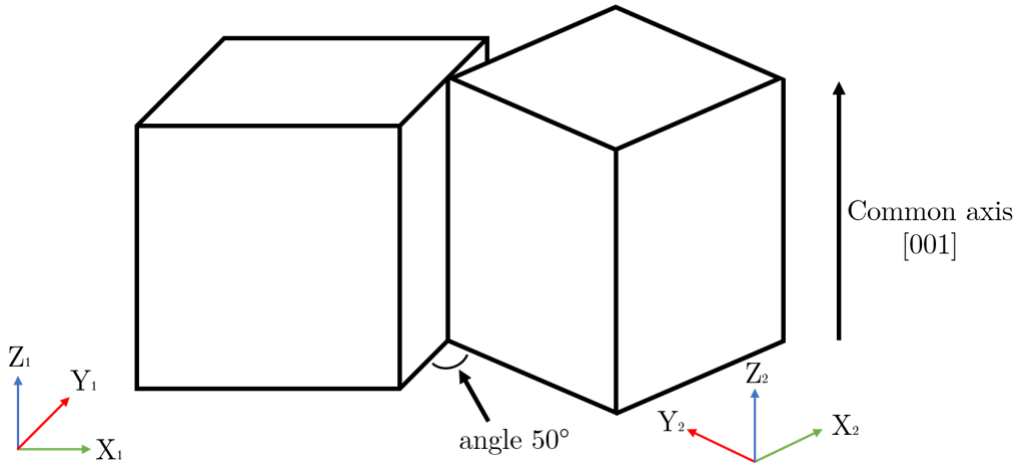

Figure 3.7: llustration of axis/angle of rotation between two cubes. (Redrawn after [10])

$$M_{12} = g_1^{-1} g_2 \qquad \text{(Eq. 3.3)}$$

where:

M_{12} = rotation Matrix between g_2 and g_1
g_1, g_2 = orientations of different grains with g_1 as arbitrary reference orientation

3.3 Orientation relationships

In austenitic steels the most common martensite types are the bcc α'- and the hexagonal-close packed ϵ-martensites, whereby experimental investigations have revealed that the austenite either transforms directly into one of the two aforementioned phases or eventually α'-martensite forms from the ϵ-martensite. The direct transformation into α'-martensite is most simply described by the model according to Bain (B) [44]. The model showed that the bcc structure of martensite is already contained in the fcc unit cell of austenite (Figure 3.8a). The bct unit cell undergoes compression in the [001] direction by about 20.63% and elongation by 12.25% in the [100] and [010] directions in order to yield the bcc martensite structure (Figure 3.8b).
However, the B model cannot explain the existence of an undistorted habit plane, as it can be easily shown that in the model each plane is subject to a shape change. Experimentally, the OR according to B was rarely observed. In contrast, the ORs according to NW [14] and KS [13] were frequently found in steels. The nature of these relationships is such that the close-packed plane of the γ lattice is parallel to that of the α' lattice and the close-packed direction of γ is parallel to that of α' (Figure 3.8c). Furthermore, it is parallel to the Burgers vector, which is physically significant. In addition, the less common Pitsch (P)

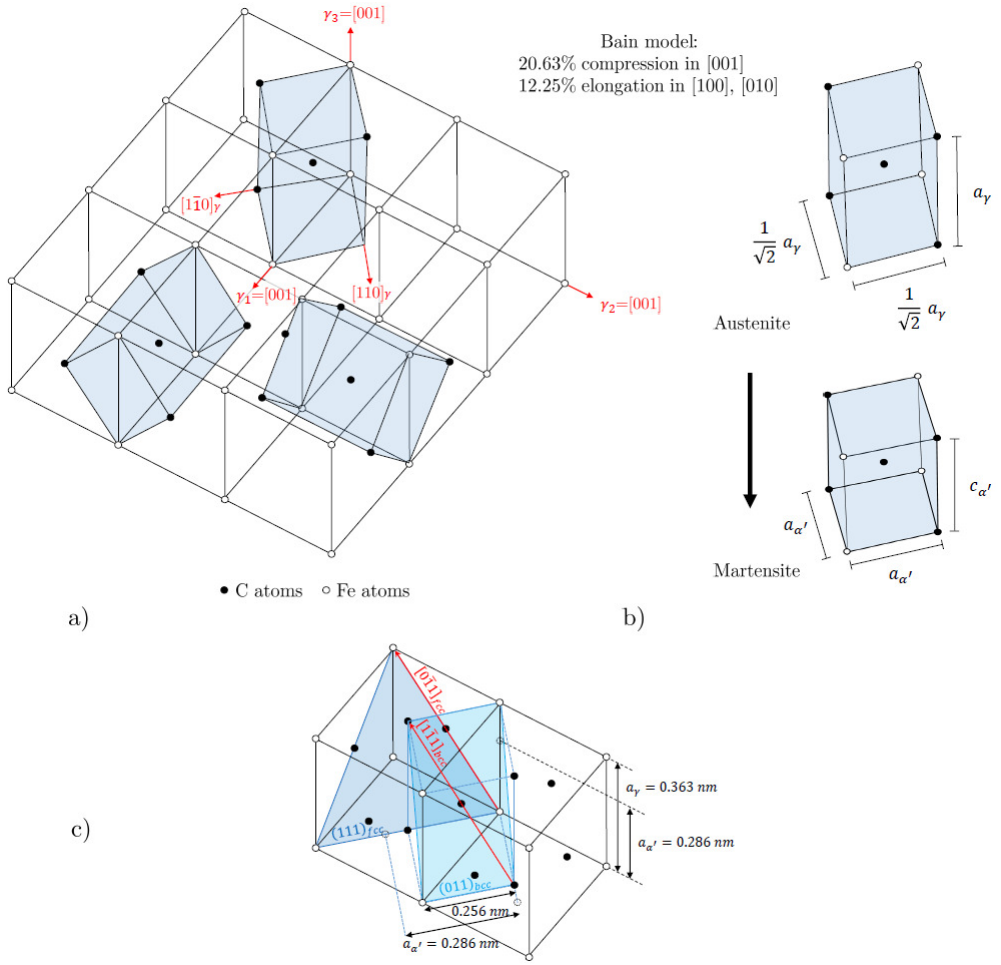

Figure 3.8: a) Martensitic variants b) Austenite to martensite transformation and c) schematic illustration of the Kurdjumov-Sachs orientation relationship. (Redrawn after [11] and [12])

[45] and GT ORs [46] have been observed in γ-α' transformations, which are presented with the other ORs and the number of variants (see Sec. 3.4) in Table 3.1.

Table 3.1: Overview of the most common orientation relationships between fcc and bcc crystals. Adapted from [11]

Name	Orientation relationship	Number of Variants	<uvw> ω_{min}
Bain (B)	$\{100\}_\gamma$ // $\{100\}_\alpha$ $< 100 >_\gamma$ // $< 110 >_\alpha$	3	<1 0 0> 45°
Kurdjumov-Sachs (KS)	$\{111\}_\gamma$ // $\{110\}_\alpha$ $< 110 >_\gamma$ // $< 111 >_\alpha$	24	<0.97 0.18 0.18> 42.85°
Nishiyama-Wasserman (NW)	$\{111\}_\gamma$ // $\{110\}_\alpha$ $< 112 >_\gamma$ // $< 110 >_\alpha$	12	<0.98 0.08 0.20> 45.98°
Pitsch (P)	$\{100\}_\gamma$ // $\{110\}_\alpha$ $< 110 >_\gamma$ // $< 111 >_\alpha$	12	<0.08 0.20 0.98> 45.98°
Greninger-Troiano (GT)	$\{111\}_\gamma$ // $\{110\}_\alpha$ $< 123 >_\gamma$ // $< 133 >_\alpha$	24	<0.97 0.19 0.13> 44.23°

3.4 Martensite variants

Displacive transformations are characterised by the fact that the child phase is not arbitrarily oriented in relation to the parent phase, but rather follows stringent crystallographic ORs. It implies that each parent grain can be transformed into a certain number of child crystal orientations, which are called variants of the transformation. The number of orientation variants varies depending on the OR. According to Kurdjumov and Sachs, the transformation of martensite is partitioned into two different shear deformations. Figure 3.9 shows three $(111)_\gamma$ planes, one above the other, which are differently packed in each atomic layer.

The arrows indicate the $[\bar{2}11]_\gamma$ shear directions along which the atoms of the second and third (111) atomic layers move. Atoms from the upper layer move up accordingly and cover the atoms from the lower layer from Figure 3.9a) marked in black along the shear direction (Figure 3.9b). A second shear along the $[1\bar{1}1]_\alpha$- and $[11\bar{1}]_\alpha$-direction leads to the final bcc-lattice (d). Based on the four slip planes (111), $(\bar{1}11)$, $(1\bar{1}1)$ and $(11\bar{1})$ and the respective shear directions depicted in Figure 3.10, 4×6 = 24 variants follow for the KS OR and 4×3 = 12 variants for the NW OR (also shown with the other ORs in Table 3.1).

In order to automatically, sequentially and statistically determine or analyse the identification of OR by the different occurring variants on the basis of EBSD data, a new

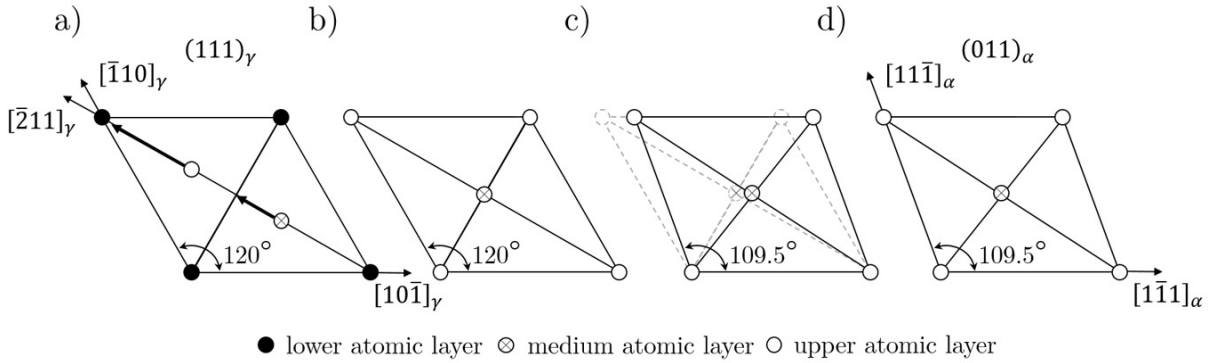

Figure 3.9: a) Schematic of the $\gamma - \alpha'$ transformation according to KS by b) atomic site change and c) shearing to d) α' martensite. (Redrawn from [13])

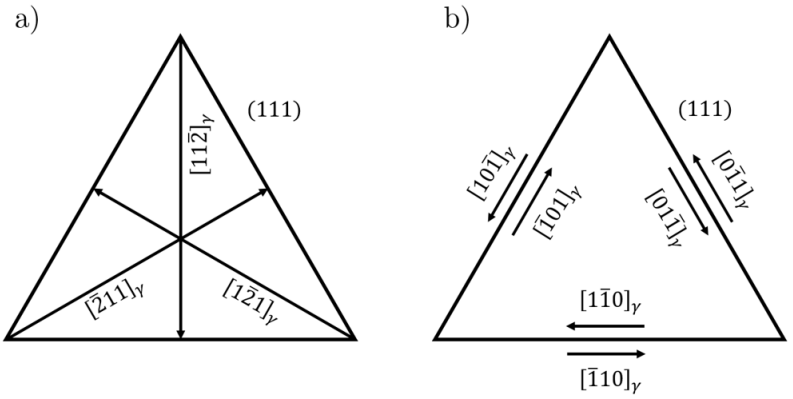

Figure 3.10: Illustration of the directions of shears on the $(111)_\gamma$ plane for a) N-W OR and b) K-S OR. (Redrawn from [14])

method was implemented in Matlab using the example of lenticular martensite and retained austenite and is presented in the following author's paper "**Orientation Relationship of FeNiC and FeNiCSi from Variant Detection in EBSD Data** [2]".

3.5 C Redistribution

In austenite, C atoms are randomly distributed on the interstitial sites of the fcc lattice, whereas in the transformed martensitic bcc lattice, a preferential distribution of C can occur. If this preferential distribution develops among the interstitial sites whose axes are parallel to each other, a general tetragonality can be observed. In the case of a random distribution of the C atoms on the interstitial sites, the tetragonality would disappear and a bcc martensite lattice would develop [47]. In medium and high C steels (0.3-1.5 wt% C), the martensite that forms is unstable at room temperature (RT) because the interstitial C atoms can diffuse into the bct martensite lattice [48]. In martensite, there are three octahedral sublattices of interstitial sites (see Figure 3.11) for C. If the C is only arranged in one of these sublattices, it is tetragonal and more stable or has a c/a

ratio >1 [49]. The order of the C atoms is dependent on both the temperature and the C concentration itself and can be estimated from the Zener temperature (Eq. 3.1). Above this temperature, the random distribution is in equilibrium, below this temperature a preferential distribution of C atoms takes place [47, 50, 51].

$$T_z = 1330 \cdot C \; in \; K \qquad \text{(Eq. 3.1)}$$

where:

T_z = critical Zener Temperature
C = carbon content in wt%

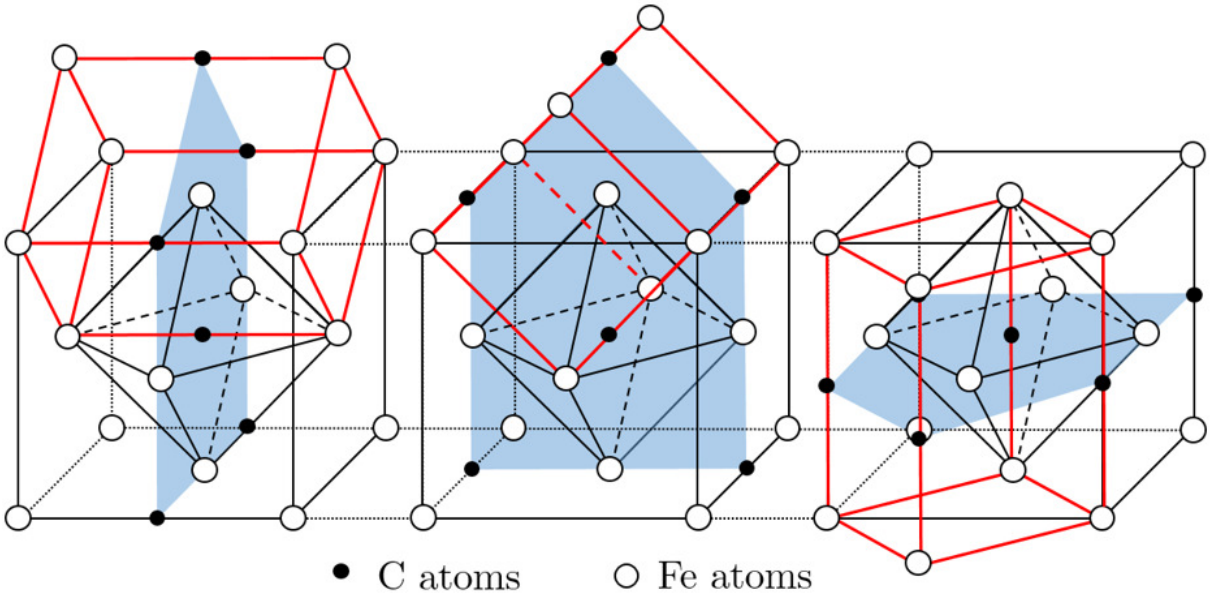

Figure 3.11: Schematic representation of the three different sublattices according to Zener for the ordered preferential carbon arrangement in the octahedral interstices. The resulting martensite is shown in red, while the blue area represents the carbon atoms marked in black along a specific sublattice. The white atoms represent iron.

The carbon partitioning from martensite to austenite is often described as controlled by the constrained carbon equilibrium (CCE) [52–54]. The CCE considers the lower mobility of iron and substitutional atoms during carbon diffusion at certain temperatures, as well as the immobility or stationarity of the martensite-austenite interface. As a result, only C undergoes equilibration of its chemical potential [55]. But the mechanism of carbon enrichment in the retained austenite is still controversial, as from a kinetic point of view temperatures lower than 300 °C seem too low for carbon diffusion [56]. The changes in phase fractions during the partitioning (determined by XRD and EBSD) suggest that for a CMnSiMo steel, the interface between martensite and austenite shifted towards the martensitic phase at 200, 300 and 400 °C, indicating a mobility of the α'/γ-interface

[57]. Previous studies have shown that carbon partitioning is influenced by the chemical potential gradient rather than the concentration gradient [58–60]. Although the carbon concentration in retained austenite and martensite is initially the same, carbon diffuses from the martensite with the higher chemical potential into the austenite with the lower potential until the carbon potential is balanced. It is assumed that the chemical potential of C in the α'/γ-interface is equal to maintain the continuity of the chemical potential. At the interface, the C partitioning can be described by (Eq. 3.2) using the diffusion coefficients of C in the austenite and martensite phases ((Eq. 3.4) and (Eq. 3.5)) [61]. The movement of atoms between the lattice positions of adjacent grains results in a movement of the interfaces of the microstructure. If the carbon contents at the interface deviate from the equilibrium concentrations of C for fcc and bcc at a given temperature, the phases experience a driving force towards the equilibrium phase composition. This driving force generates a local interfacial velocity at the interface (Eq. 3.3) [58, 59].

$$-D_C^{\alpha}\frac{dc^{\alpha}}{dz}\bigg|_{int} + \nu(c_{int}^{\gamma} - c_{int}^{\alpha}) = -D_C^{\gamma}\frac{dc^{\gamma}}{dz}\bigg|_{int} \qquad \text{(Eq. 3.2)}$$

where:

D_C^{α} = Diffusion coefficient of C in α $[m^2/s]$
D_C^{γ} = Diffusion coefficient of C in γ $[m^2/s]$
ν = interface migration velocity
c_{int}^{γ} = mole fraction of C in austenite
c_{int}^{α} = mole fraction of C in martensite

with:

$$\nu = (V_m)^{-1} M \cdot \overbrace{k\left(x_C^{\gamma-eq} - x_C^{\gamma}\right)}^{\Delta G} \qquad \text{(Eq. 3.3)}$$

where:

V_m = molar volume of iron
M = interface mobility $(3.36 \cdot 10^{-18} m^4 J^{-1} \cdot s^{-1})$
ΔG = driving force
k = constant of proportionality $(1021\ J \cdot wt.\%^{-1} \cdot mol^{-1}$

and with the diffusion coefficients of carbon in the austenite and martensite phases [61]:

$$D_C^{\gamma} = 2 \cdot 10^{-5} exp\left(\frac{-140000}{RT}\right) \quad \text{(Eq. 3.4)}$$

$$D_C^{\alpha} = 2 \cdot 10^{-6} exp\left(\frac{-10115}{T}\right) \cdot \exp\left\{0.5898\left[1 + \frac{2}{\pi}\arctan\left(1.4985 - \frac{15309}{T}\right)\right]\right\} \quad \text{(Eq. 3.5)}$$

where:

$x_C^{\gamma-eq}$ = equilibrium concentration of carbon in austenite
x_C^{γ} = concentration of carbon in austenite
R = ideal gas constant ($8.314\ J/K \cdot mol$)
T = absolute temperature $[K]$

The distribution of C in retained austenite during martensite tempering was investigated for the first time using APT [62, 63]. In studies on an Fe-25 wt%-Ni-0.4 wt%-C alloy where C partitioning was observed, the carbon depleted zone measured in the martensite was larger than a calculated zone (Figure 3.12). However, this is not indicative of an enhanced carbon diffusivity, since experimentally no increase in the C composition on the austenite side of the interface was observed. This C redistribution from martensite to austenite is described as mechanism of austenite enrichment [15].
Si is known to retard the precipitation of cementite in martensitic steels and thus to increase the C partitioning efficiency [55, 64]. An air-cooled compared to a water-quenched alloy with low C and Si content (Fe-0.06 wt.-% C-0.2 wt.-% Si-11.7 wt.-% Mn-2.9 wt.-% Al) exhibited a strong C enrichment attributed to short-range diffusion at a low cooling rate to maintain local equilibrium [65]. In a study of Fe-1wt.-% Mn-1wt.-% C-(2wt.-% Si) at 300 s and 200 °C, it became apparent that the absence of Si did not lead to a carbon distribution in the austenite and instead, decomposition of the austenite occured [66]. A DFT study at elevated temperatures suggested that the presence of Si reduces the diffusion rate of C at RT by decreasing diffusion pathways through repulsion and thereby obstructing the C at sites near Si atoms [67].
One major focus of the current (not yet published) studies is also the role of the interface on C redistribution during the rapid transformation from austenite to martensite. Therefore, kinetic Monte Carlo simulations of C redistribution during martensitic transformation are performed elsewhere within the CTRAM project. Within this thesis, the focus is on C segregation or redistribution and microstructural changes in martensitic steels due to Si influence using EBSD, TEM and APT, which is discussed in the following paper: "**Influence of Si on the microstructure and C redistribution in martensitic steels** [1]".

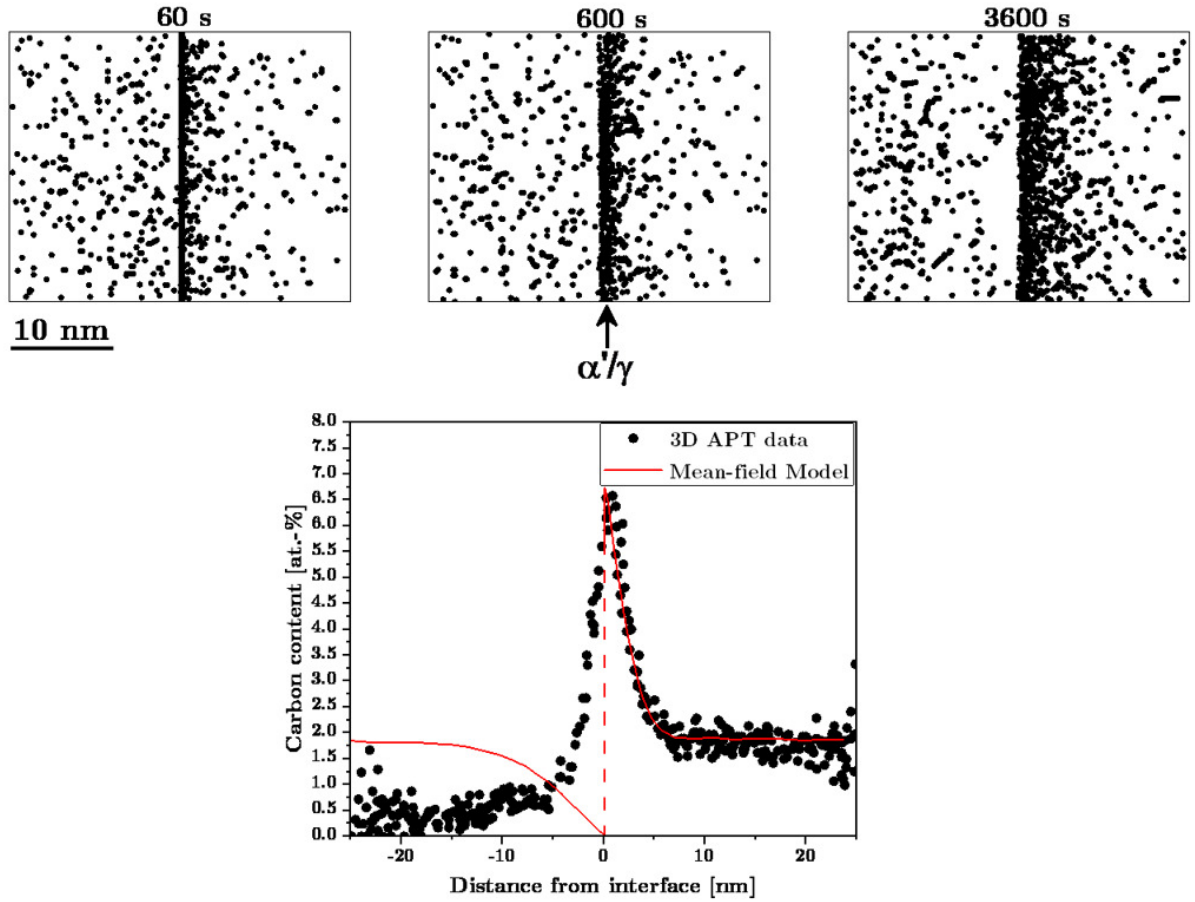

Figure 3.12: Partitioning of C atoms from martensite to austenite at 75 °C. a) Stochastic calculation at different times of the evolution of the C atom distribution (represented as black dots) in the vicinity of a α'/γ interface. b) Calculated and measured C profiles. (Redrawn after [15, 16])

3.6 First principles method

In order to investigate the ground state properties of matter, first principle calculations based on DFT serve as a computational method. Here, the Schrödinger equation is approximated by the Kohn-Sham equation [68] based on the Hohenberg-Kohn theorem (HK) [69]. One of the main advantages compared to other simulation methods, including molecular dynamics (MD), is that the DFT method requires only a reasonable estimation to reduce computational costs. The calculation uses the determined electronic structure to predict material properties such as band structures and elastic properties. The HK states that the knowledge of the ground state electron density uniquely determines the external potential. This also means that the ground state electron density further uniquely determines the ground state wave function and the ground state total energy as well as the other measured quantities. In non-relativistic Coulomb systems, the HK can be divided into three important aspects, according to which the total energy of the system

is composed of the functionals of the electron density (kinetic energy, electron-electron Coulombic repulsion, external potential) [70]. But calculations based on the entire set of electrons in the system are extremely computationally intensive. Since important chemical and physical phenomena mostly take place with the valence electrons, the electron density is smoothed to reflect the important physical properties of the real ionic nucleus [71].
The Vienna Ab-Initio Package (VASP) [72, 73] is a DFT simulation package that solves the quantum mechanical calculations using the well established pseudopotential by the projector augmented wave (PAW) method [74]. The PAW method combines the efficiency of the pseudopotential approach with the accuracy of the full-potential linearised augmented plane-wave (FLAPW) method [75]. The proper execution of simulations using the DFT method requires correct input parameters. Key input parameters that significantly affect the calculation results include the exchange correlation functional, energy cutoff, smearing method, spin polarization and the sigma value. The exchange correlation energy defines the difference between the true energy and the approximated functional, which significantly influences the simulation results [76]. Currently, several exchange correlation functionals are proposed. The simplest functional, called the local density approximation (LDA) [77], assumes that the exchange correlation functional depends only on the value of the local electron density. The generalized gradient approximation (GGA) is another example of a functional that has been extensively used [78, 79] and takes a local electron density as well as a local electron density gradient into account. To reduce the complexity of the calculation with the GGA method, the Perdew-Burke-Ernzerhof (PBE) method was introduced, which represents a simplified GGA method [80]. The smearing method and sigma value control the partial occupancies of the system, whereas the degree of spin orientation in a particular direction is controled by the spin polarization.

3.7 Nano-indentation

The development of new materials requires a detailed characterisation of their mechanical and functional properties on smaller scales. Here, nanoindentation has been established as an effective method for their evaluation [81–83]. By continuously measuring force or indentation load and displacement during indentation instead of measuring indent dimensions using optical methods as in conventional hardness testing, quantitative property values such as hardness and elastic modulus can be calculated [81, 84–87]. This instrumented nanoindentation combined with the Oliver-Pharr analysis has initiated the automated local measurement of mechanical properties [17]. Compared to other methods, nanoindentation offers a high spatial resolution for property mappings with minimal damage [88]. The Oliver-Pharr method is the prevalent analysis that approaches this complexity

by an approximated area function of the indenter tip that relates the contact depth to the projected contact area of the tip. In Figure 3.13a) a characteristic load-displacement response is represented.
Nevertheless, the underlying deformation mechanism using a Berkovich indenter is a combined result of elastic and plastic deformation, which is a limitation of the method. Here, the loading process is assumed to be elastic and plastic, while the unloading process is considered to be elastic. Based on the unloading slope S or also called contact stiffness, the Young´s modulus can be approximated.
Since the material sinks in around the indent, the measured depth is subdivided into the amounts of sinking depth and contact depth, resulting in equation (Eq. 3.1).

$$h_{max} = h_c + \overbrace{\epsilon \cdot \frac{P_{max}}{S}}^{h_S} \qquad \text{(Eq. 3.1)}$$

where:

h_{max} = maximum depth
h_c = contact depth
h_S = sink in depth
ϵ = constant depending on the indenter geometry
P_{max} = maximum load
S = contact stiffness

The hardness can then be determined by the maximum load and an area function dependent on the contact depth according to Equations (Eq. 3.2) and (Eq. 3.3).

$$H = \frac{P_{max}}{A} \qquad \text{(Eq. 3.2)}$$

$$A = f(h_c) \qquad \text{(Eq. 3.3)}$$

where:

H = hardness
A = contact area

The elastic modulus follows from its relationship to the measured unloading stiffness and to the contact area using (Eq. 3.4), where the effective elastic modulus takes into account that the indenter tip also deforms during indentation and follows (Eq. 3.5) with the respective elastic moduli and Poisson's ratios included.

$$S = \beta \cdot \frac{2}{\sqrt{\pi}} \cdot E_{eff} \cdot \sqrt{A} \qquad \text{(Eq. 3.4)}$$

$$\frac{1}{E_{eff}} = \frac{1-\nu^2}{E} + \frac{1-\nu_i^2}{E_i} \qquad \text{(Eq. 3.5)}$$

where:

β = correction factor for deviations in physical processes
E_{eff} = effective elastic modulus
E = material´s elastic modulus
E_i = indenter´s modulus
ν = material´s Poisson´s ratio
ν_i = indenter´s Poisson´s ratio

In common analytical methods for interpreting nanoindentation data in isotropic materials, the Young's modulus is assumed to be the polycrystalline average of the elastic constants. However, since many crystalline materials are anisotropic with respect to the elastic constants, Vlassak and Nix (VN) investigated the problem of a rigid indenter pressed into an elastic, anisotropic half-space. Specifically, their objective was to determine the interpretability of the results of a depth-sensitive indenter using zinc, copper and beta-brass as examples for samples with anisotropic elastic constants, which was validated by orientation-dependent hardness values obtained from nanoindentation experiments [89, 90].
It has been shown that nanoindentation can be a valid tool for measuring the mechanical properties of small grains (grain size <10 μm) within a composite matrix [91]. However, such a measurement has significant limitations, such as the need to compromise between having sufficient penetration depth to overcome surface roughness, but at the same time being shallow enough to only measure grain properties. It is difficult to visualise individual phases or to have suitable sample surfaces. To overcome these disadvantages, the grid indentation technique was developed, which can not only be used to obtain important mechanical properties of heterogeneous materials on a certain length scale, but also provides access to volume fractions of independent phases [91–93].
Publication 3 is based on this method and now enables an estimation of the basic elastic single crystal properties in a two-step optimisation procedure from the indentation modulus, it is entitled "**Estimation of directional single crystal elastic properties from nano-indentation by correlation with EBSD and first-principle calculations** [3]".

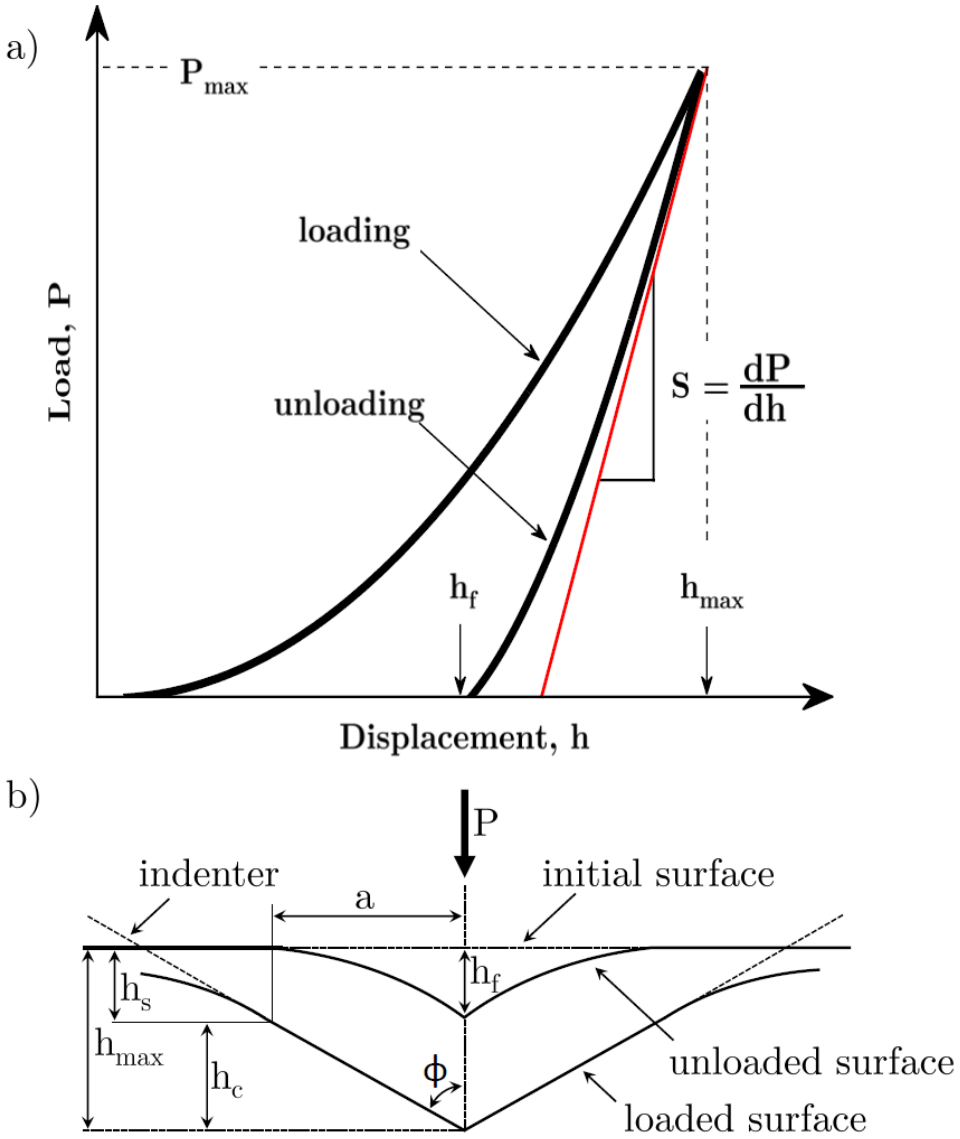

Figure 3.13: a) Characteristic load-displacement behaviour during nanoindentation using a Berkovich indenter; b) Schematic depiction of the unloading process, (where P=*load*, S=*contact stiffness*, h_{max}=*depth*, h_c=*contact depth*, h_c=*sink – in depth*, h_f=*final depth*). (Redrawn from [17]).

Chapter 4

Key insights and outlook

The following sections provide an overview of the main insights gained from this dissertation and explore potential further investigations.

4.1 Key insights

In this chapter the research questions adressed in Chapter 1 will be answered.

How can advanced experimental techniques contribute to the understanding of orientation-dependent materials properties?

The development of advanced materials is increasingly encompassing single components and focusing on smaller scales [94, 95]. In this respect, conventional methods have been extended to provide data at small scales and to combine different characterisation techniques. For example, orientation and chemical analyses in the SEM or first-principle and atomistic simulations as well as nanoindentation can provide new insights to enable multi-scale predictions and links to local properties [96–100]. In order to combine these measurement techniques and to make flexible, correlative analyses of the two-dimensional data sets, a comprehensive functionality library was developed in Python, whose possibilities and limitations were explored on the basis of initial pure austenitic FeNiC steel and a Seymchan meteorite (Figure 4.1). With respect to the research question, it could be shown that the prediction of the angular dependent elastic modulus based on either directly DFT-simulated or experimentally determined stiffness tensors is feasible as well as distinct regions of the respective phases in a correlated indentation modulus-hardness-EBSD plot could be observed (Chapter 7 and **Publication 3**).

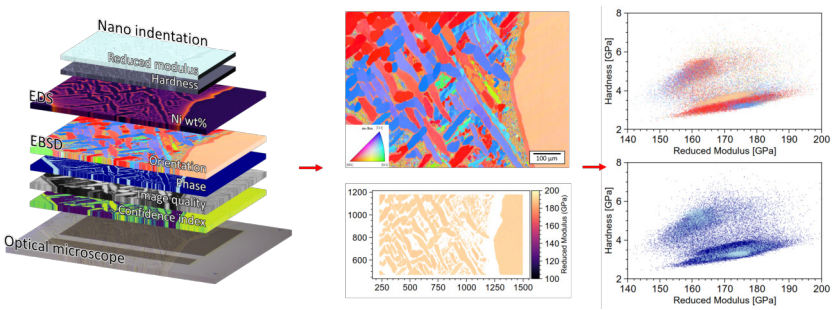

Figure 4.1: Graphical abstract for a combinatorial adaptive approach for the correlation of EBSD, BSE, nano-indentation, and first-principles simulation

How can orientation relationships be identified and represented in the investigated materials based on EBSD measurements?

In state-of-the-art applications with two, as in this case α' and γ, or multi-phase materials, the determination of ORs is of eminent importance [101, 102]. The steel samples investigated in this work were analysed statistically and automatically on the basis of EBSD data with regard to already confirmed and discovered ORs in the literature by means of a Matlab code specifically developed for this purpose (Figure 4.2). Compared to only locally obtained TEM analyses, which are not always feasible, this method also offers a statistical evaluation [39, 103–105]. In the case of the lenticular martensite and retained austenite containing steel samples, the Greninger-Troiano OR was proven to be the dominant OR (Chapter 6 and **Publication 2**).

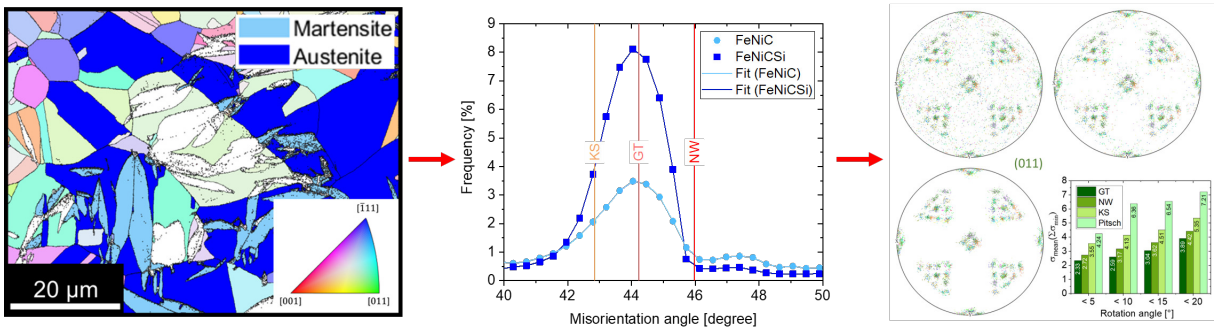

Figure 4.2: Graphical abstract for Orientation Relationship of FeNiC and FeNiCSi from Variant Detection in EBSD Data

What influence does Si addition have on the microstructure before and after martensitic transformation as well as on the C redistribution?

Since the martensitic structure of the quenched FeNiC(Si) steels and the associated carbon distribution are of fundamental interest for the technological material properties, the influence of Si on the carbon segregation was analysed for steels subsequent to 2 years of aging. C leads to a tetragonal distortion of the initial fcc austenite crystal structure and distributes among the interstitial octahedral lattice sites of the c-axis [106, 107]. The redistribution of C atoms has been investigated in various studies and revealed e.g. C segregation to coherent twin interfaces [108–139]. Besides characteristics that Si addition increases the amount of residual austenite and the upper temperature barrier for stable C clusters, the detailed effects of Si on C segregation are not yet fully known [140, 141]. Therefore, the influence of Si on the redistribution of C in the vicinity of γ/α' interfaces and twin boundaries was investigated using TEM and APT (Figure 4.3). It was found

that Si exhibits a sigmoidal distribution at the phase boundaries and acts as a barrier to C segregation into the austenite. In addition, it was also observed that stable C clusters formed at fine twin boundaries in the martensite, which inhibited carbide precipitation and correspondingly also partitioning into the austenite (Chapter 5 and **Publication 1**).

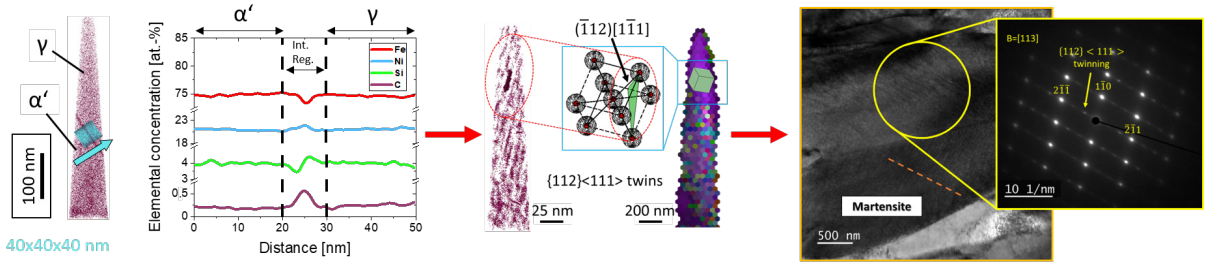

Figure 4.3: Graphical abstract for the influence of Si on the microstructure and C redistribution in martensitic steels

4.2 Outlook

In this dissertation, a multiscale analysis of FeNiC(Si) steels was conducted to investigate the effect of C redistribution in correlation with Si segregation on the martensite-austenite morphology and orientation relationships, which ultimately affect the technological material properties, and to enable the prediction of elastic properties. The study incorporates microstructure and OR examination, elastic properties prediction and nanoscale chemical distribution of C in relation to Si addition.

However, the current state of research still lacks statistical insights on solute-phase boundary interactions, thereby failing to grasp their complexity making precise property predictions impossible. Therefore, statistical investigation of the atomic Si or C distribution along whole grains should be performed in APT with correlative TEM measurements, and possible Si/C segregation anisotropies at different phase- and grain boundaries need to be extensively investigated by further APT and high-resolution transmission electron microscopy (HR-TEM) measurements.

In terms of statistical analysis of ORs a Matlab tool was developed. For further refinement of this method, the OR determination could be combined with concepts of parent grain reconstruction. In order to tackle the challenges of applying new material systems, this approach needs to be expanded to the detection of still unobserved ORs. Likewise, the method for estimating the single crystal elastic properties should be extended to other crystal systems, ultimately allowing reliable predictions of elastic properties in novel materials by calculating specific precompiled VN

parameters. The methods presented in this dissertation are currently still being extended.

Bibliography

[1] M. Seehaus, S. Korte-Kerzel, and S. Sandlöbes-Haut, "Influence of Si on the microstructure and C redistribution in martensitic steels," *Materials & Design*, 2023.

[2] M. Seehaus, R. Pei, S. Korte-Kerzel, and S. Sandlöbes-Haut, "Orientation relationship of FeNiC and FeNiCSi from variant detection in EBSD data," *Crystals*, vol. 13, no. 4, 2023.

[3] M. Seehaus, S.-H. Lee, T. Stollenwerk, J. M. Wheeler, and S. Korte-Kerzel, "Estimation of directional single crystal elastic properties from nano-indentation by correlation with EBSD and first-principle calculations," *Materials & Design*, p. 112296, 2023.

[4] K. Honda and Z. Nishiyama, "On the nature of the tetragonal and cubic martensites," *Science Reports of Tohoku Imperial University*, vol. 21, pp. 299–331, 1932.

[5] T. Maki, "Microstructure and mechanical behaviour of ferrous martensite," in *Materials Science Forum*, vol. 56, pp. 157–168, Trans Tech Publ, 1990.

[6] S. Allain, F. Danoix, M. Goune, K. Hoummada, and D. Mangelinck, "Static and dynamical ageing processes at room temperature in a Fe25Ni0.4C virgin martensite: Effect of C redistribution at the nanoscale," *Philosophical Magazine Letters*, vol. 93, pp. 68–76, 2013.

[7] T. Maki and I. Tamura, "Thin plate martensite in ferrous alloys and its various properties," *Bull. Jpn. Inst. Met.*, vol. 23, no. 4, pp. 229–237, 1984.

[8] T. Maki, *2 - Morphology and substructure of martensite in steels*, vol. 2, pp. 34–58. Woodhead Publishing, 2012.

[9] A. Shibata, S. Morito, T. Furuhara, and T. Maki, "Substructures of lenticular martensites with different martensite start temperatures in ferrous alloys," *Acta Materialia*, vol. 57, no. 2, pp. 483–492, 2009.

[10] V. Randle and O. Engler, *Introduction to texture analysis: macrotexture, microtexture and orientation mapping*. CRC press, 2000.

[11] K. Verbeken, L. Barbé, and D. Raabe, "Evaluation of the crystallographic orientation relationships between fcc and bcc phases in trip steels," *ISIJ international*, vol. 49, no. 10, pp. 1601–1609, 2009.

[12] S. Turteltaub and A. S. J. Suiker, "A multiscale thermomechanical model for cubic to tetragonal martensitic phase transformations," *International Journal of Solids and Structures*, vol. 43, no. 14, pp. 4509–4545, 2006.

[13] G. Kurdjumow and G. Sachs, "Über den Mechanismus der Stahlhärtung," *Zeitschrift für Physik*, vol. 64, no. 5, pp. 325–343, 1930.

[14] Z. Nishiyama, M. E. Fine, M. Meshii, and C. M. Wayman, *Martensitic transformation*. New York: Academic Press, 1978.

[15] M. Goune, F. Danoix, S. Allain, and O. Bouaziz, "Unambiguous carbon partitioning from martensite to austenite in Fe–C–Ni alloys during quenching and partitioning," *Scripta Materialia*, vol. 68, p. 1004–1007, 2013.

[16] P. Maugis and G. Martin, "Interface transfer coefficient in second-phase-growth models," *Physical Review B*, vol. 49, no. 17, p. 11580, 1994.

[17] W. C. Oliver and G. M. Pharr, "Measurement of hardness and elastic modulus by instrumented indentation: Advances in understanding and refinements to methodology," *Journal of materials research*, vol. 19, no. 1, pp. 3–20, 2004.

[18] J. R. C. Guimarães and J. C. Gomes, "A metallographic study of the influence of the austenite grain size on martensite kinetics," *Acta Metallurgica*, vol. 26, no. 10, pp. 1591–1596, 1978.

[19] V. Raghavan, "Formation sequence of plates in isothermal martensite transformation," *Acta Metallurgica*, vol. 17, no. 10, pp. 1299–1303, 1969.

[20] L. G.V.Kurdyumov, "On the "thermoelastic" equilibrium on martensitic transformations," *Journal of Technical Physics*, 1949.

[21] E. S. Machlin and M. Cohen, "Burst phenomenon in the martensitic transformation," *JOM*, vol. 3, no. 9, pp. 746–754, 1951.

[22] R. W. K. Honeycombe, "Steels microstructure and properties," *Metallurgy and materials science*, vol. 1, 1995.

[23] W. Dahl and A. I. für Eisenhüttenkunde, *Eigenschaften und Anwendungen von Stählen. 1. Grundlagen*. Verlag d. Augustinus-Buchh., 1993.

[24] R. Davies and C. Magee, "Influence of austenite and martensite strength on martensite morphology," *Metallurgical Transactions*, vol. 2, no. 7, pp. 1939–1947, 1971.

[25] M. Carr, J. Strife, and G. Ansell, "An investigation of the effects of austenite strength and austenite stacking fault energy on the morphology of martensite in Fe-Ni-Cr-0.3 C alloys," *Metallurgical Transactions A*, vol. 9, no. 6, pp. 857–864, 1978.

[26] G. Krauss and W. Pitsch, "Fine structure and habit planes of martensite in an iron-33 wt (nickel single crystal," in *Journal of Metals*, vol. 17, p. 1060, Minerals Metals Materials SOC 420 Commonwealth DR, Warrendale, PA 15086, 1965.

[27] T. Maki, S. Shimooka, M. Umemoto, and I. Tamura, "The morphology of strain-induced martensite and thermally transformed martensite in Fe–Ni–C alloys," *Transactions of the Japan Institute of Metals*, vol. 13, no. 6, pp. 400–407, 1972.

[28] R. Reed, "The plate-like martensite transformation in Fe-Ni alloys," *Acta Metallurgica*, vol. 15, no. 8, pp. 1287–1296, 1967.

[29] A. Marder, "The morphology of martensite in iron-carbon alloys," *Trans. ASM*, vol. 60, pp. 651–660, 1967.

[30] H. Neuhauser and W. Pitsch, "A new observation on the mechanism of martensitig transformations," *Acta Metallurgica*, vol. 19, no. 4, pp. 337–344, 1971.

[31] T. Kakeshita, K. Shimizu, T. Maki, and I. Tamura, "Growth behavior of lenticular and thin plate martensites in ferrous alloys and steels," *Scripta Metallurgica*, vol. 14, no. 10, pp. 1067–1070, 1980.

[32] J. C. Fisher, J. H. Hollomon, and D. Turnbull, "Kinetics of the austenite→martensite transformation," *JOM*, vol. 1, no. 10, pp. 691–700, 1949.

[33] M. A. Meyers, "On the growth of lenticular martensite," *Acta Metallurgica*, vol. 28, no. 6, pp. 757–770, 1980.

[34] R. F. Bunshah and R. F. Mehl, "Rate of propagation of martensite," *Trans. AIME*, vol. 197, 1953.

[35] R. E. Cech and D. Turnbull, "Heterogeneous nucleation of the martensite transformation," *JOM*, vol. 8, no. 2, pp. 124–132, 1956.

[36] T. Kakeshita, K. Kuroiwa, K. Shimizu, T. Ikeda, A. Yamagishi, and M. Date, "A new model explainable for both the athermal and isothermal natures of martensitic transformations in Fe-Ni-Mn alloys," *Materials Transactions, JIM*, vol. 34, no. 5, pp. 423–428, 1993.

[37] A. Shibata, S. Morito, T. Furuhara, and T. Maki, "Substructures of lenticular martensites with different martensite start temperatures in ferrous alloys," *Acta Materialia*, vol. 57, no. 2, pp. 483–492, 2009.

[38] R. L. Patterson and G. Wayman, "The crystallography and growth of partially-twinned martensite plates in Fe-Ni alloys," *Acta Metallurgica*, vol. 14, no. 3, pp. 347–369, 1966.

[39] A. Shibata, S. Morito, T. Furuhara, and T. Maki, "Local orientation change inside lenticular martensite plate in Fe–33Ni alloy," *Scripta Materialia*, vol. 53, no. 5, pp. 597–602, 2005.

[40] J. Hansen, J. Pospiech, and K. Lücke, *Tables for texture analysis of cubic crystals*. Springer, 1978.

[41] F. Lange, "Mathematical characterization of a general bicrystal," *Acta Metallurgica*, vol. 15, no. 2, pp. 311–318, 1967.

[42] A. t. Santoro and A. Mighell, "Coincidence-site lattices," *Acta Crystallographica Section A: Crystal Physics, Diffraction, Theoretical and General Crystallography*, vol. 29, no. 2, pp. 169–175, 1973.

[43] V. Randle and G. Laird, "A microtexture study of eutectic carbides in white cast irons using electron back-scatter diffraction," *Journal of materials science*, vol. 28, no. 15, pp. 4245–4249, 1993.

[44] E. C. Bain and N. Dunkirk, "The nature of martensite," *trans. AIME*, vol. 70, no. 1, pp. 25–47, 1924.

[45] W. Pitsch, "The martensite transformation in thin foils of iron-nitrogen alloys," *The Philosophical Magazine: A Journal of Theoretical Experimental and Applied Physics*, vol. 4, no. 41, pp. 577–584, 1959.

[46] A. B. Greninger and A. R. Troiano, "The mechanism of martensite formation," *JOM*, vol. 1, no. 9, pp. 590–598, 1949.

[47] C. Zener, "Kinetics of the decomposition of austenite," *Metals Technology*, 1945.

[48] G. Kurdjumov and A. Khachaturyan, "Phenomena of carbon atom redistribution in martensite," *Metallurgical Transactions*, vol. 3, pp. 1069–1076, 1972.

[49] H. Bhadeshia and R. Honeycombe, *Steels: microstructure and properties*. Butterworth-Heinemann, 2017.

[50] J. Fisher, J. Hollomon, and D. Turnbull, "Kinetics of the austenite→ martensite transformation," *JOM*, vol. 1, pp. 691–700, 1949.

[51] D. Hoffman, "Concerning the elastic free energy of dilute interstitial alloys," *Acta Metallurgica*, vol. 18, no. 7, pp. 819–833, 1970.

[52] J. Speer, D. K. Matlock, B. C. De Cooman, and J. Schroth, "Carbon partitioning into austenite after martensite transformation," *Acta materialia*, vol. 51, no. 9, pp. 2611–2622, 2003.

[53] J. Speer, D. Matlock, B. DeCooman, and J. Schroth, "Comments on "On the definitions of paraequilibrium and orthoequilibrium" by M. Hillert and J. Ågren, Scripta Materialia, 50, 697–9 (2004)," *Scripta Materialia*, vol. 52, no. 1, pp. 83–85, 2005.

[54] M. Hillert and J. Ågren, "On the definitions of paraequilibrium and orthoequilibrium," *Scripta Materialia*, vol. 50, no. 5, pp. 697–699, 2004.

[55] M. J. Santofimia, J. G. Speer, A. J. Clarke, L. Zhao, and J. Sietsma, "Influence of interface mobility on the evolution of austenite–martensite grain assemblies during annealing," *Acta Materialia*, vol. 57, no. 15, pp. 4548–4557, 2009.

[56] M. Santofimia, L. Zhao, and J. Sietsma, "Overview of mechanisms involved during the quenching and partitioning process in steels," *Metallurgical and Materials Transactions A*, vol. 42, pp. 3620–3626, 2011.

[57] G. A. Thomas and J. G. Speer, "Interface migration during partitioning of Q&P steel," *Materials Science and Technology*, vol. 30, no. 9, pp. 998–1007, 2014.

[58] B. Zhu, Z. Liu, Y. Wang, B. Rolfe, L. Wang, and Y. Zhang, "Application of a model for quenching and partitioning in hot stamping of high-strength steel," *Metallurgical and Materials Transactions A*, vol. 49, pp. 1304–1312, 2018.

[59] M. Santofimia, L. Zhao, and J. Sietsma, "Model for the interaction between interface migration and carbon diffusion during annealing of martensite–austenite microstructures in steels," *Scripta Materialia*, vol. 59, no. 2, pp. 159–162, 2008.

[60] Y. Wang, H. Geng, B. Zhu, Z. Wang, and Y. Zhang, "Carbon redistribution and microstructural evolution study during two-stage quenching and partitioning process of high-strength steels by modeling," *Materials*, vol. 11, no. 11, p. 2302, 2018.

[61] A. S. Nishikawa, M. J. Santofimia, J. Sietsma, and H. Goldenstein, "Influence of bainite reaction on the kinetics of carbon redistribution during the quenching and partitioning process," *Acta Materialia*, vol. 142, pp. 142–151, 2018.

[62] S. Barnard, G. Smith, M. Sarikaya, and G. Thomas, "Carbon atom distribution in a dual phase steel: An atom probe study," *Scripta Metallurgica*, vol. 15, no. 4, pp. 387–392, 1981.

[63] M. Sarikaya, A. Jhingan, and G. Thomas, "Retained austenite and tempered martensite embrittlement in medium carbon steels," *Metallurgical Transactions A*, vol. 14, pp. 1121–1133, 1983.

[64] J. Mola and B. C. De Cooman, "Quenching and partitioning (Q&P) processing of martensitic stainless steels," *Metallurgical and Materials Transactions A*, vol. 44, pp. 946–967, 2013.

[65] Y. Ma, B. Sun, A. Schoekel, W. Song, D. Ponge, D. Raabe, and W. Bleck, "Phase boundary segregation-induced strengthening and discontinuous yielding in ultrafine-grained duplex medium-Mn steels," *Acta Materialia*, vol. 200, pp. 389–403, 2020.

[66] B. Kim, J. Sietsma, and M. Santofimia, "The role of silicon in carbon partitioning processes in martensite/austenite microstructures," *Materials & Design*, vol. 127, 2017.

[67] D. Simonovic, C. K. Ande, A. I. Duff, F. Syahputra, and M. H. F. Sluiter, "Diffusion of carbon in bcc Fe in the presence of Si," *Physical Review B*, vol. 81, no. 5, p. 054116, 2010.

[68] W. Kohn and L. Sham, "Quantum density oscillations in an inhomogeneous electron gas," *Physical Review*, vol. 137, no. 6A, p. A1697, 1965.

[69] P. Hohenberg and W. Kohn, "Density functional theory (DFT)," *Phys. Rev*, vol. 136, no. 1964, p. B864, 1964.

[70] K. Capelle, "A bird's-eye view of density-functional theory," *Brazilian journal of physics*, vol. 36, pp. 1318–1343, 2006.

[71] E. Kaxiras and K. M. Rabe, *Atomic and Electronic Structure of Solids*, vol. 57. Cambridge University Press, 2004.

[72] G. Kresse and J. Furthmüller, "Efficiency of ab-initio total energy calculations for metals and semiconductors using a plane-wave basis set," *Computational materials science*, vol. 6, no. 1, pp. 15–50, 1996.

[73] G. Kresse and D. Joubert, "From ultrasoft pseudopotentials to the projector augmented-wave method," *Physical review b*, vol. 59, no. 3, p. 1758, 1999.

[74] P. E. Blöchl, "Projector augmented-wave method," *Physical review B*, vol. 50, no. 24, p. 17953, 1994.

[75] J. Hafner, "Ab-initio simulations of materials using VASP: Density-functional theory and beyond," *Journal of computational chemistry*, vol. 29, no. 13, pp. 2044–2078, 2008.

[76] E. Kiely, R. Zwane, R. Fox, A. M. Reilly, and S. Guerin, "Density functional theory predictions of the mechanical properties of crystalline materials," *CrystEngComm*, vol. 23, no. 34, pp. 5697–5710, 2021.

[77] D. M. Ceperley and B. J. Alder, "Ground state of the electron gas by a stochastic method," *Physical review letters*, vol. 45, no. 7, p. 566, 1980.

[78] G. I. Csonka, J. P. Perdew, A. Ruzsinszky, P. H. Philipsen, S. Lebègue, J. Paier, O. A. Vydrov, and J. G. Ángyán, "Assessing the performance of recent density functionals for bulk solids," *Physical Review B*, vol. 79, no. 15, p. 155107, 2009.

[79] P. Haas, F. Tran, P. Blaha, L. S. Pedroza, A. J. da Silva, M. M. Odashima, and K. Capelle, "Systematic investigation of a family of gradient-dependent functionals for solids," *Physical Review B*, vol. 81, no. 12, p. 125136, 2010.

[80] J. P. Perdew, K. Burke, and M. Ernzerhof, "Generalized gradient approximation made simple," *Physical review letters*, vol. 77, no. 18, p. 3865, 1996.

[81] W. C. Oliver and G. M. Pharr, "An improved technique for determining hardness and elastic modulus using load and displacement sensing indentation experiments," *Journal of materials research*, vol. 7, no. 6, pp. 1564–1583, 1992.

[82] J. Pethicai, R. Hutchings, and W. C. Oliver, "Hardness measurement at penetration depths as small as 20 nm," *Philosophical Magazine A*, vol. 48, no. 4, pp. 593–606, 1983.

[83] M. Doerner, D. Gardner, and W. Nix, "Plastic properties of thin films on substrates as measured by submicron indentation hardness and substrate curvature techniques," *Journal of Materials Research*, vol. 1, no. 6, pp. 845–851, 1986.

[84] J. Pethica and W. Oliver, "Mechanical properties of nanometre volumes of material: use of the elastic response of small area indentations," *MRS Online Proceedings Library (OPL)*, vol. 130, p. 13, 1988.

[85] J. Loubet, J. Georges, O. Marchesini, and G. Meille, "Vickers indentation curves of magnesium oxide (MgO)," *Journal of Tribology*, 1984.

[86] D. Newey, M. Wilkins, and H. Pollock, "An ultra-low-load penetration hardness tester," *Journal of Physics E: Scientific Instruments*, vol. 15, no. 1, p. 119, 1982.

[87] D. Stone, W. La Fontaine, P. Alexopoulos, T.-W. Wu, and C.-Y. Li, "An investigation of hardness and adhesion of sputter-deposited aluminum on silicon by utilizing a continuous indentation test," *Journal of Materials Research*, vol. 3, pp. 141–147, 1988.

[88] A. J. Bushby, "Nano-indentation using spherical indenters," *Nondestructive Testing and Evaluation*, vol. 17, no. 4-5, pp. 213–234, 2001.

[89] J. J. Vlassak and W. Nix, "Indentation modulus of elastically anisotropic half spaces," *Philosophical Magazine A*, vol. 67, no. 5, pp. 1045–1056, 1993.

[90] J. J. Vlassak and W. Nix, "Measuring the elastic properties of anisotropic materials by means of indentation experiments," *Journal of the Mechanics and Physics of Solids*, vol. 42, no. 8, pp. 1223–1245, 1994.

[91] N. X. Randall, M. Vandamme, and F.-J. Ulm, "Nanoindentation analysis as a two-dimensional tool for mapping the mechanical properties of complex surfaces," *Journal of materials research*, vol. 24, no. 3, pp. 679–690, 2009.

[92] C. Tromas, M. Arnoux, and X. Milhet, "Hardness cartography to increase the nanoindentation resolution in heterogeneous materials: Application to a Ni-based single-crystal superalloy," *Scripta Materialia*, vol. 66, no. 2, pp. 77–80, 2012.

[93] F.-J. Ulm, M. Vandamme, C. Bobko, J. Alberto Ortega, K. Tai, and C. Ortiz, "Statistical indentation techniques for hydrated nanocomposites: Concrete, bone, and shale," *Journal of the American Ceramic Society*, vol. 90, no. 9, pp. 2677–2692, 2007.

[94] J. Gong and A. J. Wilkinson, "A microcantilever investigation of size effect, solid-solution strengthening and second-phase strengthening for< a> prism slip in alpha-Ti," *Acta Materialia*, vol. 59, no. 15, pp. 5970–5981, 2011.

[95] W. C. Oliver and G. M. Pharr, "Nanoindentation in materials research: Past, present, and future," *Mrs Bulletin*, vol. 35, no. 11, pp. 897–907, 2010.

[96] H. Southworth, "Scanning electron microscopy and microanalysis," *Physicochemical Methods of Mineral Analysis*, pp. 421–450, 1975.

[97] M. Quaresimin, "Modelling the fatigue behaviour of bonded joints in composite materials," in *Multi-scale Modelling of Composite Material Systems*, pp. 469–494, Elsevier, 2005.

[98] Y. M. Arısoy, L. E. Criales, T. Özel, B. Lane, S. Moylan, and A. Donmez, "Influence of scan strategy and process parameters on microstructure and its optimization in additively manufactured nickel alloy 625 via laser powder bed fusion," *The International Journal of Advanced Manufacturing Technology*, vol. 90, pp. 1393–1417, 2017.

[99] T. Britton, H. Liang, F. Dunne, and A. Wilkinson, "The effect of crystal orientation on the indentation response of commercially pure titanium: experiments and simulations," *Proceedings of the Royal Society A: Mathematical, Physical and Engineering Sciences*, vol. 466, no. 2115, pp. 695–719, 2010.

[100] S. Das, F. Hofmann, and E. Tarleton, "Consistent determination of geometrically necessary dislocation density from simulations and experiments," *International Journal of Plasticity*, vol. 109, pp. 18–42, 2018.

[101] P. Asghari-Rad, M. Nili-Ahmadabadi, H. Shirazi, S. Hossein Nedjad, and S. Koldorf, "A significant improvement in the mechanical properties of AISI 304 stainless steel by a combined RCSR and annealing process: A significant improvement in the mechanical properties," *Advanced Engineering Materials*, vol. 19, 2016.

[102] J. Ren, C. Li, Y. Han, E. Li, C. Gao, and C. Qiu, "Effect of initial martensite and tempered carbide on mechanical properties of 3Cr2MnNiMo mold steel," *Materials Science and Engineering: A*, vol. 812, p. 141080, 2021.

[103] H. Sato and S. Zaefferer, "A study on the formation mechanisms of butterfly-type martensite in fe–30

[104] V. A. Yardley and E. J. Payton, "Austenite–martensite/bainite orientation relationship: characterisation parameters and their application," *Materials Science and Technology*, vol. 30, no. 9, pp. 1125–1130, 2014.

[105] G. Nolze, "Determination of orientation relationships between fcc/bcc lattices by the use of pole figures," *HKL Usermeeting*, pp. 1–9, 2004.

[106] G. V. Kurdjumov and A. G. Khachaturyan, "Nature of axial ratio anomalies of the martensite lattice and mechanism of diffusionless $\gamma \rightarrow \alpha$ transformation," *Acta Metallurgica*, vol. 23, no. 9, pp. 1077–1088, 1975.

[107] C. Zener, "Theory of strain interaction of solute atoms," *Physical Review*, vol. 74, pp. 639–647, 1948.

[108] K. Han, M. Van Genderen, A. Böttger, H. Zandbergen, and E. Mittemeijer, "Initial stages of Fe-C martensite decomposition," *Philosophical Magazine A*, vol. 81, no. 3, pp. 741–757, 2001.

[109] M. Hayakawa, M. Tanigami, and M. Oka, "Low temperature aging of the freshly formed martensite in an Fe-Ni-C alloy," *Metallurgical Transactions A*, vol. 16, no. 10, pp. 1745–1750, 1985.

[110] B. Kim, J. Sietsma, and M. Santofimia, "Thermodynamic aspects of carbon redistribution during ageing and tempering of Fe–Ni–C alloys," *Philosophical Magazine*, vol. 96, no. 25, pp. 2632–2648, 2016.

[111] M. Miller, P. Beaven, S. Brenner, and G. Smith, "An atom probe study of the aging of iron-nickel-carbon martensite," *Metallurgical Transactions A*, vol. 14, no. 6, pp. 1021–1024, 1983.

[112] S. Nagakura, Y. Hirotsu, M. Kusunoki, T. Suzuki, and Y. Nakamura, "Crystallographic study of the tempering of martensitic carbon steel by electron microscopy and diffraction," *Metallurgical Transactions A*, vol. 14, no. 6, pp. 1025–1031, 1983.

[113] R. Naraghi, M. Selleby, and J. Ågren, "Thermodynamics of stable and metastable structures in Fe–C system," *Calphad*, vol. 46, pp. 148–158, 2014.

[114] G. Olson and M. Cohen, "Early stages of aging and tempering of ferrous martensites," *Metallurgical Transactions A*, vol. 14, no. 6, pp. 1057–1065, 1983.

[115] S. Ren, T. Tadaki, K. Shimizu, and X. Wang, "Electron diffraction study of aging processes in Fe-1.83 wt pct C martensite at room temperature," *Metallurgical and Materials Transactions A*, vol. 26, no. 8, pp. 2001–2005, 1995.

[116] K. Taylor, l. Chang, G. Olson, G. Smith, M. Cohen, and J. Sande, "Spinodal Decomposition During Aging of Fe—Ni—C Martensites," *Metallurgical Transactions A*, vol. 20, pp. 2717–2737, 1989.

[117] K. Taylor, G. Olson, M. Cohen, and J. Vander Sande, "Carbide precipitation during stage I tempering of Fe-Ni-C martensites," *Metallurgical Transactions A*, vol. 20, no. 12, pp. 2749–2765, 1989.

[118] K. Ullakko, V. Gavriljuk, and V. Nadutov, "Aging of freshly formed Fe-based martensites at low temperatures," *Metallurgical and Materials Transactions A*, vol. 25, no. 5, pp. 889–909, 1994.

[119] M. Van Genderen, M. Isac, A. Böttger, and E. Mittemeijer, "Aging and tempering behavior of iron-nickel-carbon and iron-carbon martensite," *Metallurgical and Materials Transactions A*, vol. 28, no. 3, pp. 545–561, 1997.

[120] L. Morsdorf, E. Emelina, B. Gault, M. Herbig, and C. C. Tasan, "Carbon redistribution in quenched and tempered lath martensite," *Acta Materialia*, vol. 205, p. 116521, 2021.

[121] L. Morsdorf, C. C. Tasan, D. Ponge, and D. Raabe, "3D structural and atomic-scale analysis of lath martensite: effect of the transformation sequence," *Acta Materialia*, vol. 95, pp. 366–377, 2015.

[122] M. K. Miller, P. A. Beaven, S. S. Brenner, and G. D. W. Smith, "An atom probe study of the aging of iron- nickel- carbon martensite," *Metallurgical Transactions A*, vol. 14, no. 5, pp. 1021–1024, 1983.

[123] M. Sarikaya, A. K. Jhingan, and G. Thomas, "Retained austenite and tempered martensite embrittlement in medium carbon steels," *Metallurgical Transactions A*, vol. 14, no. 6, pp. 1121–1133, 1983.

[124] J. Akré, F. Danoix, H. Leitner, and P. Auger, "The morphology of secondary-hardening carbides in a martensitic steel at the peak hardness by 3DFIM," *Ultramicroscopy*, vol. 109, no. 5, pp. 518–523, 2009.

[125] G. Badinier, C. W. Sinclair, X. Sauvage, X. Wang, V. Bylik, M. Gouné, and F. Danoix, "Microstructural heterogeneity and its relationship to the strength of martensite," *Materials Science and Engineering: A*, vol. 638, pp. 329–339, 2015.

[126] A. Böttger, P. J. Warren, G. D. Smith, M. Van Genderen, S. Sijbrandij, and E. J. Mittemeijer, "Tempering of iron-carbon-nitrogen martensites:(re) distribution of interstitial atoms," in *Materials science forum*, vol. 318, pp. 103–108, Trans Tech Publ, 1999.

[127] F. Danoix, R. Danoix, J. Akre, A. Grellier, and D. Delagnes, "Atom probe tomography investigation of assisted precipitation of secondary hardening carbides in a medium carbon martensitic steels," *Journal of microscopy*, vol. 244, no. 3, pp. 305–310, 2011.

[128] D. Delagnes, F. Pettinari-Sturmel, M. Mathon, R. Danoix, F. Danoix, C. Bellot, P. Lamesle, and A. Grellier, "Cementite-free martensitic steels: A new route to develop high strength/high toughness grades by modifying the conventional precipitation sequence during tempering," *Acta materialia*, vol. 60, no. 16, pp. 5877–5888, 2012.

[129] D. Pierce, D. Coughlin, D. Williamson, K. Clarke, A. Clarke, J. Speer, and E. De Moor, "Characterization of transition carbides in quench and partitioned steel microstructures by Mössbauer spectroscopy and complementary techniques," *Acta Materialia*, vol. 90, pp. 417–430, 2015.

[130] G. Smith, D. Hudson, P. Styman, and C. Williams, "Studies of dislocations by field ion microscopy and atom probe tomography," *Philosophical Magazine*, vol. 93, no. 28-30, pp. 3726–3740, 2013.

[131] H. P. Van Landeghem, B. Langelier, B. Gault, D. Panahi, A. Korinek, G. R. Purdy, and H. S. Zurob, "Investigation of solute/interphase interaction during ferrite growth," *Acta Materialia*, vol. 124, pp. 536–543, 2017.

[132] C. Zhu, X. Xiong, A. Cerezo, R. Hardwicke, G. Krauss, and G. Smith, "Three-dimensional atom probe characterization of alloy element partitioning in cementite during tempering of alloy steel," *Ultramicroscopy*, vol. 107, no. 9, pp. 808–812, 2007.

[133] B. Sandvik and C. Wayman, "Direct observations of carbon clusters in a high-carbon martensitic steel," *Metallography*, vol. 16, no. 4, pp. 429–447, 1983.

[134] M. Kusunoki and S. Nagakura, "Modulated structure of iron–carbon martensite studied by electron microscopy and diffraction," *Journal of Applied Crystallography*, vol. 14, no. 5, pp. 329–336, 1981.

[135] M. Kusunoki and S. Nagakura, "Modulated structure of iron-carbon martensite studied by electron microscopy and diffraction," *Journal of Applied Crystallography*, vol. 14, no. 5, pp. 329–336, 1981.

[136] S. Babu, K. Hono, and T. Sakurai, "APFIM studies on martensite tempering of Fe-C-Si-Mn low alloy steel," *Applied Surface Science*, vol. 67, no. 1-4, pp. 321–327, 1993.

[137] N. Law, P. Howell, and D. Edmonds, "Structure of lath martensite and occurrence of retained austenite in as-quenched Fe-VC low-alloy steels," *Metal Science*, vol. 13, no. 9, pp. 507–515, 1979.

[138] H. Kwon and C. H. Kim, "Tempered martensite embrittlement in Fe-Mo-C and Fe-WC steel," *Metallurgical Transactions A*, vol. 14, pp. 1389–1394, 1983.

[139] R. Clark and G. Thomas, "Design of strong tough Fe/Mo/C martensitic steels and the effects of cobalt," *Metallurgical Transactions A*, vol. 6, pp. 969–979, 1975.

[140] J. Mola, G. Luan, D. Brochnow, O. Volkova, and J. Wu, "Tempering of martensite and subsequent redistribution of Cr, Mn, Ni, Mo, and Si between cementite and martensite studied by magnetic measurements," *Metallurgical and Materials Transactions A*, vol. 48, no. 12, pp. 5805–5812, 2017.

[141] D. H. Sherman, S. M. Cross, S. Kim, F. Grandjean, G. J. Long, and M. K. Miller, "Characterization of the carbon and retained austenite distributions in martensitic medium carbon, high silicon steel," *Metallurgical and Materials Transactions A*, vol. 38, no. 8, pp. 1698–1711, 2007.

Chapter 5

Influence of Si on the microstructure and C redistribution in martensitic steels

M. Seehaus[1], S. Korte-Kerzel[1], S. Sandlöbes-Haut[1]
[1]Institute of Physical Metallurgy and Materials Physics, RWTH Aachen University, Germany

Materials & Design 229 (2023) 111875
Received: 21 November 2022
Accepted: 24 March 2023

For this publication, the candidate carried out the conceptualisation, experimental work, formal analysis, data curation and drafting of the manuscript. In agreement and collaboration with the co-authors, the published version of the manuscript was finalised.

(Online availability: j.matdes.2023.111875)

Materials & Design 229 (2023) 111875

Contents lists available at ScienceDirect

Materials & Design

journal homepage: www.elsevier.com/locate/matdes

Influence of Si on the microstructure and C redistribution in martensitic steels

Mattis Seehaus *, Sandra Korte-Kerzel, Stefanie Sandlöbes-Haut

Institut für Metallkunde und Materialphysik, RWTH Aachen University, 52074 Aachen, Germany

HIGHLIGHTS

- Silicon addition in Fe-Ni-C alloys leads to smaller initial austenite grains and less retained austenite.
- c/a ratio is not significantly impacted by Silicon addition.
- Identification of the Greninger Troiano orientation relationship for Fe-Ni-C-(Si)
- Si affects the C segregation and partitioning behaviour in the vicinity of the phase interface.
- Combined atom probe tomography and transmission electron microscopy reveal carbon clustering along twins in the martensite.

GRAPHICAL ABSTRACT

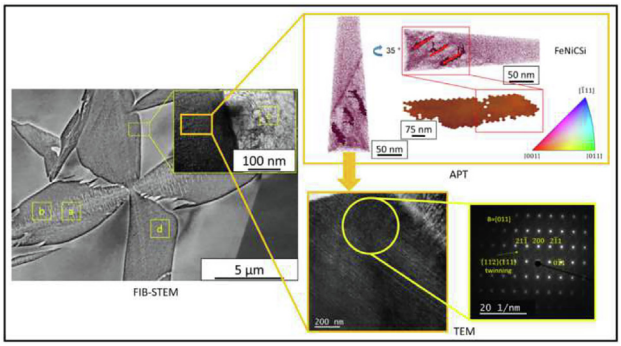

ARTICLE INFO

Article history:
Received 21 November 2022
Revised 10 February 2023
Accepted 24 March 2023
Available online 31 March 2023

Keywords:
Martensitic steel
Carbon segregation
Martensite/austenite interface
Orientation relationship
Atom probe tomography

ABSTRACT

In martensitic steels the distribution of C is fundamental for the technological material properties. However, the effect of Si on C segregation is not known in detail. In this study, the impact of Si on the microstructure of martensitic steels is investigated using scanning electron microscopy and the martensite/austenite orientation relationships are determined using electron backscatter diffraction and transmission Kikuchi diffraction. Transmission electron microscopy and selected area diffraction pattern analysis were used to analyse the intragranular substructure of the martensitic phase. Further, the effect of Si on the redistribution of C is investigated by atom probe tomography in combination with transmission Kikuchi diffraction measurements in order to obtain the local C distribution and correlate it with the crystallography. It was found that the Si addition forms a sigmoidal distribution at the phase boundary and functions as a barrier for C segregation, hence reduces C partitioning into the austenite, while a Si free alloy shows clear C partitioning. Further it was observed that stable C cluster formation occurs along fine twin boundaries in the martensite, inhibiting carbide formation and partitioning of the C into the austenite.

1. Introduction

The microstructure of martensite in steels is of essential interest as many steels obtain their technological properties through martensitic transformation and the resulting hardening. Especially, the distribution of C during this transformation and during natural aging is fundamental for the emerging crystal structure and therefore affecting the material properties significantly.

In a martensitic transformation, the initial phase is subjected to both, a change in crystal structure and a change in shape, which occurs during cooling or deformation through successive

* Corresponding author.
E-mail address: seehaus@imm.rwth-aachen.de (M. Seehaus).

https://doi.org/10.1016/j.matdes.2023.111875
0264-1275/

nucleation by means of autocatalysis [1,2]. In this displacive transformation, the resulting constituents cannot cross high angle grain boundaries and are therefore limited to the grains in which they nucleate [3,4]. Nevertheless, the microstructure of freshly transformed martensite is unstable in the quenched state because the C solid solution in the martensitic phase is supersaturated and there are large internal stresses in the system. After the martensitic transformation, this leads to a larger volume of the crystals that have been transformed as well as a change in the shape [5–7].

In steels, martensite exhibits different morphologies related to the chemical composition of the respective alloy and the cooling rate. The chemical composition also determines the martensite transformation start temperature (M_S), resulting in the formation of lath martensite at high M_S temperatures, whereas at low M_S temperatures plate martensite is formed, that can be lenticular [8,9]. The specific substructure and crystallography are consequently directly dependent on the chemical composition and temperature treatment.

The mechanisms determining the structural changes at low temperatures were found for steels by investigations using X-ray diffraction (XRD), Mössbauer techniques and neutron diffraction [10–16]. XRD investigations revealed that the c/a ratio of the martensite (bct) lattice parameters is abnormally small in some alloyed steels with an austenitic microstructure at room temperature (RT) that were quenched below 0 °C in liquid nitrogen, whereas ambient temperature leads to an increase in the c/a ratio, which is consistent with its C concentration [6,17]. This change could be attributed to a redistribution of C atoms to octahedral interstitial sites along the c-axis from equivalent interstitial sites on the other lattice axes, consistent with Zenefs theory that the ordered distribution of C is more stable inside a unique sublattice of octahedral interstitial sites [6,17]. Accordingly, the redistribution of C is of fundamental interest for the crystal structure formed during martensitic transformation.

C redistribution has been studied for several decades [18–30]. A redistribution of C atoms can occur either inside the crystalline lattice or outside by a diffusion process, which was reported experimentally for the first time within the interstices of the martensite lattice in manganese steels [10–16]. The C distribution and segregation at the interface between tempered martensite and austenite was reported to increase significantly in a 2 wt-% Mn steel after annealing at 200 °C for 1 h [31]. One of the first studies related to C redistribution in steels on the example of plate martensite observed C segregation at the coherent twin interfaces [32]. In Fe-C alloys, quenching down to RT continues to promote auto-tempering after the martensitic transformation, which results in the precipitation of carbides, C clustering, segregation to microstructural features like voids, dislocations or phase boundaries, spinodal decomposition and eventually depletion of C in the matrix [9,21,22,24,26,27,31,33–48].

Therefore, in the current study the redistribution of C is investigated by the addition of Ni, allowing a martensite starting temperature below RT and stabilising the austenite. Ni also decreases the lattice parameters and, with increasing content, leads to a lower solubility of C in α iron in metastable equilibrium with γ iron [49–51]. In Fe-Ni-C steels the C has a high solubility in austenite and a low solubility in ferrite [52]. In Fe-Ni-C steels, the Ni content has a significantly stronger impact on the M_S temperature than the C content. If the Ni content is above 25 wt-%, the M_S temperature is below 0° [53,54]. The martensite, which is supersaturated in C, is then formed by quenching in liquid nitrogen. Until subsequently isothermal conditions are set at ambient temperature, C diffusion is kinetically inhibited [9]. The addition of Si increases the residual austenite content and elevates the upper temperature barrier for stable C clusters, thus retarding in particular cementite precipitation during tempering. However, the effects of Si on C segregation are not known in detail yet [55,56].

The present study aims at gaining a deeper understanding of the redistribution of C subsequent to the martensitic transformation. Therefore, the influence of Si on the C redistribution in the vicinity of the austenite/martensite interface and twin boundaries in Fe-Ni-C-(Si) alloys after 2 years of aging at RT is investigated using transmission electron microscopy (TEM) and atom probe tomography (APT) revealing significant effects of Si on the C partitioning.

2. Experimental procedure

The alloys investigated in this work were synthesised by casting and rolling and have a completely austenitic microstructure at RT. This provides the advantage that it is possible to characterise the initial austenite microstructure prior to the formation of martensite which is not possible for steels with a M_S temperature significantly above RT. The chemical composition of the two alloys investigated was Fe-24 wt%Ni-0.4 wt%C (called FeNiC in this study) and Fe-24 wt%Ni-0.4 wt%C-2 wt%Si (called FeNiCSi in this study). The samples were not completely placed into liquid nitrogen, but only half of them and the other half stayed at RT, which preserved some retained austenite together with the transformed martensite. This allows the determination of the orientation relationship between the two phases α' and γ. In addition, the two samples were aged for two years at RT in order to obtain and analyse the C redistribution.

For the microstructure investigations, the samples were cut from the rolled sheets by electrical discharge machining and subjected to metallographic preparation. The samples were first mechanically ground and then polished down to 0.25 μm using a diamond suspension. Finally, the specimens were electropolished at 30 V and 30 s using an A2 (Struers) electrolyte.

The chemical composition of the bulk samples was measured using energy-dispersive x-ray spectroscopy (EDS) in a Dual-Beam-FIB (Helios Nanolab 600i, FEI), and is shown with the estimated c/a ratios in Table 1. Scanning electron microscopy (SEM), electron backscatter diffraction (EBSD), backscattered electron (BSE) imaging, scanning transmission electron microscopy (STEM), transmission Kikuchi diffraction (TKD) and site-specific preparation of APT and TEM samples was conducted in the same Dual-Beam-FIB Helios Nanolab 600i (FEI).

The microstructure analysis by means of EBSD measurements was performed at 15 kV and 1.4 nA using a Hikari detector (EDAX Inc.). The EBSD maps have an area of 180 · 140 μm, were recorded with a step size of 250 nm and analysed by means of the free MTEX 5.7.0 toolbox based on Matlab® [57].

Macrotexture measurements were conducted by XRD using a Bruker D8 Advance diffractometer and a HI-STAR multi-wire X-ray detector. TEM analysis was performed in a JEM-F200 (JEOL) transmission electron microscope operated at 200 kV.

Both alloys were investigated using APT in a local electrode atom probe (CAMECA LEAP 4000X HR) to study local differences in C concentration and also the distribution of the other alloying elements Ni and Si. For this purpose, EBSD measurements were performed to determine areas of interest, i.e. austenite–martensite interfaces, and the APT tips were site-specifically prepared from the interfaces. The measured APT tips were obtained from the same two samples, four each from FeNiC and FeNiCSi. The APT analyses were conducted using the laser pulse mode, with 30 pJ laser energy, 125 kHz pulse rate and a temperature of 50 K. As soon as a sample had been lifted out and thinned to a proper APT tip shape, TKD was conducted on the APT tip to characterise the

Table 1
Chemical composition of FeNiC and FeNiCSi from EDS, respectively, and calculated c/a ratios based on the C contents determined by APT.

	Fe [wt.-%]	Ni [wt.-%]	Si [wt.-%]	c/a
FeNiC	76.33	22.74	–	1.0016
FeNiCSi	75.37	21.10	0.93	1.0028

crystallography of the APT tip [58,59]. The benefits of utilising TKD in an FIB to simultaneously analyse and mill a site specific APT tip have been shown recently [60,61]. However, the electron beam scanning of the APT tip during the TKD measurement has the major disadvantage that the tip might be contaminated by hydrocarbons that can affect the detection during the atom probe measurement. This can be minimised by plasma cleaning. Reconstructions were performed using the AP Suite 6.1.0.35 software. The peak decomposition and subsequent analysis was conducted using the IVAS software. In Fig. 1, the process of preparing an APT tip with an austenite–martensite phase boundary is shown.

The expected c/a ratios were calculated based on the C content ([C] in wt.-%) measured by APT using Eq. (1) [62–68], see Table 1.

$$\frac{c}{a} = 1 + 0.045[C] \quad (1)$$

3. Results

The midrib of the lenticular martensite is composed of a substructure of aligned transformation twins that initiate growth to the lenticular shape as shown in Fig. 2 [69]. To reveal the basic microstructural differences between the two alloys, SEM and BSE images were acquired first, highlighting the various substructures of the lenticular martensite and at the same time showing the differences due to the presence of Si in Fig. 3c) and d), respectively.

It is evident from the BSE and EBSD measurements presented in Fig. 3c)-h) that the addition of Si leads to a finer structure of the martensite, but also a higher variation in the size of the lenticular martensite plates. Other major differences between FeNiC and FeNiCSi are the different lenticular plate sizes as well as the fractions of transformed martensite, which amount to approximately 20 % and 56 %, respectively, when considering the EBSD maps shown in Fig. 3e)-f).

The grain size distributions determined from the EBSD measurements, Fig. 4, are consistent with the visual observation that the addition of Si leads to the formation of finer martensite lenticular plates in FeNiCSi, although some martensite lenticular plates are quite large compared to the majority of the lenticular plates. The grain sizes of the austenite range between 40 and 1650 μm^2 in FeNiC and 44–830 μm^2 in FeNiCSi. The same tendency is

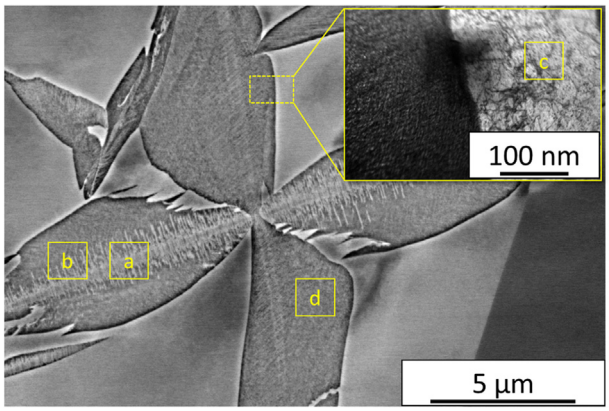

Fig. 2. Substructure of lenticular martensite in FeNiC observed using BSE. a) Midrib (fine transformation twins); b) Twins originating from the midrib; c) Austenitic matrix exhibiting a high density of curved and tangled dislocations observed by means of bright field scanning transmission electron microscopy (FIB, 30 kV); d) High density of dislocations in the martensite.

revealed by the martensite grain size ranges of 5–235 μm^2 in FeNiC and 5–30 μm^2 in FeNiCSi. It should be noted that the initial austenitic structure of FeNiCSi exhibits smaller austenite grains than that of FeNiC, which constrains the lenticular martensite size during transformation.

In order to analyse the local microstructure of both alloys in more detail, TKD and correlative FIB-STEM was performed, Fig. 5. When comparing Fig. 5a) and b), the higher number of martensite grains and, consequently, growth directions for martensite in FeNiCSi is evident, causing a high amount of impingement events as visible in 5b). In contrast to the STEM image of Fig. 5d), larger martensite plates are observed for FeNiC, see Fig. 5c). Additionally, the phase maps of FeNiC and FeNiCSi are also presented as Fig. 5e) and f), respectively.

The phase fractions and lattice parameters at RT were measured by means of XRD. These measurements also show that FeNiCSi has a much lower residual austenite content than FeNiC, and consequently contains a larger amount of transformed martensite (Table 2) as was already visible from the EBSD maps presented in Fig. 3e)-f).

Determination of the OR between martensite and austenite was performed using a Matlab® code developed for this purpose, the detailed procedure and the code are available in [70]. In order to analyse whether the samples FeNiC and FeNiCSi belong to one known OR and to which one, pole figures were generated from the corresponding EBSD data sets and compared in terms of rotation angle deviation with calculated theoretical ORs, Table 3.

The comparison in Fig. 6 clearly suggests that the GT OR fits best to FeNiC and FeNiCSi, respectively.

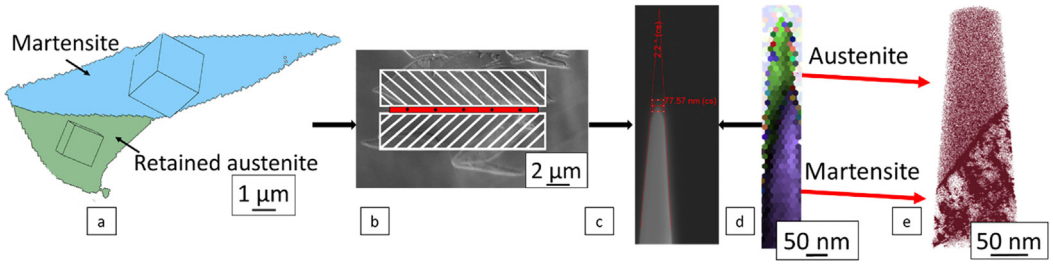

Fig. 1. Conceptual sketch of TKD correlative APT sample preparation: a) EBSD measurement to find a region of interest (interface); b) Lift-out (white regions are bulk material and the red region shows the lamellar structure for 4–5 APT tips); c) Placing of samples on Si wafers; d) Final thinning step with correlated TKD measurements to ensure tracing the interface during milling; e) Reconstruction of readily thinned tip after the APT measurement showing the C concentration with an isoconcentration surface of 5 %. (For interpretation of the references to color in this figure legend, the reader is referred to the web version of this article.)

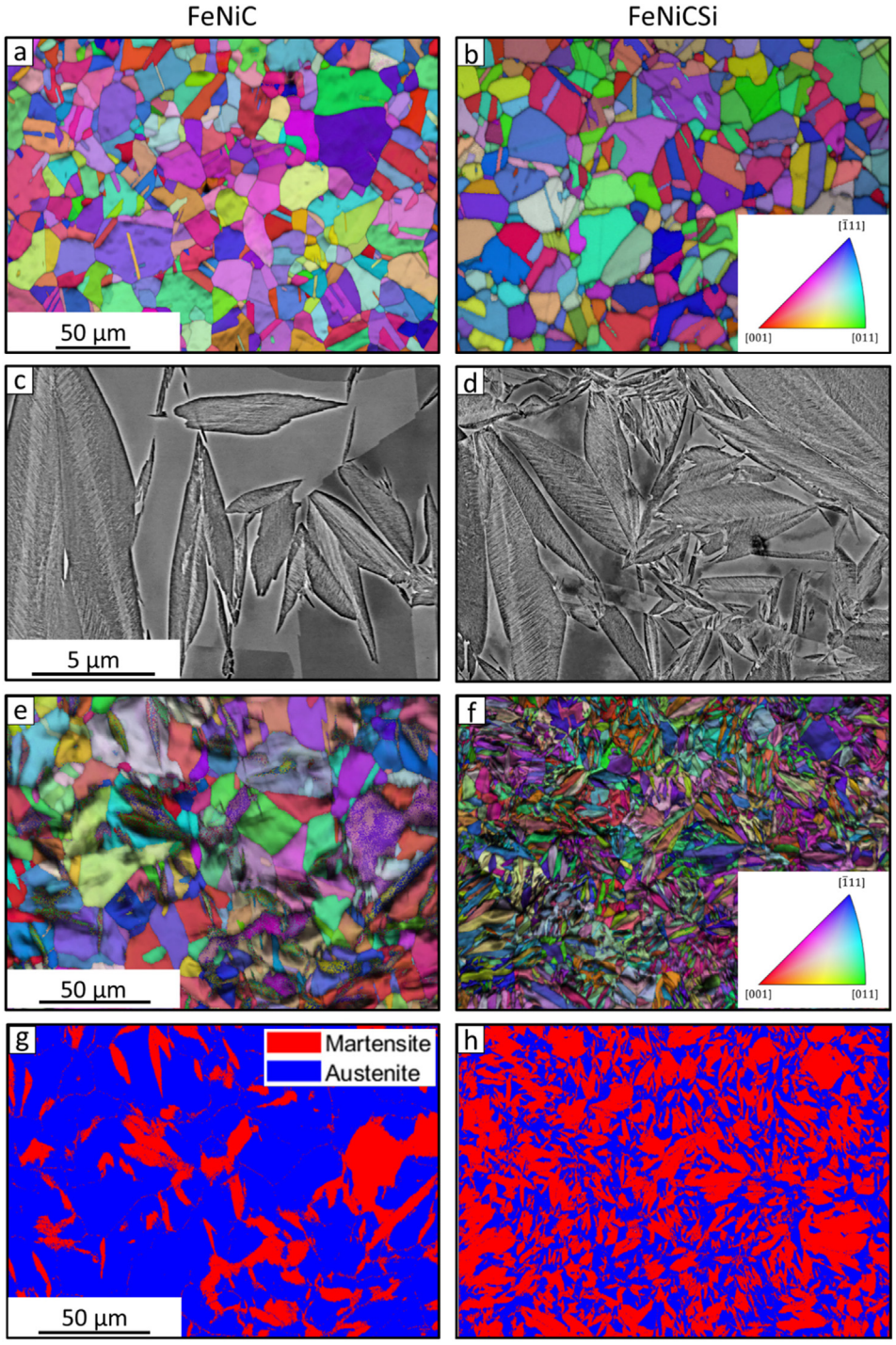

Fig. 3. a), b) Initial EBSD and associated inverse pole figure (IPF) of the fully austenitic microstructure before quenching; c), d) BSE micrographs; e), f) EBSD after martensite formation g), h) phase maps revealing the microstructural differences of the martensite.

The misorientation angle distributions of α'/γ phase boundaries within a range of ± 5° deviation are shown in Fig. 7 for FeNiC and FeNiCSi, respectively. The martensite-austenite misorientation profiles show peaks at an average misorientation angle of about 44.5°, which lies between the misorientations predicted by KS and NW, respectively, and therefore particularly close to 44.23° of the Greninger-Troiano OR [75].

In addition to the visual comparison, a quantitative analysis of the pole figures using correlation coefficient analysis and orientation angle deviations further confirmed the existence of the GT orientation relationship between austenite–martensite interfaces and is described in [70] in detail. Fig. 8 shows typical APT measurements of the two alloys, where the purple spots represent C atoms. The tips were analysed by defining a cylindrical volume of 20 nm diameter and a length of 20 nm, from which a perpendicular 1D-concentration profile of the alloying elements Fe, C, Ni and Si was obtained.

It is observed that the austenite in FeNiC is enriched with C atoms, while in FeNiCSi the C distribution is more homogeneous. This indicates that the presence of Si reduces C partitioning into

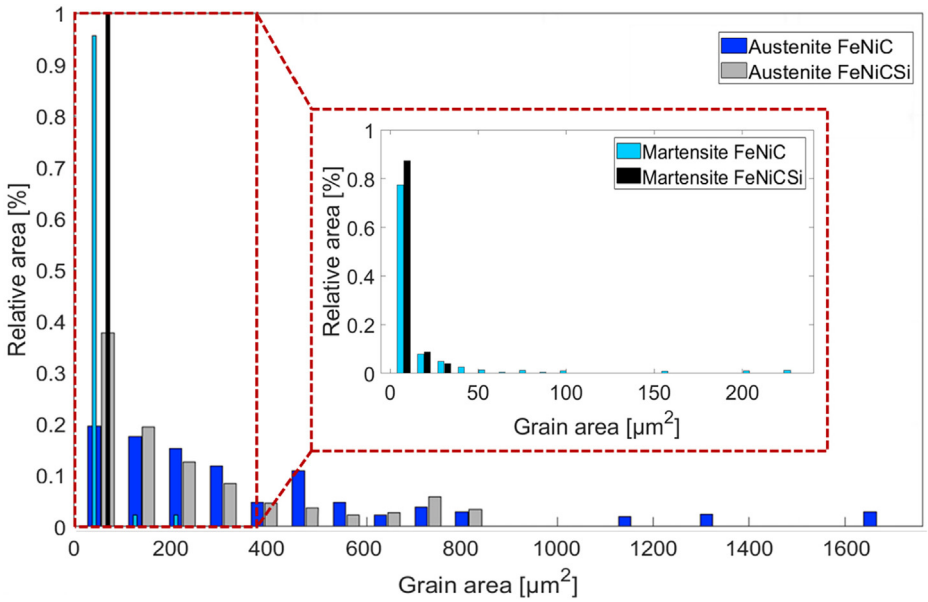

Fig. 4. Grain size distribution for austenite and martensite with and without Si.

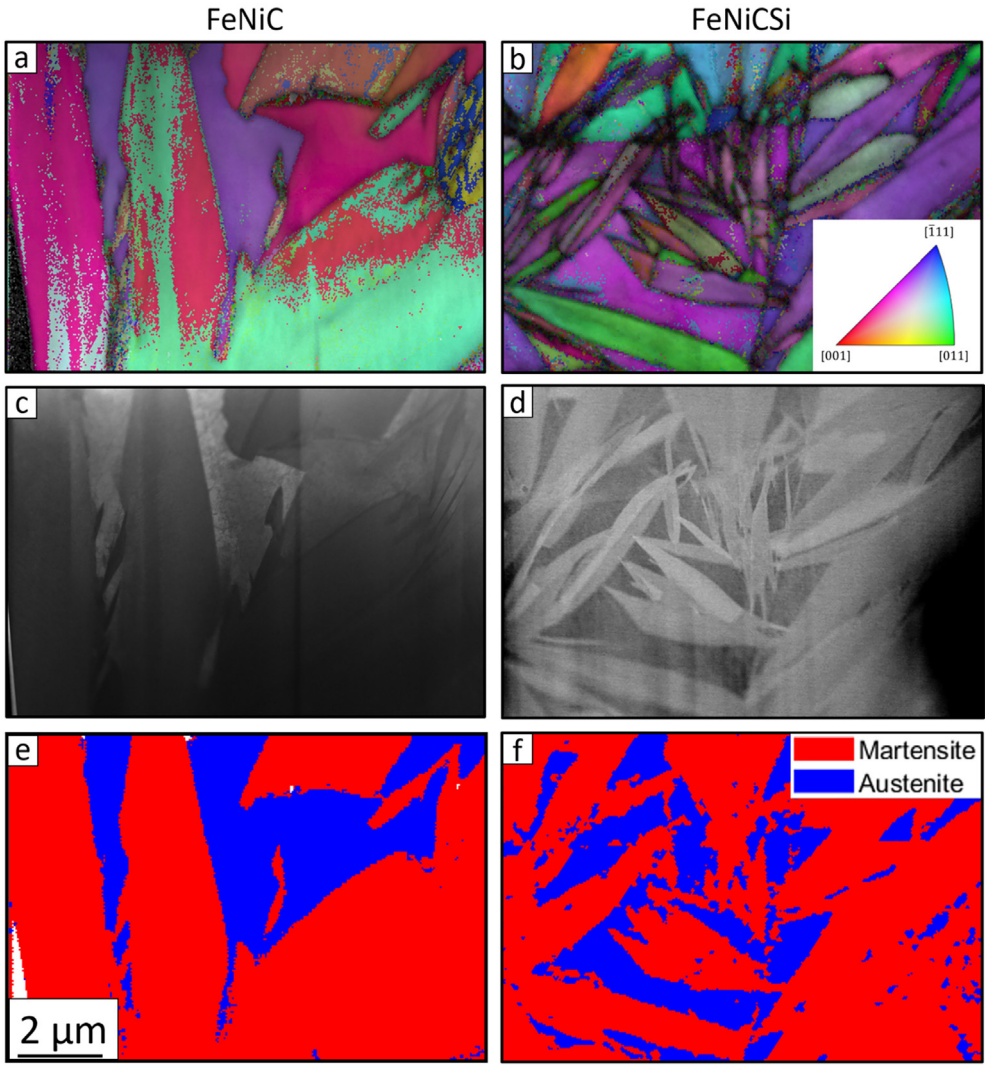

Fig. 5. TKD, FIB-STEM and corresponding phase maps for FeNiC (left) and FeNiCSi (right), respectively.

Table 2
Area fraction, lattice parameters, and measured c/a ratio of austenite and martensite for FeNiC and FeNiCSi, respectively, by means of XRD.

Alloy	Austenite [%]	Lattice parameter a_γ [Å]	Martensite [%]	Lattice parameter $a_{\alpha'}$ [Å]	c/a
FeNiC	79.79	3.599 ± 0.001	20.21	2.864 ± 0.001	1.012
FeNiCSi	25.87	3.586 ± 0.001	74.13	2.860 ± 0.001	1.011

Table 3
Most common ORs between martensite and austenite crystals in steels [71].

Name	OR	(uvw) ω_{min}
Bain [72]	$\{100\}_\gamma//\{100\}_\alpha$ $\langle 100\rangle_\gamma //\langle 110\rangle_\alpha$	⟨100⟩ 45°
Nishiyama-Wasserman (NW) [73]	$\{111\}_\gamma//\{110\}_\alpha$ $\langle 112\rangle_\gamma//\langle 110\rangle_\alpha$	<0.98 0.08 0.20> 45.98°
Kurdjumov-Sachs (KS) [74]	$\{111\}_\gamma//\{110\}_\alpha$ $\langle 110\rangle_\gamma//\langle 111\rangle_\alpha$	<0.97 0.18 0.18> 42.85°
Greninger-Troiano (GT) [75]	$\{111\}_\gamma//\{110\}_\alpha$ $\langle 123\rangle_\gamma//\langle 133\rangle_\alpha$	<0.97 0.19 0.13> 44.23°
Pitsch [76]	$\{100\}_\gamma//\{110\}_\alpha$ $\langle 110\rangle_\gamma//\langle 111\rangle_\alpha$	<0.08 0.20 0.98> 45.98°

the austenite. In the interfacial region, a significant change in the concentration gradient is observed, evidenced by a decrease of C and Ni across the austenite–martensite interface in FeNiC. In FeNiCSi a significant increase of C and Ni at the interface is observed, whereas a C-depleted region can be found on both sides of the C enriched area. It is also worth noting that the Si concentration in FeNiCSi shows a sigmoidal tendency within the interfacial region.

4. Discussion

The influence of Si on the microstructure formation and the C distribution in martensitic steel has been investigated. Here, it was observed that the addition of 2 wt-% Si to FeNiCSi leads to smaller austenite grains and also to smaller lenticular martensite plates. This is most probably caused by the increase of the Ac3 temperature due to the Si addition, which results in smaller austenite grains at a given temperature in the higher Si alloy when comparing two alloys with different Si contents. Smaller austenite grains saturate their nucleation sites faster than larger ones, which limits their ability to grow before impingement occurs and the transformation can only be suppressed by hindering plastic absorption, such as the absence of dislocations or grain refinement by Si addition [77,78]. It was also observed that both alloys, FeNiC and FeNiCSi, exhibit the GT OR between martensite and austenite. Similarly, in an Fe-33Ni steel it was revealed that the OR between α'/γ in the mid-rib region of lenticular martensite is close to GT, while at the interface between the cohesive martensite and the austenite it was closer to KS OR [79,80]. In investigations on a 14 Ni steel, the NW-OR was predominantly observed and the differences in the martensitic structure as well as interfacial orientation were investigated for interfacial mobility, showing that the NW-OR exhibited a stationary rather than a mobile interface compared to the KS-OR [81]. However, in the present study, the intragranular misorientations were less than 1°, indicating that the GT OR was observed not only near the midrib but also close to the boundary with the austenite. In a study with a similar alloy (Fe-31%Ni-0.01C) and partially transformed lenticular martensite in combination with retained austenite, it was reported that despite a scatter of orientations was observed near both, the interface and the midrib, the misorientations were closer to the GT orientation and accordingly the OR was the same between the midrib and the interface [82]. The results further indicate that Si does indeed influence the C redistribution, but in the present study no influence of the martensite size and volume fraction on the C redistribution was observed, probably due to the fact, that the C atoms mainly segregate to the twin boundaries and do not partition into the austenite.

A main aspect of this study is how Si affects the C redistribution. The local elemental C distributions for both alloys were investigated using APT. In FeNiCSi, a local enrichment of C at the phase boundaries between austenite and martensite and a low partitioning of C into the austenite is observed. This behaviour was also found in an Fe-1C-1Mn-2Si alloy where the addition of silicon stabilised the austenite phase during the partitioning stage, promoting the distribution of C from martensite into austenite and resulting in a build-up of C at the edge of the austenite grain [83]. C segregation into the austenite is generally favoured by the smaller size of octahedral sites in martensite compared to austenite. Further, it is probable that interstitial C diffusion into the austenite occurs even at RT, leading to the C partitioning from martensite to austenite observed in FeNiC (see Fig. 8a) [84]. This C distribution is facilitated by larger diffusion distances of C in the austenite compared to the thicknesses of the martensite laths [85]. Furthermore, Si tends to segregate into the austenite due to the lower volume of martensite compared to austenite [86–89]. However, the low temperature (RT) may limit substitutional vacancy-assisted diffusion into the austenite matrix, leading to small diffusion paths, whereas the high defect rate at the phase boundary enables local diffusion from the martensite to the austenite in the vicinity of the interface. This is in accordance with the observed sigmoidal Si distribution, as indicated by the local Si depletion on the martensite side and the corresponding Si increase on the austenite side of the interface (see Fig. 8b). Based on thermo-kinetic simulations and also experimental investigations, similar sigmoidal tendencies for Si segregation and a similar carbon redistribution behaviour was found, although at higher temperatures [90,91]. The increased presence of Si in the austenite adjacent to the phase boundary might function as a barrier to carbon segregation from martensite to austenite. The presence of Si was suspected to reduce the diffusion speed of C at RT by decreasing diffusion paths due to repulsion and thereby blocking C at sites near Si atoms, which was found in DFT studies at higher temperatures [92]. Carbon diffusion far into the austenite matrix was observed in the Si free alloy, while in FeNiCSi the addition of Si led to a threefold increase in the C content within the interfacial

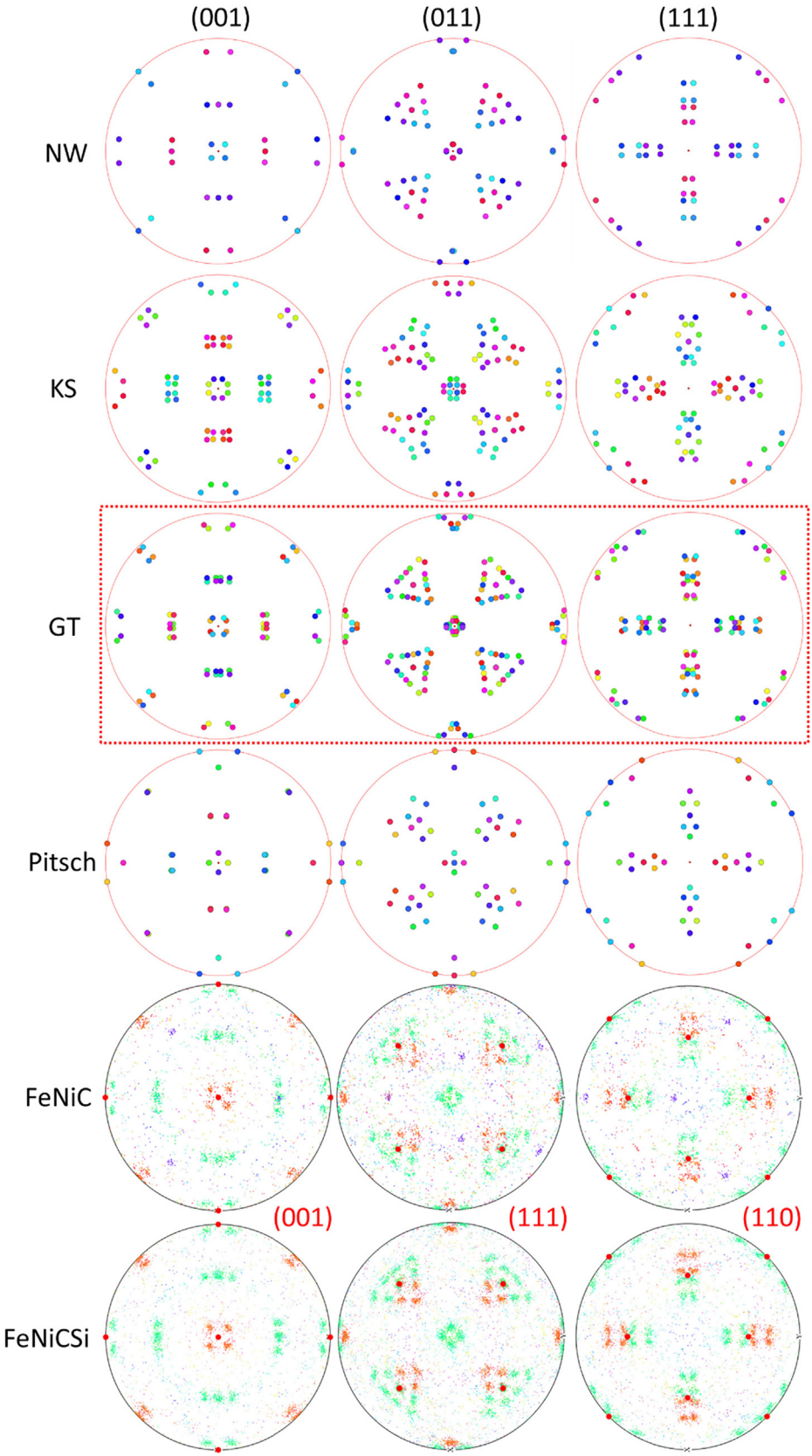

Fig. 6. Pole figures calculated for various theoretical ORs, namely Kurdjumov-Sachs (KS), Nishiyama-Wasserman (NW), Greninger-Troiano (GT), Pitsch (identical colours relate to the same variant) and experimentally obtained data for FeNiC and FeNiCSi, respectively, colourised according to an inverse pole figure color key (see e.g. Fig. 5). The large red poles of the experimental pole figures represent the reference austenite orientation, whereas the red dashed line indicates the visually closest OR correspondence with the experimental data. (For interpretation of the references to color in this figure legend, the reader is referred to the web version of this article.)

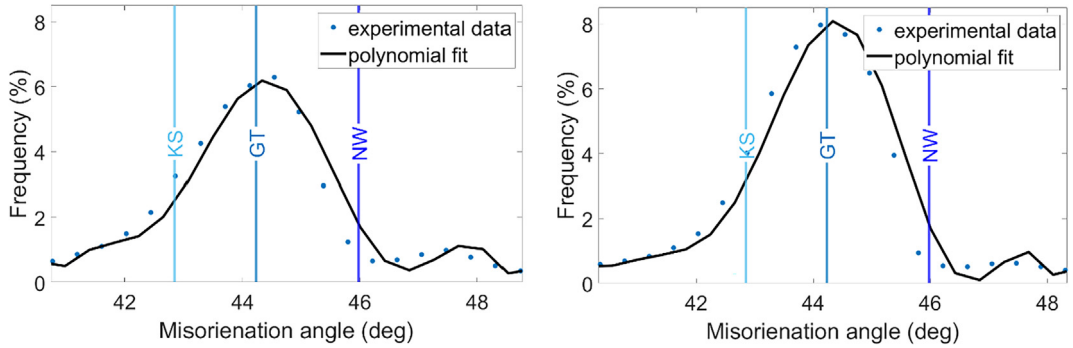

Fig. 7. Fitted misorientation distributions of α'/γ phase boundaries for FeNiC (left) and FeNiCSi (right) with respect to different ORs.

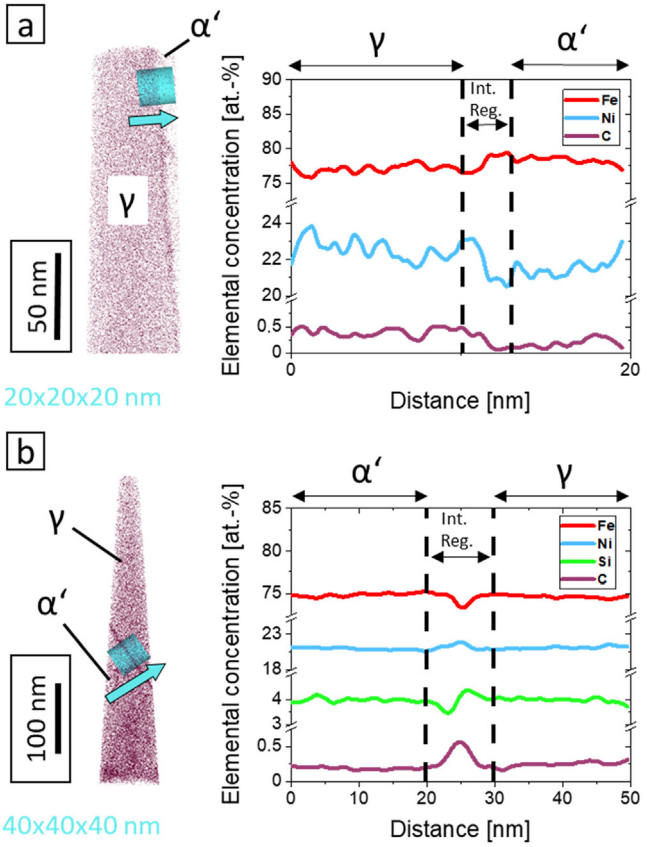

Fig. 8. 3D Reconstructions of representative APT tips from alloys a) FeNiC and b) FeNiCSi (purple dots represent C atoms). The concentration line profiles are stemming from the cylinders drawn in the reconstructions and show the local chemistry at austenite–martensite phase boundaries along the arrows, respectively. (For interpretation of the references to color in this figure legend, the reader is referred to the web version of this article.)

region between the martensite and austenite, as it was observed also in other alloy systems, e.g. in a Mn steel [31].

In addition to the enrichment of C at the phase boundaries between austenite and martensite, segregation occurred in the form of C-enriched clusters in the martensite during natural aging for 2 years. For steels with a carbon content of 0.3–1.5% C, the carbon atoms can diffuse interstitially into the tetragonal martensite lattice at RT tending to segregate into defects and form small clusters after natural aging [21,56,93,94]. To analyse these C clusters in more detail, crystallographic analysis of the APT tips and TEM was performed. From the 3D APT reconstructions, it is visible, that the C-enriched clusters form as parallelly aligned platelets most probably along specific planes, such as twin or habit planes, Fig. 9. In another study on Fe-15Ni-1C (wt.-%) steel after natural aging of up to three years, the interface between η-carbides and the martensitic matrix indicated a {5 2 1} habit plane, which was selected due to the internal distortion of the martensite and the high strain energy [80,95,96]. To find out whether the C clusters observed in the present study also formed along {5 2 1} habit planes, the TKD data of the APT tips were used to determine the crystallographic nature of the C clusters. The correlation of the TKD and APT data could be determined from the martensite-austenite interface shown in Fig. 9a) and Fig. 9f). As the C-rich clusters are not orientated edge-on, rotating the 3D-reconstructions by 98° and 35°, respectively, about their length axis brings the C clusters into an edge-on orientation. The so determined planes of the C-enriched clusters are highlighted by continuous red lines in Fig. 9d), e), i) and k). The light blue regions show an estimated tolerance range of 5° since the APT reconstruction correlated with the TKD required a visual approximation. Fig. 9d) and i) show the standard projections of the martensite orientations as well as the suggested [80,95,96] {5 2 1} poles of the martensite phase oriented in the same way as the martensite plate shown in Fig. 9c) and h). Thus, at the intersections between the outer circle of the stereographic projection and the dashed lines, the habit planes are located, revealing for FeNiCSi a pole of the {5 2 1} family is close, however not for FeNiC. Therefore, the standard projection of the {1 1 2} ⟨1 1 1⟩ twinning system in Fig. 9e) and 9 k) for FeNiC and FeNiCSi, respectively, were further analysed revealing that the C clusters are aligned along the twinning planes after aging at RT for 2 years.

In order to determine if twins are present in the FeNiC and FeNiCSi and how the distance between the possible twin boundaries correlates with the density of C clusters, further TEM was performed on samples that were lifted out close to the regions investigated by APT, Fig. 10.

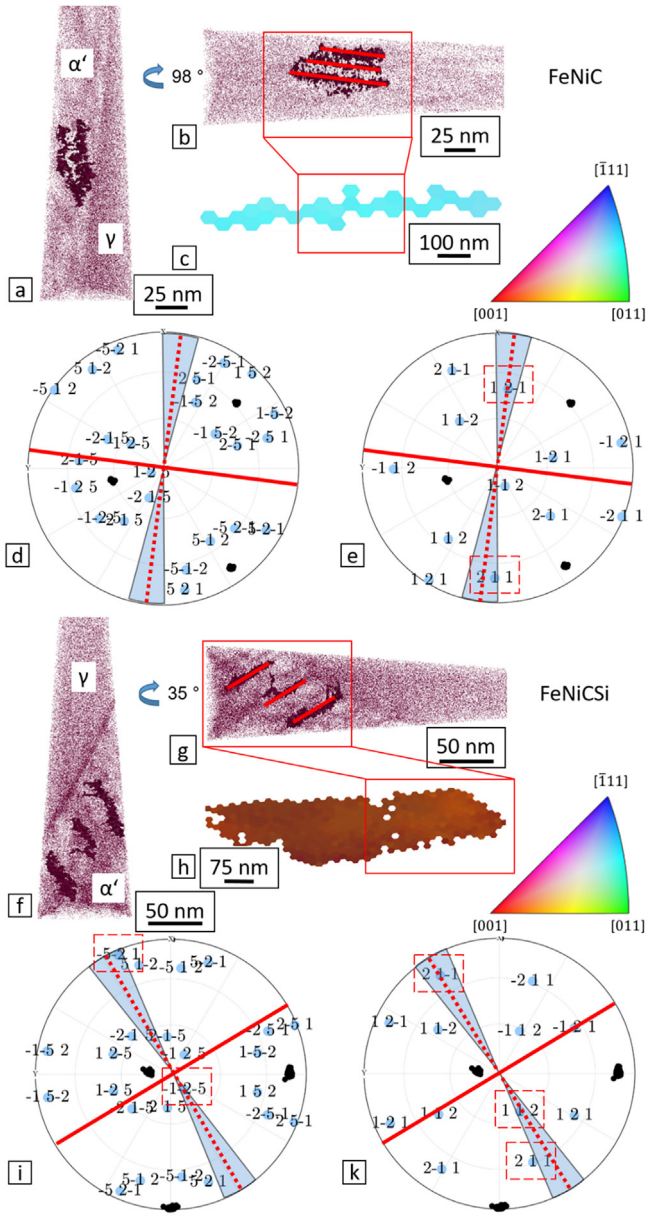

Fig. 9. APT analysis of the habit planes of the C-enriched clusters. C atoms are displayed as purple points. a), f) 3D reconstructions of APT tips for FeNiC and FeNiCSi, respectively, showing exemplary elongated C *iso*-concentration surfaces enveloping C-enriched clusters with 0.7 % C and in total 50 % of the detected C atoms. b), g) Rotation of the tip in a way that the C-enriched clusters are edge-on aligned with the TKD maps. c), h) EBSD orientations of the martensite; d), i) Stereographic projections showing the orientation of the martensite and the poles of the {5 2 1} habit planes. e), k) Stereographic projections showing the orientation of the martensite and the habit planes of the C-enriched clusters revealing that the clusters are aligned parallel to the {1 1 2} twinning plane. (For interpretation of the references to color in this figure legend, the reader is referred to the web version of this article.)

Indeed, it was observed that the martensitic plates of FeNiC and FeNiCSi contain a high density of planar defects, which, when tilted edge-on, were identified as {1 1 2} ⟨1 1 1⟩ twins using SAD, Fig. 10d) and h). In Fig. 10c) and g) the intermediate distances between the nano-twins along the exemplary red dashed lines perpendicular to the twins in Fig. 10b) and f) using the GMS3 software were determined by filtering and calculating the differences between the local maxima. The average distance between the twins amounts to 9.87 ± 0.55 nm and 9.83 ± 0.59 nm for FeNiC and FeNiCSi, respectively. These twins are not detected using TKD as the twins are smaller than the interaction volume (~3.2 μm for Fe at 30 keV) of the electron beam with the sample [97,98].

The observed segregation of C to the twin boundaries can cause a relaxation of the martensite as fewer C atoms are interstitially present, but on the other hand, it might either strengthen or embrittle the twin boundaries. This combination might result in an overall weakened martensite, but in highly decorated twin boundaries that might act as strengthener of the martensite. It is generally assumed that the segregation of C to the twin boundaries in the martensite is preferential when compared to partitioning into the austenite as this would lower the strength of the martensite and therefore also the strength of the material. Since the C redistribution occurs even at room temperature during service, the partitioning of C into the austenite should be avoided as the macroscopic properties, specifically the strength, are consequently degraded during operation, which, after several years, might result in the requirements for the part or component no longer being met.

From Fig. 10 it is also evident that the austenite contains a high density of geometrically necessary dislocations presumably due to high stresses occurring during the martensite formation. Dislocations are also known to attract C-segregation in martensite. However, no C clustering was observed in the austenite, but it should be noted that a clear distinction of dislocations by APT is limited. Furthermore, in lenticular martensite, the dislocation density is reportedly inhomogeneous, resulting in high densities at the martensite/austenite interfaces and low densities in the mid-rib region [32,69,99–102], as was also observed in the present study.

Finally, to analyse if the C clusters observed using APT have formed at the twins observed using TEM, the width and distances of the C-enriched clusters were determined from the APT data, as illustrated in Fig. 11d) and h) and compared to the mean twin distances observed using TEM. The average C cluster distances determined from the distances between the peak concentrations of parallelly aligned C-enriched clusters amount to 10.2 ± 0.6 nm for FeNiC and 9.9 ± 0.4 nm for FeNiCSi, respectively. These results correspond to the mean distances of the twins found by TEM and indicate that the C-enriched clusters indeed form along the fine twin boundaries, thereby inhibiting the precipitation of carbides and also reducing the driving force for C partitioning into the austenite. In particular Si addition (3.2 at. pct) in Fe-Ni-C steels was reported to increase the temperatures for the onset of carbide precipitation [56]. In the present study no carbides were observed for both alloys, FeNiC and FeNiCSi.

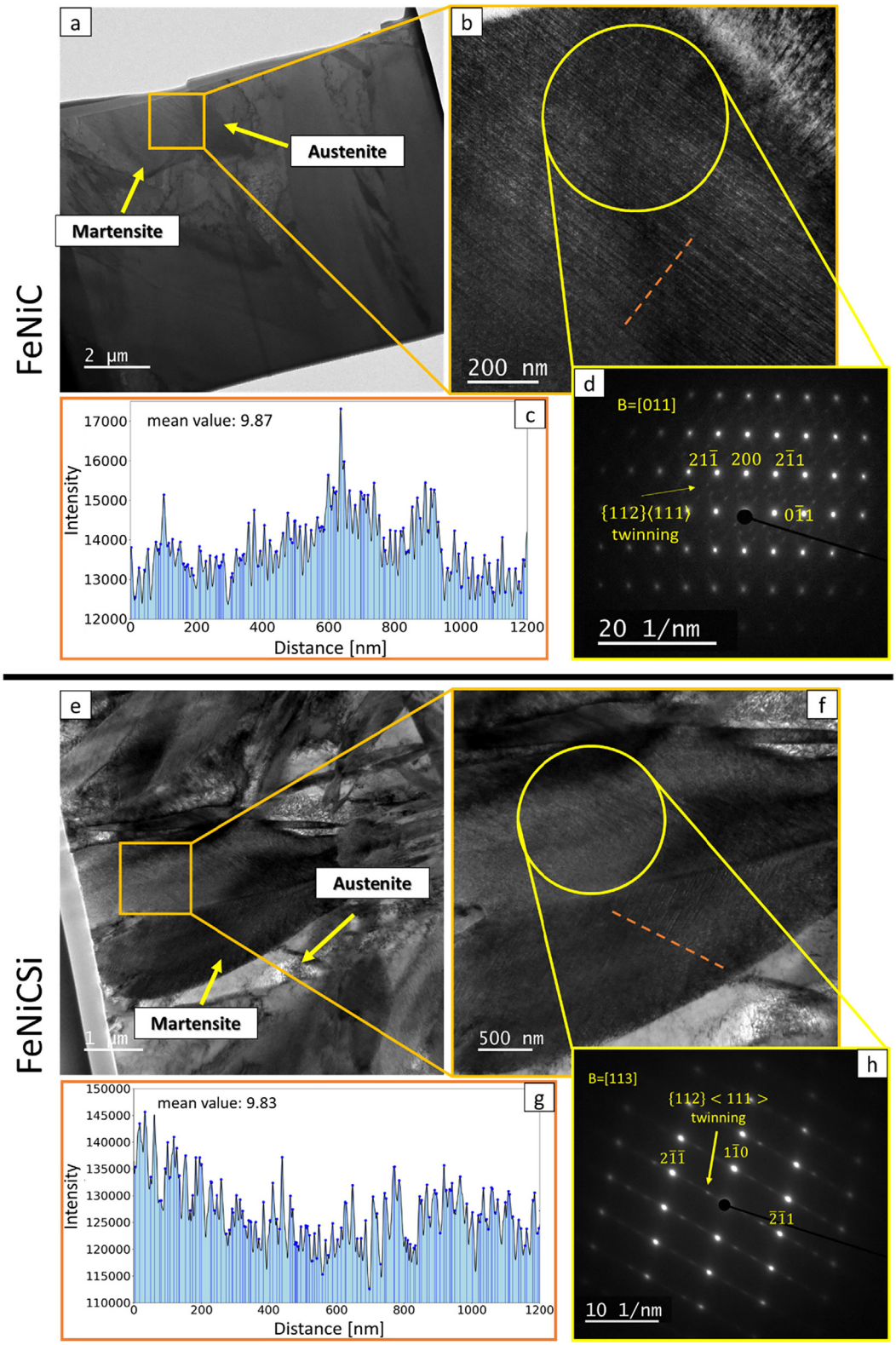

Fig. 10. TEM analyses of FeNiC and FeNiCSi lamellae, respectively. a), e) Lamellae with a thickness of ~ 100 nm revealing the microstructural austenite and martensite phases highlighting the regions for the SADP in d) and h); b), f) High density of a nano-twin substructure of the martensite phase; c), e) Intensity along the red dashed lines in c) and f) in a distance of 1200 nm highlighting the mean distances between the peaks, respectively; d), h) SADPs of the regions of interest depicted in a) and e) revealing the twinning system. (For interpretation of the references to color in this figure legend, the reader is referred to the web version of this article.)

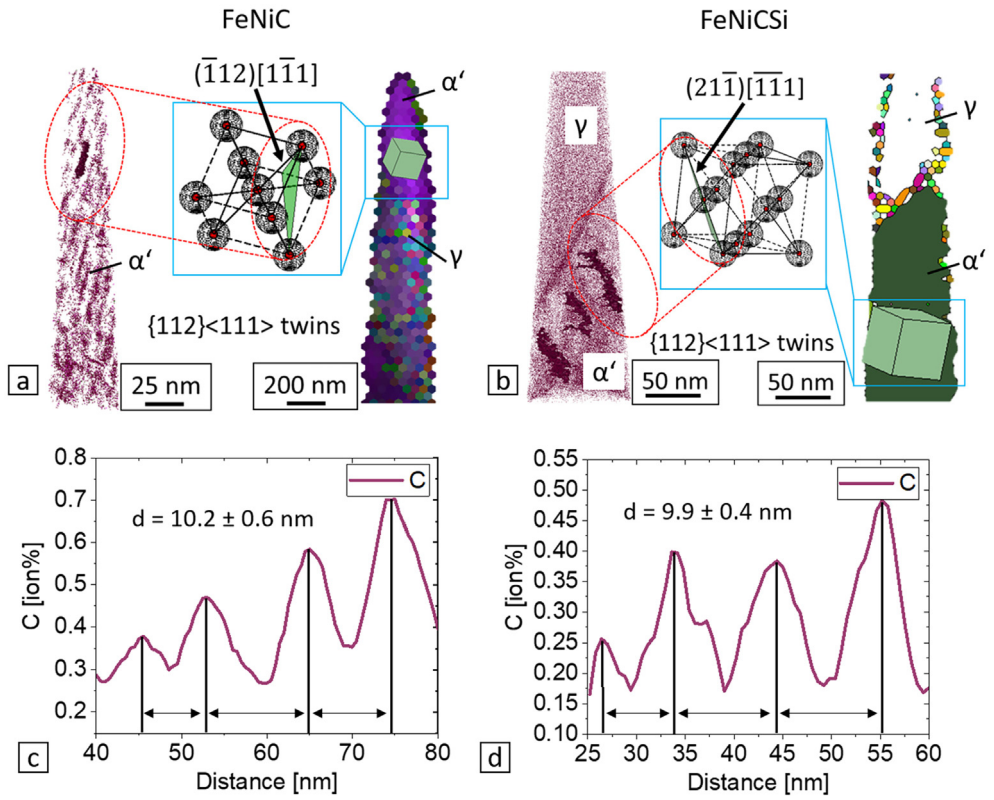

Fig. 11. Correlated analysis of the C-enriched clusters using APT and correlative TKD. 3D-reconstructions of the martensite phase of FeNiC (a)) and FeNiCSi (b)) highlighting exemplary C isosurfaces (0.6 % C) are represented. TKD analyses of the APT tips highlighting the martensite orientations in the APT tips and bcc unit cells show the twinning plane with the crystallographic alignment of the C-enriched clusters. c), d) C distributions along cylindrical regions of interest perpendicular to the parallel C-enriched clusters shown in a) and b).

5. Conclusions

The influence of Si on the microstructure formation and C redistribution in two Fe-Ni-C(-Si) steels aged at RT for two years was studied. From the present study the following conclusions are derived:

- The addition of 2 wt-% Si to a Fe-24 wt-%Ni-0.4 wt-%C alloy leads to a lower volume fraction of retained austenite, smaller austenite grains and also smaller transformed martensite grains.
- XRD measurements revealed that the Si addition does not affect the martensite lattice parameters and the c/a ratio significantly.
- From EBSD and TKD measurements the OR between austenite and martensite was identified to be Greninger-Troiano for both alloys, FeNiC and FeNiCSi.
- APT results revealed that Si affects the segregation and partitioning behaviour in the vicinity of the phase interface. In FeNiC, C partitioning between austenite and martensite was observed, while Si significantly reduced C partitioning and led to a C increase at the phase boundary. Si forms a sigmoidal distribution at the phase boundary leading to a local Si depletion in the martensite and a corresponding increase in the austenite, which may have a barrier effect on C segregation.
- Combined APT and TEM analysis shows that C clusters form along fine (~10 nm thickness) twins in the martensite in both alloys hindering the formation of carbides and also reducing the driving force for C partitioning into the austenite.

Data Availability

The raw/processed data required to reproduce these findings cannot be shared at this time as the data also forms part of an ongoing study.

Declaration of Competing Interest

The authors declare that they have no known competing financial interests or personal relationships that could have appeared to influence the work reported in this paper.

Acknowledgement

The authors gratefully acknowledge funding by the Deutsche Forschungsgemeinschaft (DFG, German Research Foundation) through project 406912286 (C-TRAM).

References

[1] J.R.C. Guimarães, J.C. Gomes, A metallographic study of the influence of the austenite grain size on martensite kinetics, Acta Metall. 26 (10) (1978) 1591–1596.
[2] V. Raghavan, Formation sequence of plates in isothermal martensite transformation, Acta Metall. 17 (10) (1969) 1299–1303.
[3] G.V. Kurdyumov, L.G. Khandros, On the "thermoelastic" equilibrium on martensitic transformations, J. Tech. Phys. (1949).
[4] E.S. Machlin, M. Cohen, Burst phenomenon in the martensitic transformation, JOM 3 (9) (1951) 746–754.

[5] V. Danil'chenko, Martensite twinning in quenched steel, Scr. Metall. 23 (12) (1989) 2101–2104.
[6] G.V. Kurdjumov, A.G. Khachaturyan, Nature of axial ratio anomalies of the martensite lattice and mechanism of diffusionless $\gamma \rightarrow \alpha$ transformation, Acta Metall. 23 (9) (1975) 1077–1088.
[7] P. Winchell, M. Cohen, The Strength of Martensite, Massachusetts Inst of Tech Cambridge, 1962.
[8] L. Morsdorf et al., Multiple mechanisms of lath martensite plasticity, Acta Mater. 121 (2016) 202–214.
[9] L. Morsdorf et al., 3D structural and atomic-scale analysis of lath martensite: Effect of the transformation sequence, Acta Mater. 95 (2015) 366–377.
[10] P.C. Chen, B. Hall, P. Winchell, Atomic displacements due to C in Fe Ni C martensite, Metall. Trans. A 11 (8) (1980) 1323–1331.
[11] W.K. Choo, R. Kaplow, Mössbauer measurements on the aging of iron-carbon martensite, Acta Metall. 21 (6) (1973) 725–732.
[12] V. Danil'chenko, V. Sagaradze, P. l'Heritier, Martensite crystal structure of nickel steel at cryogenic temperatures, Mater. Sci. Eng. A 358 (1–2) (2003) 26–31.
[13] V. Gavriljuk, Distribution of Carbon in Steels, Naukova Dumka, 1987.
[14] G. Krauss, Martensite in steel: strength and structure, Mater. Sci. Eng. A 273–275 (1999) 40–57.
[15] M. Lesoille, P.M. Gielen, Mössbauer spectroscopy study of iron-carbon austenite and virgin martensite, Metall. Trans. 3 (10) (1972) 2681–2689.
[16] L. Lysak, B. Nikolin, Physical basis of heat treatment of steel, Met. Sci. Heat Treat. 20 (3) (1978) 255–257.
[17] C. Zener, Theory of strain interaction of solute atoms, Phys. Rev. - Phys Rev X 74 (1948) 639–647.
[18] K. Han et al., Initial stages of Fe-C martensite decomposition, Philos. Mag. A 81 (3) (2001) 741–757.
[19] M. Hayakawa, M. Tanigami, M. Oka, Low temperature aging of the freshly formed martensite in an Fe-Ni-C alloy, Metall. Trans. A 16 (10) (1985) 1745–1750.
[20] B. Kim, J. Sietsma, M. Santofimia, Thermodynamic aspects of carbon redistribution during ageing and tempering of Fe–Ni–C alloys, Phil. Mag. 96 (25) (2016) 2632–2648.
[21] M. Miller et al., An atom probe study of the aging of iron-nickel-carbon martensite, Metall. Trans. A 14 (6) (1983) 1021–1024.
[22] S. Nagakura et al., Crystallographic study of the tempering of martensitic carbon steel by electron microscopy and diffraction, Metall. Trans. A 14 (6) (1983) 1025–1031.
[23] R. Naraghi, M. Selleby, J. Ågren, Thermodynamics of stable and metastable structures in Fe–C system, Calphad 46 (2014) 148–158.
[24] G. Olson, M. Cohen, Early stages of aging and tempering of ferrous martensites, Metall. Trans. A 14 (6) (1983) 1057–1065.
[25] S. Ren et al., Electron diffraction study of aging processes in Fe-1.83 wt pct C martensite at room temperature, Metall. Mater. Trans. A 26 (8) (1995) 2001–2005.
[26] K. Taylor et al., Spinodal Decomposition During Aging of Fe—Ni—C Martensites, Metall. Trans. A 20 (1989) 2717–2737.
[27] K. Taylor et al., Carbide precipitation during stage I tempering of Fe-Ni-C martensites, Metall. Trans. A 20 (12) (1989) 2749–2765.
[28] K. Ullakko, V. Gavriljuk, V. Nadutov, Aging of freshly formed Fe-based martensites at low temperatures, Metall. Mater. Trans. A 25 (5) (1994) 889–909.
[29] M. Van Genderen et al., Aging and tempering behavior of iron-nickel-carbon and iron-carbon martensite, Metall. Mater. Trans. A 28 (3) (1997) 545–561.
[30] L. Morsdorf et al., Carbon redistribution in quenched and tempered lath martensite, Acta Mater. 205 (2021) 116521.
[31] M. Sarikaya, A.K. Jhingan, G. Thomas, Retained austenite and tempered martensite embrittlement in medium carbon steels, Metall. Trans. A 14 (6) (1983) 1121–1133.
[32] M.K. Miller, P.A. Beaven, G.D.W. Smith, A study of the early stages of tempering of iron-carbon martensites by atom probe field ion microscopy, Metall. Trans. A 12 (7) (1981) 1197–1204.
[33] J. Akré et al., The morphology of secondary-hardening carbides in a martensitic steel at the peak hardness by 3DFIM, Ultramicroscopy 109 (5) (2009) 518–523.
[34] G. Badinier et al., Microstructural heterogeneity and its relationship to the strength of martensite, Mater. Sci. Eng. A 638 (2015) 329–339.
[35] A. Böttger et al., Tempering of iron-carbon-nitrogen martensites:(Re) distribution of interstitial atoms, Materials science forum, Trans Tech Publ, 1999.
[36] F. Danoix et al., Atom probe tomography investigation of assisted precipitation of secondary hardening carbides in a medium carbon martensitic steels, J. Microsc. 244 (3) (2011) 305–310.
[37] D. Delagnes et al., Cementite-free martensitic steels: A new route to develop high strength/high toughness grades by modifying the conventional precipitation sequence during tempering, Acta Mater. 60 (16) (2012) 5877–5888.
[38] D. Pierce et al., Characterization of transition carbides in quench and partitioned steel microstructures by Mössbauer spectroscopy and complementary techniques, Acta Mater. 90 (2015) 417–430.
[39] G. Smith et al., Studies of dislocations by field ion microscopy and atom probe tomography, Phil. Mag. 93 (28–30) (2013) 3726–3740.
[40] H.P. Van Landeghem et al., Investigation of solute/interphase interaction during ferrite growth, Acta Mater. 124 (2017) 536–543.
[41] C. Zhu et al., Three-dimensional atom probe characterization of alloy element partitioning in cementite during tempering of alloy steel, Ultramicroscopy 107 (9) (2007) 808–812.
[42] B.P.J. Sandvik, C.M. Wayman, Direct observations of carbon clusters in a high-carbon martensitic steel, Metallography 16 (4) (1983) 429–447.
[43] M. Kusunoki, S. Nagakura, Modulated structure of iron-carbon martensite studied by electron microscopy and diffraction, J. Appl. Cryst. 14 (5) (1981) 329–336.
[44] M. Kusunoki, S. Nagakura, Incommensurate direction of the modulated structure in Iron-Carbon martensite, Trans. Jpn. Inst. Metals 25 (8) (1984) 517–522.
[45] S.S. Babu, K. Hono, T. Sakurai, APFIM studies on martensite tempering of Fe-C-Si-Mn low alloy steel, Appl. Surf. Sci. 67 (1) (1993) 321–327.
[46] N.C. Law, P.R. Howell, D.V. Edmonds, Structure of lath martensite and occurrence of retained austenite in as-quenched Fe-V-C low-alloy steels, Metal Science 13 (9) (1979) 507–515.
[47] H. Kwon, C.H. Kim, Tempered martensite embrittlement in Fe-Mo-C and Fe-W-C steel, Metall. Trans. A 14 (7) (1983) 1389–1394.
[48] R.A. Clark, G. Thomas, Design of strong tough Fe/Mo/C martensitic steels and the effects of cobalt, Metall. Trans. A 6 (5) (1975) 969–979.
[49] E. Kozeschnik, J.M. Vitek, Ortho-equilibrium and para-equilibrium phase diagrams for interstitial/substitutional iron alloys, Calphad 24 (4) (2000) 495–502.
[50] P. Samuel, L. Finch, J. Rait, A phase diagram for 1 per cent Carbon-Iron alloys containing up to 16 per cent Nickel, Nature 175 (4444) (1955) 37–38.
[51] M. Rao, R. Russell, P. Winchell, A correlation of thermodynamic variables for Iron-Nickel-Carbon alloys, AIME Me Soc Trans 239 (5) (1967).
[52] N. Lebrun, P. Perrot, Carbon – Iron – Nickel: Datasheet from Landolt-Börnstein - Group IV Physical Chemistry · Volume 11D2: "Iron Systems, Part 2" in SpringerMaterials (https://doi.org/10.1007/978-3-540-74196-1_10), G. Effenberg and S. Ilyenko, Editors., Springer-Verlag Berlin Heidelberg.
[53] G. Ghosh, G. Olson, Computational thermodynamics and the kinetics of martensitic transformation, J. Phase Equilib. 22 (3) (2001) 199–207.
[54] M. Umemoto, E. Yoshitake, I. Tamura, The morphology of martensite in Fe-C, Fe-Ni-C and Fe-Cr-C alloys, J. Mater. Sci. 18 (10) (1983) 2893–2904.
[55] J. Mola et al., Tempering of martensite and subsequent redistribution of Cr, Mn, Ni, Mo, and Si between cementite and martensite studied by magnetic measurements, Metall. Mater. Trans. A 48 (12) (2017) 5805–5812.
[56] D.H. Sherman et al., Characterization of the carbon and retained austenite distributions in martensitic medium carbon, high silicon steel, Metall. Mater. Trans. A 38 (8) (2007) 1698–1711.
[57] F. Bachmann, R. Hielscher, H. Schaeben, Texture analysis with MTEX – Free and open source software toolbox, Solid State Phenom. 160 (2010) 63–68.
[58] P.W. Trimby, Orientation mapping of nanostructured materials using transmission Kikuchi diffraction in the scanning electron microscope, Ultramicroscopy 120 (2012) 16–24.
[59] N. Brodusch, H. Demers, R. Gauvin, Nanometres-resolution Kikuchi patterns from materials science specimens with transmission electron forward scatter diffraction in the scanning electron microscope, J. Microsc. 250 (2013).
[60] K. Babinsky et al., A novel approach for site-specific atom probe specimen preparation by focused ion beam and transmission electron backscatter diffraction, Ultramicroscopy 144 (2014) 9–18.
[61] K. Leitner Née Babinsky et al., Atom probe study of grain boundary segregation in technically pure molybdenum, Mater Charact 87 (2014) 95–103.
[62] G.V. Kurdjumov, Martensite crystal lattice, mechanism of austenite-martensite transformation and behavior of carbon atoms in martensite, Metall. Trans. A 7 (7) (1976) 999–1011.
[63] L. Cheng et al., Lattice parameters of iron-carbon and iron-nitrogen martensites and austenites, Scr. Metall. Mater. 24 (3) (1990) 509–514.
[64] K. Honda, Z. Nishiyama, On the nature of the tetragonal and cubic martensites, Science Reports of Tohoku Imperial University 21 (1932) 299–331.
[65] G. Kurdumoff, E. Kaminsky, X-Ray studies of the structure of quenched Carbon steel, Nature 122 (3074) (1928) 475–476.
[66] Z. Nishiyama et al., Martensitic transformation, Academic Press, New York, 1978.
[67] E. Öhman, Crystal structure of martensite, Nature 127 (3199) (1931) 270–272.
[68] Y. Lu, Martensite lattice parameter measured by modern X-ray diffraction in Fe-C alloy, 2016.
[69] A. Shibata et al., Substructures of lenticular martensites with different martensite start temperatures in ferrous alloys, Acta Mater. 57 (2) (2009) 483–492.
[70] M. Seehaus, et al., Orientation relationship of FeNiC and FeNiCSi from variant detection in EBSD data, Archived on arXiv, (2023).
[71] K. Verbeken, L. Barbé, D. Raabe, Evaluation of the crystallographic orientation relationships between FCC and BCC phases in TRIP steels, ISIJ Int. 49 (10) (2009) 1601–1609.
[72] E.C. Bain, N. Dunkirk, *The nature of martensite.* trans, AIME 70 (1) (1924) 25–47.
[73] Z. Nishiyama, Science Reports of Tohoku Imperial University Tokio 23 (1934) 637–664.
[74] G. Kurdjumow, G. Sachs, Über den Mechanismus der Stahlhärtung, Z. Phys. 64 (5) (1930) 325–343.

[75] A.B. Greninger, A.R. Troiano, The mechanism of martensite formation, JOM 1 (9) (1949) 590–598.
[76] W. Pitsch, The martensite transformation in thin foils of iron-nitrogen alloys, Philosoph. Mag.: J. Theore. Experim. Appl. Phys. 4 (41) (1959) 577–584.
[77] C.C. Anya, T.N. Baker, The effect of silicon on the grain size and the tensile properties of low carbon steels, Mater. Sci. Eng. A 118 (1989) 197–206.
[78] S. Kajiwara, Roles of dislocations and grain boundaries in martensite nucleation, Metall. Mater. Trans. A 17 (10) (1986) 1693–1702.
[79] A. Shibata et al., Local orientation change inside lenticular martensite plate in Fe–33Ni alloy, Scr. Mater. 53 (5) (2005) 597–602.
[80] H. Sato, S. Zaefferer, A study on the formation mechanisms of butterfly-type martensite in Fe–30% Ni alloy using EBSD-based orientation microscopy, Acta Mater. 57 (6) (2009) 1931–1937.
[81] G.A. Thomas, J.G. Speer, Interface migration during partitioning of Q&P steel, Mater. Sci. Technol. 30 (9) (2014) 998–1007.
[82] K. Zilnyk et al., Misorientation distribution between martensite and austenite in Fe-31 wt%Ni-0.01 wt%C, Acta Mater. 143 (2018) 227.
[83] B. Kim, J. Sietsma, M. Santofimia, The role of silicon in carbon partitioning processes in martensite/austenite microstructures, Mater. Des. 127 (2017).
[84] C.A. Wert, Diffusion coefficient of C in alpha-Iron, Phys. Rev. 79 (4) (1950) 601–605.
[85] M.J. Santofimia et al., Influence of interface mobility on the evolution of austenite–martensite grain assemblies during annealing, Acta Mater. 57 (15) (2009) 4548–4557.
[86] W. Prause, The magnetic zener-relaxation and correlation factors in the pair model of chemical reactions, J. Magn. Magn. Mater. 2 (1) (1975) 230–241.
[87] I. Boesono et al., A Zener-damping peak in Fe-4 wt% Si, Physica Status Solidi (b) 19 (1) (1967) 107–110.
[88] K. Tanaka, The Zener relaxation effect in ferrous alloy systems, Trans. Jpn. Inst. Metals 16 (4) (1975) 199–205.
[89] P.E. Brommer, H.A.t Hooft, Magnetic Zener relaxation in iron - silicon alloys 26 (1967) 52–53.
[90] J. Escobar et al., Compositional analysis on the reverted austenite and tempered martensite in a Ti-stabilized supermartensitic stainless steel: Segregation, partitioning and carbide precipitation, Mater. Des. 140 (2018) 95–105.
[91] I. Souza Filho et al., Martensite to austenite reversion in a high-Mn steel: Partitioning-dependent two-stage kinetics revealed by atom probe tomography, in-situ magnetic measurements and simulation, Acta Mater. 166 (2019) 178–191.
[92] D. Simonovic et al., Diffusion of carbon in bcc Fe in the presence of Si, Phys. Rev. B 81 (5) (2010) 054116.
[93] H. Bhadeshia, R. Honeycombe, Chapter 9 - Tempering of Martensite, in Steels: Microstructure and Properties (Fourth Edition), H. Bhadeshia and R. Honeycombe, Editors. 2017, Butterworth-Heinemann. p. 237-270.
[94] G.V. Kurdjumov, A.G. Khachaturyan, Phenomena of carbon atom redistribution in martensite, Metall. Trans. 3 (5) (1972) 1069–1076.
[95] W. Lu et al., Formation of eta carbide in ferrous martensite by room temperature aging, Acta Mater. 158 (2018) 297–312.
[96] D.-H. Huang, G. Thomas, Metallography of bainitic transformation in silicon containing steels, Metall. Trans. A 8 (11) (1977) 1661–1674.
[97] J.I. Goldstein et al., Scanning Electron Microscopy and X-ray Microanalysis, Springer, 2017.
[98] K. Kanaya, S. Okayama, Penetration and energy-loss theory of electrons in solid targets, J. Phys. D Appl. Phys. 5 (1) (1972) 43.
[99] F. Caballero, M. Miller, C. Garcia-Mateo, Carbon supersaturation of ferrite in a nanocrystalline bainitic steel, Acta Mater. 58 (2010) 2338–2343.
[100] M. Herbig et al., Atomic-Scale quantification of grain boundary segregation in nanocrystalline material, Phys. Rev. Lett. 112 (12) (2014) 126103.
[101] B. Hutchinson et al., Microstructures and hardness of as-quenched martensites (0.1–0.5%C), Acta Mater. 59 (14) (2011) 5845–5858.
[102] Y.J. Li et al., Evolution of strength and microstructure during annealing of heavily cold-drawn 6.3GPa hypereutectoid pearlitic steel wire, Acta Mater. 60 (9) (2012) 4005–4016.

Chapter 6

OR of FeNiC and FeNiCSi from Variant Detection in EBSD Data

M. Seehaus[1], R. Pei[1], S. Korte-Kerzel[1], S. Sandlöbes-Haut[1]
[1]Institute of Physical Metallurgy and Materials Physics, RWTH Aachen University, Germany

Crystals 2023, 13, 663
Received: 6 March 2023
Accepted: 10 April 2023

The candidate carried out the conception, experimental work, formal analysis, data management and drafting of the manuscript for this publication. In collaboration with the co-authors, the methodology and software were developed and the final version of the manuscript was completed.

(Online availability: 10.3390/cryst13040663)

crystals

MDPI

Article

Orientation Relationship of FeNiC and FeNiCSi from Variant Detection in EBSD Data

Mattis Seehaus *, Risheng Pei, Sandra Korte-Kerzel and Stefanie Sandlöbes-Haut

Institute for Physical Metallurgy and Materials Physics, RWTH Aachen University, 52074 Aachen, Germany
* Correspondence: seehaus@imm.rwth-aachen.de

Abstract: The determination of orientation relationships in dual or multi-phase materials is very important in the field of interface engineering for the design of materials with tailored properties. In this work, a code is developed for the automated and statistical analysis of the orientation relationship of electron backscatter diffraction data. The code is applied to the example of Fe-Ni-(Si)-C alloys containing lenticular martensite and retained austenite, and it is shown that the orientation relationship (OR) corresponds to the Greninger–Troiano OR and that a statistically reliable investigation of the OR between the retained austenite and the related martensite variants is feasible using the code developed in this study.

Keywords: orientation relationship; EBSD; martensitic steel

Citation: Seehaus, M.; Pei, R.; Korte-Kerzel, S.; Sandlöbes-Haut, S. Orientation Relationship of FeNiC and FeNiCSi from Variant Detection in EBSD Data. *Crystals* **2023**, *13*, 663. https://doi.org/10.3390/cryst13040663

Academic Editors: Duc Nguyen-Manh and Raghvendra Singh Yadav

Received: 6 March 2023
Revised: 29 March 2023
Accepted: 10 April 2023
Published: 12 April 2023

1. Introduction

In the field of interface engineering, it is important to determine and identify the present orientation relationships (OR) between the different phases in dual or multi-phase materials. This helps to understand and tailor the material properties such as fracture toughness, strength, ductility and the mechanisms of (co-)deformation [1,2]. An example of materials with distinct ORs is steels containing martensite (bct) and austenite (fcc), whereby the character of the interphase boundary of the constituent phases affects the mechanical properties of the material. In these steels, the OR between neighbouring austenite and martensite grains is mostly investigated by transmission electron microscopy (TEM) due to the usually small grain sizes [3–7]. However, investigation by means of electron backscatter diffraction (EBSD) has been established in the last decade as a sufficiently performant method to investigate large, representative areas with respect to crystallographic information such as crystal structure (phase), grain orientation or misorientation across grain boundaries in martensitic, low-carbon or duplex steels [8–13].

The EBSD orientation maps, revealing the spatial orientation distribution, are recorded using a scanning electron microscope (SEM) and have the advantage of a higher statistical significance of the discovered ORs compared to the acquisition of individual orientation measurements in the TEM. The orientation maps obtained in this way contain a large amount of crystallographic data, which then leads to a statistically reliable analysis. Prior studies on the determination of ORs between martensite and austenite have revealed some advantages of EBSD over TEM, but have been carried out on individual laths only [14–16]. By reducing the acceleration voltage and/or using transmission Kikuchi diffraction (TKD) on thin (~100 nm) lamellae, the interaction volume between the electron beam and the sample can be reduced, enabling the measurement of small grains similar to TEM [17]. In contrast to the statistically low relevance of the TEM data, the large amount of orientation data obtained by EBSD provides the possibility to determine the differences between experimental pole figures and theoretical pole figures, calculated from the respective OR models [18].

A basic prerequisite for such investigations is an OR model. Typically, OR models define lattice directions and lattice planes. The statistically relevant identification

of ORs using austenitic–martensitic steels as an example is shown in this work. Examples of well-established OR models for these steels are the Kurdjumov–Sachs (KS) and Nishiyama–Wassermann (NW) orientation relationships, that were discovered in low-carbon steels on a single austenite grain after the martensitic transformation and in iron–nickel alloys (30% Ni), respectively [19–21]. These models appear in many studies to classify the OR of martensitic steels [10,22]. Plate martensite forms at temperatures down to those of liquid nitrogen, unlike lath martensite, resulting in a morphology of accommodated twins exhibiting the Greninger–Troiano (GT) OR [15,23–27]. However, in the case of lath martensite also, the GT OR was found to be the most dominant between martensite laths and retained austenite [28–30]. Investigations on thin Fe-N foils revealed the Pitsch-OR, which has also been studied theoretically [31,32]. However, the KS and NW OR models are considered untenable based on the high-indexed martensite habit planes and, moreover, numerous measurements show significant deviations from the ideal model conditions, which could still be referred to as near KS or near NW ORs [7,33]. In Table 1, the main ORs proposed or observed are summarised [14,15,34].

Table 1. Observed orientation relationships (ORs) between austenite, γ, and martensite, α', in steels.

OR	Plane	Direction
Bain	{100} γ//{100}α	<100> γ//<110> α
NW	{111} γ//{110} α	<112> γ//<110> α
KS	{111} γ//{110} α	<110> γ//<111> α
GT	{111} γ//{110} α	<123> γ//<133> α
Pitsch	{100} γ//{110} α	<110> γ//<111> α

In the present work, the OR between austenite and martensite is determined using TKD and EBSD in Fe-Ni-C-(Si) alloys, where lenticular martensite and retained austenite co-exist at room temperature. In steels, Si increases both the strength and the amount of retained austenite. Further, the addition of Si also increases the temperature at which stable C clusters can form, which prevents carbide precipitation like cementite during tempering [35–37]. A code was developed to automatically determine the ORs from the EBSD and TKD data. As a result of the large data sets resulting from these EBSD and TKD mappings, a statistically reliable determination with regard to the martensite/austenite ORs is feasible.

2. Experimental Procedure

The Fe-24 wt%Ni-0.4 wt%C and Fe-24 wt%Ni-0.4 wt%C-2 wt%Si alloy samples investigated (hereafter referred to as FeNiC and FeNiCSi, respectively) have been produced by casting, hot rolling at 1050 °C, subsequent cold rolling and recrystallisation treatment at 950 °C. At room temperature, these two materials are completely austenitic. The martensitic transformation takes place at temperatures below 0 °C, which facilitates the investigation of the austenitic microstructure at RT before the martensitic transformation. Quenching of only half of the samples in liquid nitrogen preserves a high proportion of austenite, which further enables the determination of the orientation relationship between α' and γ. Samples for microstructure characterisation were cut from the rolled sheet by electrical discharge machining, mechanically ground, polished to 0.25 µm with diamond suspension and finally electrolytically polished with A2 electrolyte (700 mL ethanol, 100 mL glycol butyl ether, 78 mL perchloric acid 60%) at 30 V for 30 s.

SEM and BSE images were taken to investigate the microstructure of the two alloys. Different substructures of the lenticular martensite are clearly visible, caused by the presence and absence of silicon, as shown in Figure 1. The midrib, characteristic of lenticular martensite, consists of a structure of fine transformation twins from which growth to the lenticular form is initiated.

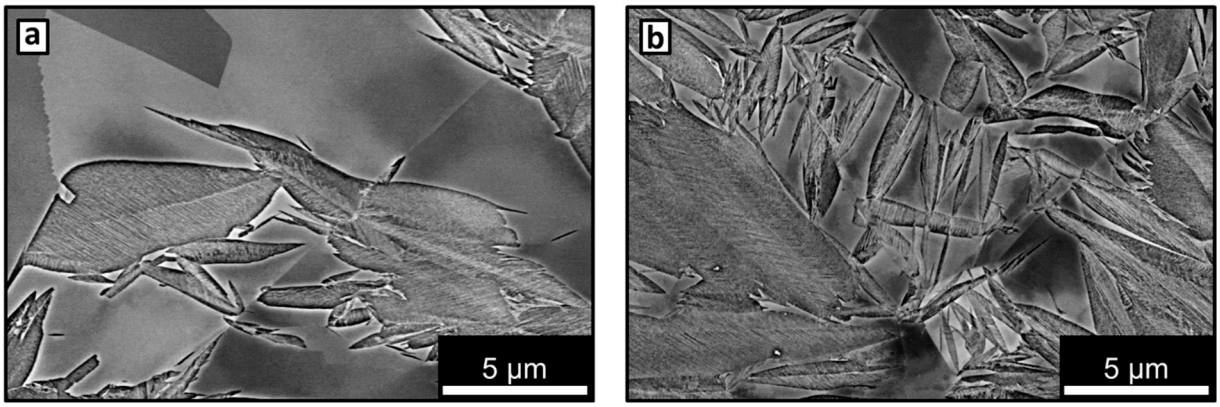

Figure 1. Microstructure of the lenticular martensite in (**a**) FeNiC and (**b**) FeNiCSi by means of backscatter electron imaging, respectively.

EBSD was applied to perform microstructure analysis in a FEG-SEM (Helios NanoLab 600i, FEI Co., Waltham, MA, USA) at 15 kV and 1.4 nA (Hikari, EDAX Inc., Pleasanton, CA, USA). The EBSD maps cover an area of 40 × 30 µm^2, were recorded with a step size of 150 nm and were analyzed using the free Matlab® toolbox MTEX 5.7.0 [38].

Code Development

For the identification of ORs, a code was developed that uses various methods for analysing two-phase or multi-phase materials in terms of orientation relationships and is accessible at [39]. In this work, the code is used with martensite and austenite in Fe-Ni-C(-Si) steels as an example.

In order to determine the orientation relationship between austenite and martensite, as well as to compare them, the austenite grains were detected from the EBSD maps of the partially transformed samples and their orientation matrices were rotated according to the standard projection along (001). In conjunction with this orientation transformation, the transformed martensite grains were selected and rotated with the corresponding rotation matrices with reference to the sample symmetry. Several different workflows are enabled and visualised in Figure 2.

The developed Matlab code enables the fully automated characterisation of an entire EBSD map and plotting of the result as pole figures. If only specific grains or individual interfaces of an EBSD are of interest, the manual selection of grains is also possible. Furthermore, the different modes can be used to correlate the orientations within a Phase 1 (parent phase) grain or individually selected EBSD data points with the Phase 2 (transformed) grain orientations.

In the automated mode, the EBSD data set is first arranged in descending order of the size of the Phase 1 grains and the orientations of a predefined number of the largest grains are stored. To improve statistics, this selection is expanded to all austenite grains that exhibit the same orientations within a deviation angle of $\varphi = 5°$. Furthermore, the adjacent Phase 1 grains that share a grain boundary with the filtered Phase 2 grains are assigned to them and their orientations are stored. Consequently, the Phase 2 grains are rotated to the standard orientation and the corresponding transformation matrices are stored in order to rotate the corresponding Phase 1 grains accordingly. In Figure 3, an example of an EBSD map of martensite and austenite, the corresponding phase map and the combined EBSD/phase map after completion of the code analysis are depicted.

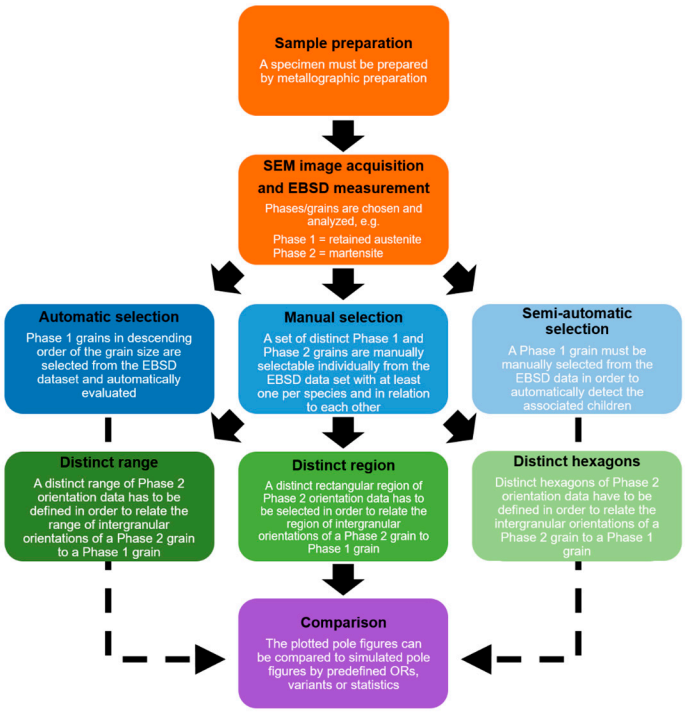

Figure 2. Workflow of the OR analysis code. Orange segments show preceding preparations and measurements, blue shows modes 1, 2 and 3, whereas green illustrates the three submodes of mode 2 and purple depicts potential analysis after the code has been executed.

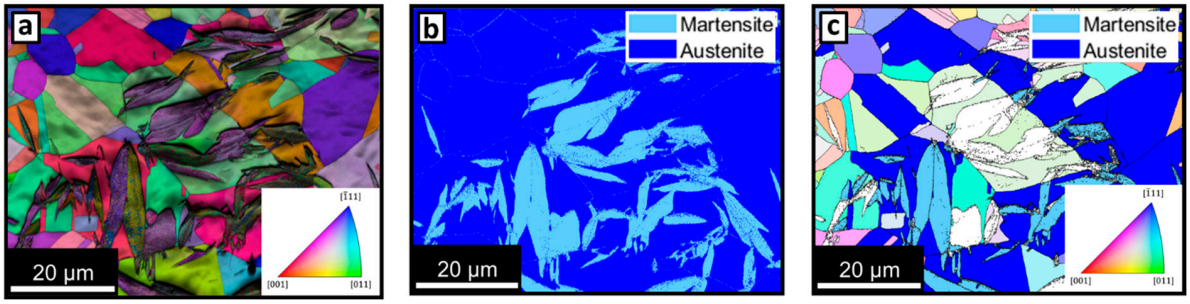

Figure 3. (**a**) EBSD map of FeNiC revealing the orientation data (**b**) phase map showing martensite/austenite grains, respectively and (**c**) combined EBSD/Phase map revealing both the analysed, selected austenite grains with the corresponding martensite grains in terms of their OR and the remaining unexamined grains according to their orientation.

Moreover, it is feasible to select individual Phase 2 grains and either automatically determine the respective fraction of (converted) Phase 1 grains originating from these grains, or select certain other Phase 1 grains and display them correlatively in the pole figures. In Figure 4a, such a combined EBSD/phase map is depicted with the three individual modes for partial intergranular orientation relationship plots. In Figure 4b, the intergranular orientations of a single martensite (green box in the extracted region of Figure 4c) are shown. Based on the adaptive selection method, the orientations of the individual martensite grains can be compared and plotted as a predefined pattern (Figure 4d), as a manually created rectangular area or as individual EBSD data points with the orientations of the parent phase, depending on the specific use case. Using this mode, it is feasible to analyse the OR in specific areas close to interfaces, as the ORs at individual interfaces may vary.

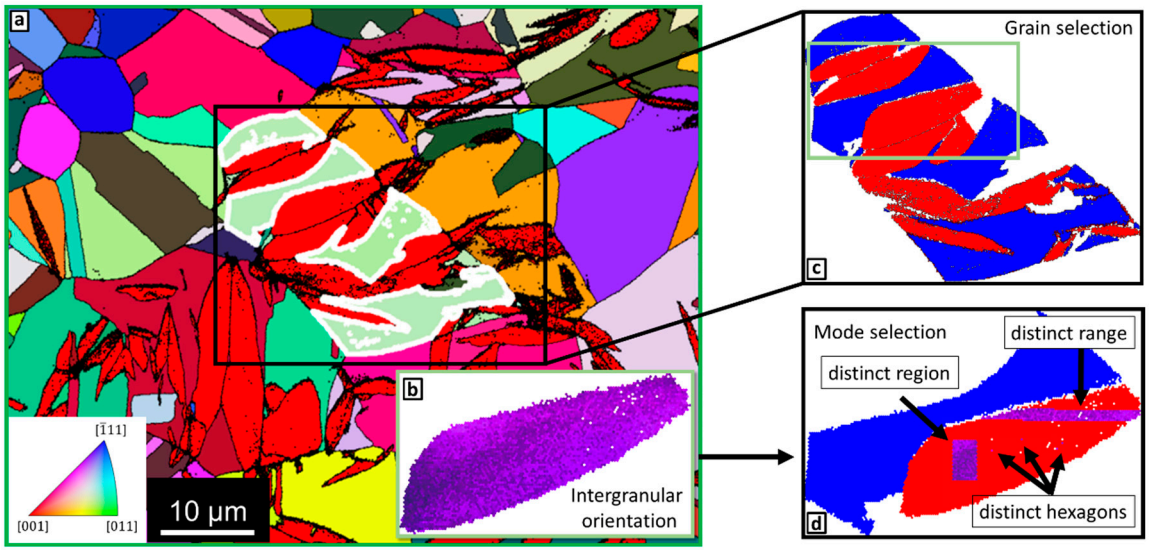

Figure 4. (**a**) Combined EBSD and phase map of FeNiC representing the mean austenite orientations as indicated by the inverse pole figure colour code with reference to the norm direction. The martensite is represented in red colour only. (**b**) Intergranular orientations of martensite and the corresponding austenite grain in (**c**); (**d**) distinct predefined range, individually selected rectangular area and individually predefined data points of the EBSD data within the martensite and the corresponding austenite grain. The white spots indicate non-indexed points.

3. Results

The procedures available in the code are demonstrated by using FeNiCSi. However, the analysis results of FeNiC obtained using the same procedures will be also presented in the final sections. Figure 5 shows the measured orientations of martensite and austenite of FeNiCSi and simulated pole figures of the possible ORs (Table 1), enabling direct comparison between experimentally measured and simulated orientation relationships, here using the (001), (011) and (111) pole figures. The blue orientations in the pole figures of FeNiCSi correspond to the austenite grains after rotation into the reference position.

An example of the semi-automatic selection of grains is depicted in Figure 6. The blue orientations in the pole figures of FeNiCSi correspond to the austenite grains after rotation into the reference position. Likewise, the rotation angle between the martensite and austenite orientations is utilised to identify the variants. The lowest rotation angle deviation, and thus the variant, is determined by comparison with martensite variants previously calculated based on the closest matching OR (Table 2), as exemplified in Figure 6d.

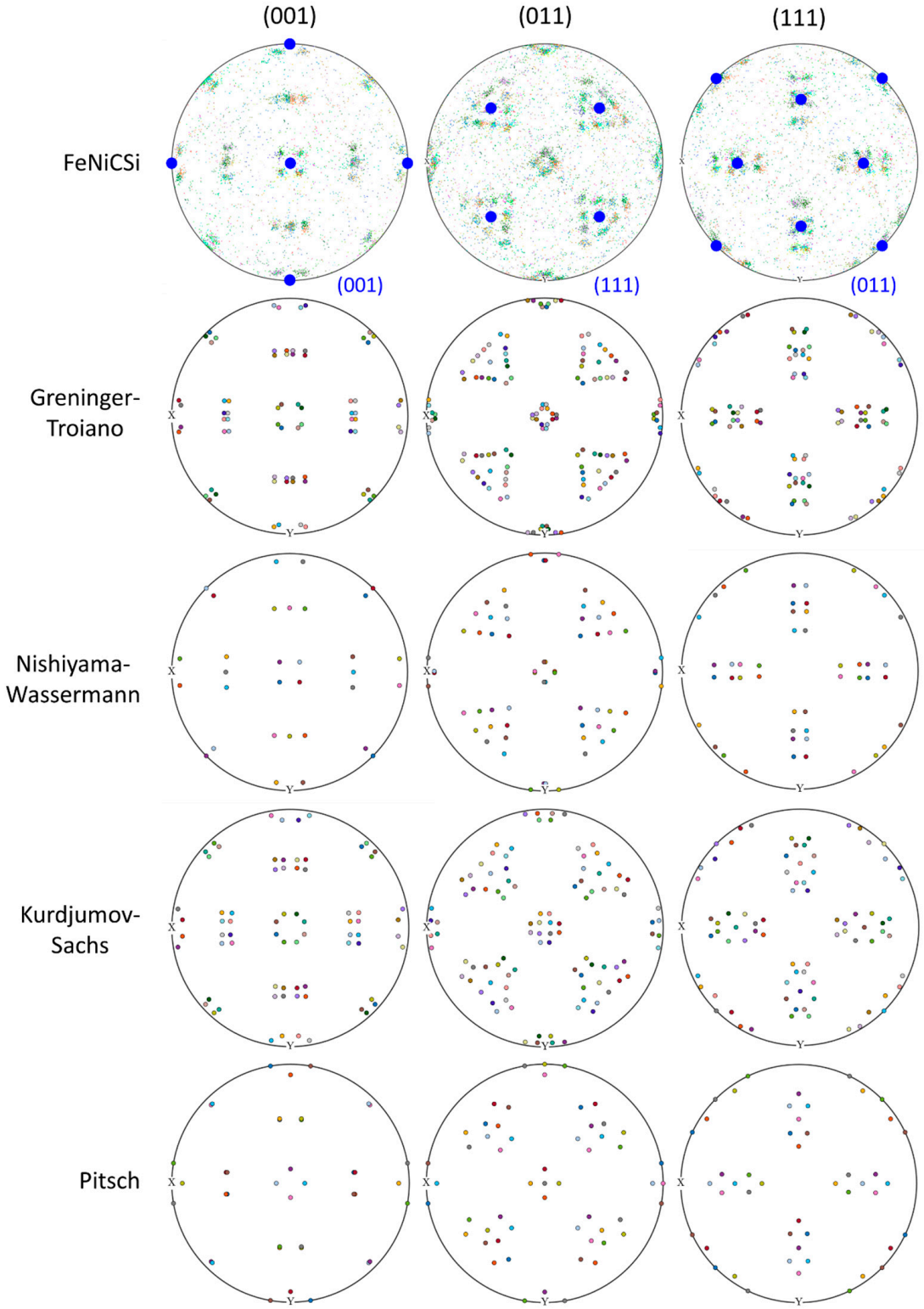

Figure 5. Pole figures calculated for different theoretical orientation relationships, namely Kurdjumov–Sachs (KS), Nishiyama–Wasserman (NW), Greninger–Troiano (GT), Pitsch and experimentally obtained data exemplarily shown for FeNiCSi, showing the reference austenite orientation in blue.

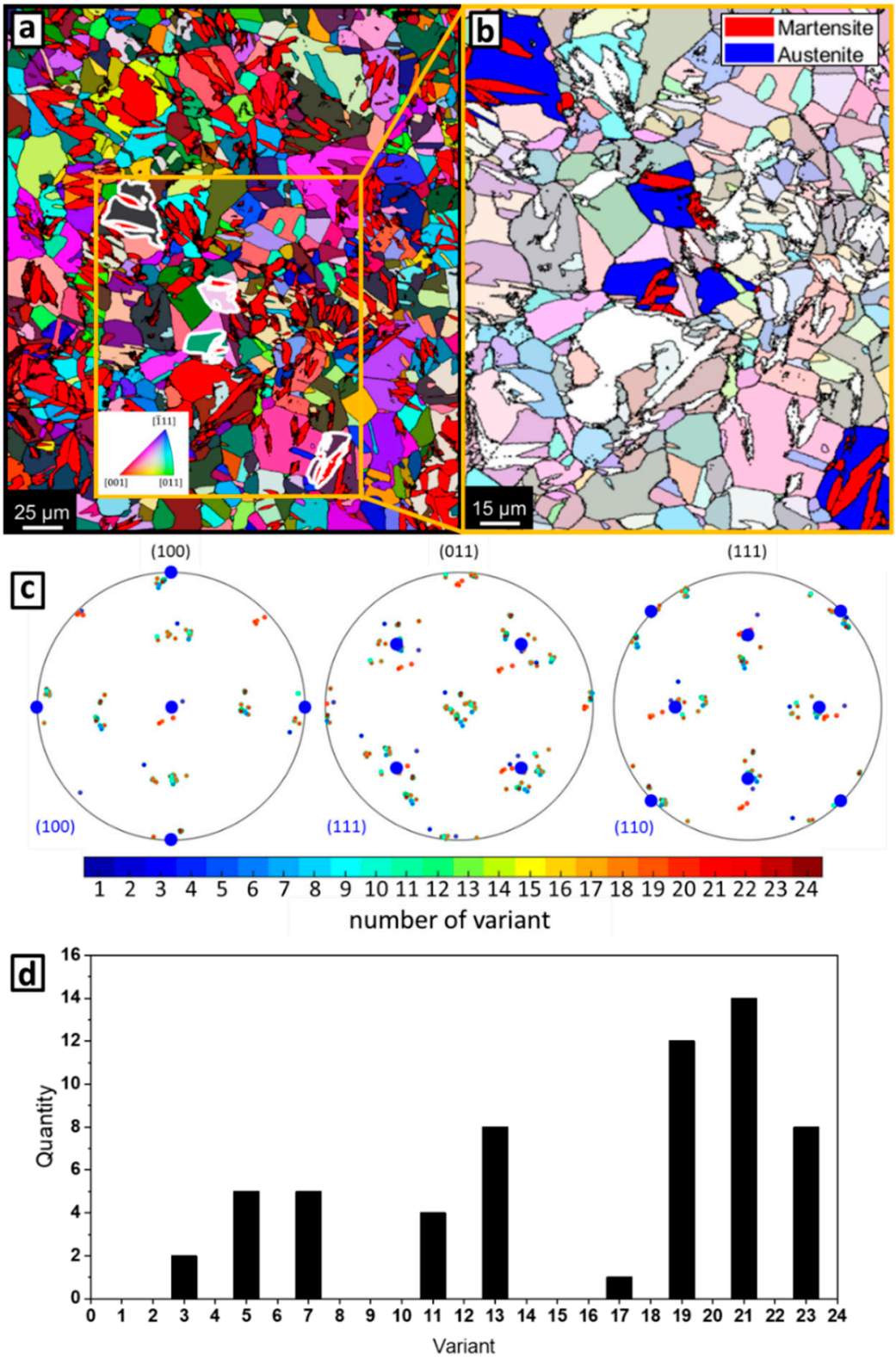

Figure 6. (**a**) Selection of grains to be analysed (white) with respect to their orientation relationship or variants. (**b**) Extraction and highlighting of the selected grains visualised in (**c**) for martensite with respect to the rotated austenite orientations shown in blue in the pole figure. (**d**) Histogram of the variants based on the smallest deviation of the rotation angle of the exemplary martensite variants from the extracted grains with respect to the possible simulated variants (here GT).

Table 2. Calculated variants from the GT OR.

Variant No.	Mis. Angle from V1	Rotation Axis from V1	φ_1	Φ	φ_2
1	0	-	324.79	170.10	191.32
2	55.26	[−0.71 0.00 0.71]	98.12	84.31	136.13
3	60	[−0.71 0.00 0.71]	351.88	95.70	316.13
4	4.74	[−0.71 0.00 0.71]	125.21	9.90	11.32
5	60	[−0.71 0.00 0.71]	275.75	98.08	46.94
6	60.25	[−0.53 0.53 0.66]	174.25	81.92	226.94
7	50.67	[−0.64 0.42 0.64]	261.88	95.70	316.13
8	16.61	[−0.69 0.23 0.69]	35.21	9.90	11.32
9	55.24	[−0.67 0.23 0.71]	185.75	98.08	46.94
10	50.14	[−0.47 0.57 0.68]	84.25	81.92	226.94
11	13.99	[−0.55 0.06 0.83]	234.79	170.10	191.32
12	50.65	[−0.67 0.26 0.70]	8.12	84.31	136.13
13	13.99	[−0.06 0.55 0.83]	54.79	170.10	191.32
14	50.14	[−0.57 0.47 0.68]	188.11	84.31	136.13
15	52.21	[−0.21 0.65 0.73]	81.88	95.70	316.13
16	11.60	[−0.69 0.19 0.69]	215.21	9.90	11.32
17	49.64	[−0.60 0.52 0.60]	5.75	98.08	46.94
18	56.85	[−0.19 0.66 0.72]	264.25	81.92	226.94
19	55.24	[−0.23 0.67 0.71]	354.25	81.92	226.94
20	50.65	[−0.26 0.67 0.70]	95.75	98.08	46.94
21	19.71	[−0.14 0.00 0.99]	305.21	9.90	11.32
22	56.84	[−0.66 0.19 0.72]	171.88	95.69	316.13
23	52.21	[−0.65 0.21 0.73]	278.11	84.31	136.13
24	19.80	[−0.20 0.00 0.98]	144.79	170.10	191.32

4. Discussion

An approach to compare the similarity of experimental data with potential orientation relationships is the analysis of the misorientation angles. The distributions of the misorientation angles of the martensite/austenite-phases are depicted in Figure 7, within a range of ±5° for FeNiC and FeNiCSi, respectively. The martensite–austenite misorientation profiles show clear peaks at a misorientation angle of about 44.05°, indicating that the Greninger–Troiano orientation relationship best matches the experimental data.

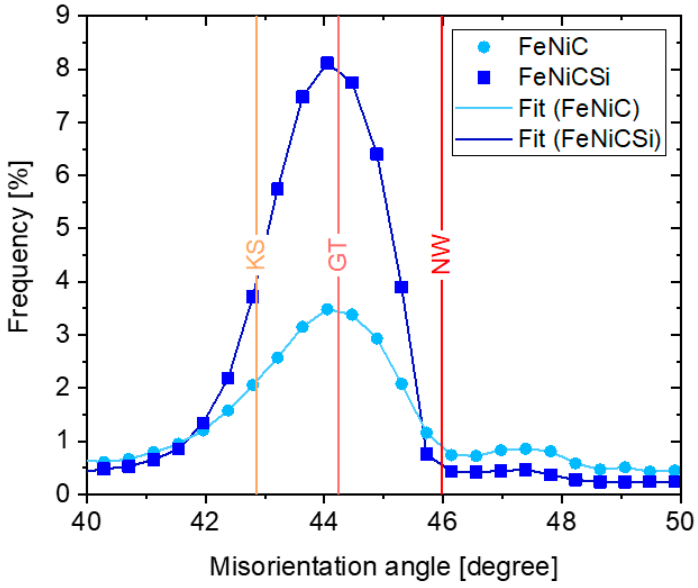

Figure 7. Misorientation angle distribution for FeNiC and FeNiCSi.

Specifically, the mean misorientation angle of FeNiC and FeNiCSi amounts to 44.43°, which is very close to the misorientation postulated by Greniger and Troiano, which lies between the KS and the NW orientation relationships (Table 3, Figure 7) [40].

Table 3. Overview of the different ORs between fcc and bcc crystals and the respective misorientation axis/angle.

OR	<uvw>	ω_{min}
Bain	<100>	45°
NW	<0.98 0.08 0.20>	45.98°
KS	<0.97 0.18 0.18>	42.85°
GT	<0.97 0.19 0.13>	44.23°
Pitsch	<0.08 0.20 0.98>	45.98°

The analysis of the misorientation angle is not always sufficient to accurately determine an OR. To confirm this finding, a subsequent pole figure analysis can be performed. As an approach to validate the obtained OR, normalised cross correlation (NCC), an inverse Fourier transform of the convolution of the Fourier transform of, e.g., two images, can be applied [41,42]. The normalisation is then done using the local cumulative sums and standard deviations. This type of correlation helps to ascertain the agreement between two data sets and has been applied to compare the simulated and experimental pole figures of the automatic selection mode visually, in order to obtain quantitative correlation coefficients. In Figure 8a–c, the subtracted simulated and experimental (001), (011) and (111) pole figures of FeNiCSi are depicted. In addition, the correlation factors of the possible ORs given in Table 1 are shown in Figure 8d, indicating that the dominant OR in both alloys corresponds to the GT OR with the highest correlation factors. The effects of Si on the initial austenite grain sizes, and hence on the thermally transformed martensites, have no major impact on the determination of the OR as GT for both FeNiC and FeNiCSi in this work.

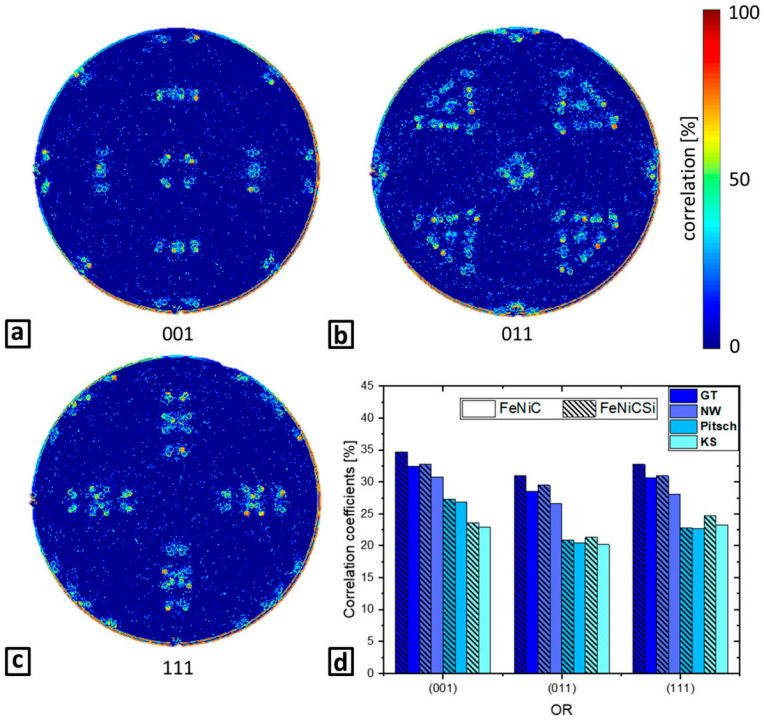

Figure 8. Subtraction of simulated (here GT) from experimental (**a**) (001) (**b**) (011) and (**c**) (111) pole figures for FeNiCSi; (**d**) Correlation coefficients of FeNiC and FeNiCSi, respectively, with the simulated pole figures to enable quantitative analysis.

As another approach to statistically analyse the experimentally measured and the simulated pole figures, the orientation data were compared in terms of the minimum deviation of the rotation angles between the measured orientation and all martensite variants of the respective ORs, according to a certain threshold value. Figure 9a displays the experimental raw data of the (011) pole figure, while b and c present the filtered experimental data for a minimum rotation angle deviation with a threshold of <10° and <5°, respectively. For a threshold value of <5°, about ~86% of all orientations of the original EBSD map are preserved, allowing a statistical analysis of the large majority of the experimental data. As a result of multiple phases or grain boundaries in material systems, the EBSD measurement is partially unable to assign the correct diffraction patterns unambiguously. By comparing all ORs at the different threshold values and the average values of both alloys, the smallest rotational deviations are obtained for the GT OR, demonstrating that the misorientation distribution and combined pole figure comparison are suitable to determine orientation relationships.

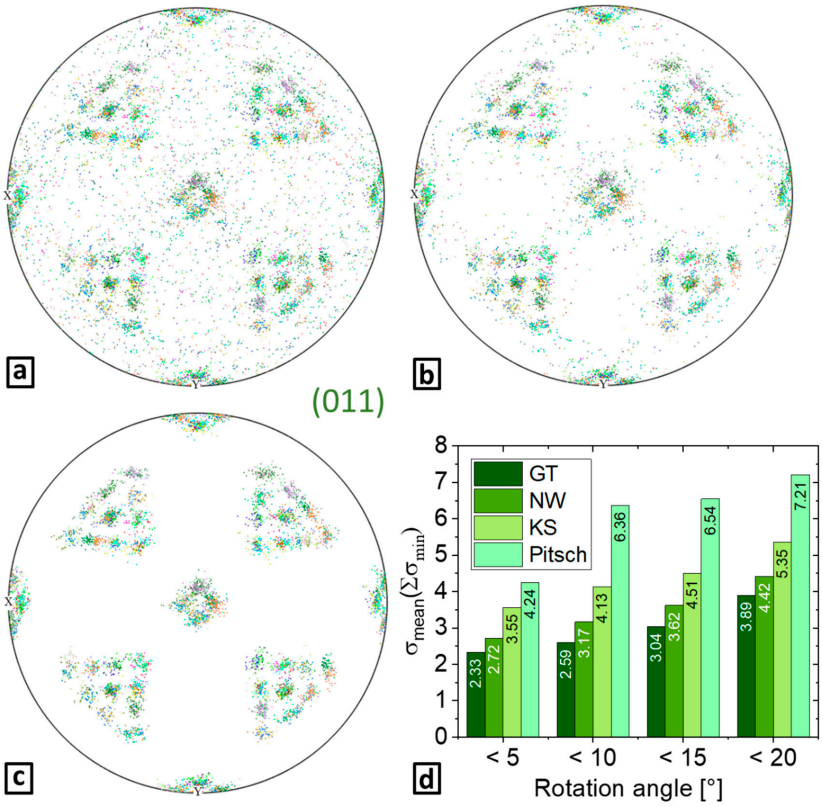

Figure 9. Pole figures of the raw and filtered orientation data measured for FeNiCSi and the statistical evaluation of the orientation data exemplary for the (011) pole figure. (**a**) Raw pole figure, (**b**) pole figure filtered by rotation angle deviation <10° and (**c**) pole figure filtered by rotation angle deviation <5° and (**d**) histograms showing the mean values for each set of minimum rotation angle deviation for each OR revealing that the lowest rotational deviations are present for the GT orientation relationship.

Table 4 presents the correlation coefficients and rotational deviations of FeNiC and FeNiCSi when considering the possible orientation relationships given in Table 1. The higher the correlation coefficient of the experimental data with one of the possible ORs, the higher the similarity between them. Similarly, a lower rotational deviation indicates higher similarity. In the present examples, all methods to determine the OR show the highest match with the GT OR.

Table 4. Mean correlation coefficients C_{corr} and mean orientation angle deviation σ calculated for FeNiC and FeNiCSi.

OR	NW	KS	GT	Pitsch
Mean C_{corr} (FeNiC)	28.50	24.05	30.51	23.33
Mean C_{corr} (FeNiCSi)	31.05	25.41	32.84	23.66
Mean σ (FeNiC) [°]	3.48	4.39	2.97	6.09
Mean σ (FeNiCSi) [°]	3.70	4.54	3.12	6.04

The experimental data of the martensite variants of both FeNiC and FeNiCSi, presented in austenite reference pole figures in this work (Figure 5), provide a statistically close correspondence with the GT OR, in comparison with other established ORs like KS, NW or Pitsch. It has been shown that the code developed for identifying orientation relationships gives quite unambiguous results for reasonably accurate EBSD and/or TKD data sets. The main component is the automatically generated statistical evaluation of all grain orientations within an entire EBSD/TKD measurement and relating them to a predefined orientation relationship. In addition, the reference systems can be modified. In principle, the code was designed as a workflow for several use cases with some defined pre-settings, but it is also intended to be kept as user-friendly as possible, which means that functional components can be adjusted in the respective source codes. It is mainly optimised for two-phase systems, but can also visualise at least individual orientation relationships in multi-phase systems through the manual selection of grains. If the EBSD/TKD map quality is insufficient for a statistical evaluation, manual grain selection may be an option to determine the orientation relationship of individual areas. Since the local misorientations within individual grains can diverge significantly, the manual mode enables the visualisation of the orientation relationship of single, acquired orientation spots or areas within a grain. Although this method could also be useful for, e.g., phase shape memory alloys (Ti-Ni [43,44]) or intermetallic phases (Mg-Ag-Al [45]), it has so far only been investigated for the material systems described in this work.

The aforementioned concept is limited to use cases in which grains of both phases and their boundaries remain for OR analysis. Thus, it is not applicable after a complete phase transformation without including data of the initial phase from another measurement and adjusting the code specifically for this use case. In the case of only small, untransformed, retained austenite fractions, the orientation may deviate from the orientation of the initial state due to the plastic accommodation caused by the strain resulting from the martensitic transformation [46]. For such applications, methods have been developed that determine the OR mainly on the basis of the transformed phase or the martensite variants, and the results could be verified or adjusted using the manual mode of the present work [29–31,47]. Micromechanical effects, such as strain fields or distortions between neighbouring martensite variants, could have an influence on the crystal orientation of the martensite variants, which complicates a precise differentiation of individual ORs [48]. In an Fe-24Ni-0.3C alloy, by comparing ultrafine with coarse-grained austenitic microstructure, it was observed that the martensite/austenite interface exhibited the GT OR on both sides in coarse grains and the KS OR on the outer side of the martensite in ultrafine grains [49]. In an Fe-33Ni alloy, it was found that the OR in lenticular martensite varied from the midrib (GT) to the austenite/martensite interface (KS) [15]. However, in an Fe-31%Ni-0.01C alloy, where partially transformed lenticular martensite in conjunction with austenite was present, it was reported that although there is a scatter of orientations, near both the interface and the midrib, the misorientations are closer to the GT orientation, resulting in the OR being the same between the midrib and the interfacial region [50]. Due to the potential existence of several ORs in one material, and to enable a more representative demonstration of the ORs, further work is required.

All the codes discussed in this work are maintained in an online repository available at the following reference: [39].

5. Conclusions

A Matlab® code based on the MTEX toolbar for the quantitative identification of orientation relationships with statistical relevance has been developed. As an example, the OR between retained austenite and martensite was determined and statistically evaluated. From our study, the following conclusions have been derived:

- The code contains different modes that can be used for an in-depth analysis of obtained ORs, specifically the automatic, semi-automatic and manual selection of grains or microstructure areas.
- The automatic mode allows a statistically relevant and fully automatic evaluation of the orientation relationship of a large range of grains and thereby allows the determination of the predominant OR. This is done by comparing the pole figures of the corresponding phases of interest, e.g., retained parent austenite grains and the adjacent martensite grains, with a calculated theoretical orientation relationship.
- Additionally, the manual evaluation mode provides local insights into the precise OR for chosen grains or individual interfaces, and in the present case a determination of the occurring martensite variants was possible. The selection of individual measurement points instead of whole grains is also possible, and could be used to evaluate the behavioural impact of intragranular misorientations on the OR or be applied if the indexing rate of the EBSD data is low.
- Exemplarily, the code was applied to an austenitic–martensitic steel where the successful identification and evaluation of the OR between austenite and martensite was demonstrated. The comparison of the misorientation angle distribution with the misorientation angles of specific ORs supports the identification of the Greninger–Troiano OR for both FeNiC and FeNiCSi. This was further confirmed by an image correlation algorithm, comparing calculated theoretical variants with the experimental pole figures.
- For quantitative analysis of the observed OR, the minimum rotation angle deviations between the experimental and the theoretically calculated orientation relationships were determined for different ORs. This method was successfully applied to confirm the previously identified Greninger–Troiano OR for the present example case.
- Although the capabilities of the developed code on the example of martensite and austenite in steels have been demonstrated, it can be used for many other applications where an orientation relationship between different phases is relevant. An adaptation of the present method for the investigation of ORs in other material systems, such as intermetallic phases, shape memory alloys, thin films or other composite materials, could provide insights into the existing ORs.

Author Contributions: Conceptualization, M.S.; methodology, M.S. and R.P.; software, M.S. and R.P.; writing—original draft preparation, M.S.; writing—review and editing, S.S.-H. and S.K.-K.; supervision, S.S.-H.; project administration, S.S.-H.; funding acquisition, S.S.-H. All authors have read and agreed to the published version of the manuscript.

Funding: This research was funded by DFG grant number 406912286.

Data Availability Statement: The raw/processed data required to reproduce these findings cannot be shared at this time as the data also form part of an ongoing study.

Acknowledgments: The authors gratefully acknowledge funding by the Deutsche Forschungsgemeinschaft (DFG, German Research Foundation) through project 406912286 (C-Tram).

Conflicts of Interest: The authors declare no conflict of interest.

References

1. Asghari-Rad, P.; Nili-Ahmadabadi, M.; Shirazi, H.; Hossein Nedjad, S.; Koldorf, S. A significant improvement in the mechanical properties of AISI 304 stainless steel by a combined RCSR and annealing process: A significant improvement in the mechanical properties. *Adv. Eng. Mater.* **2016**, *19*, 1600663. [CrossRef]
2. Ren, J.; Li, C.; Han, Y.; Li, E.; Gao, C.; Qiu, C. Effect of initial martensite and tempered carbide on mechanical properties of $_3Cr_2$MnNiMo mold steel. *Mater. Sci. Eng. A* **2021**, *812*, 141080. [CrossRef]

3. Ameyama, K.; Weatherly, G.; Aust, K. A study of grain boundary nucleated widmanstätten precipitates in a two-phase stainless steel. *Acta Metall. Mater.* **1992**, *40*, 1835–1846. [CrossRef]
4. Chen, T.H.; Yang, J.-R. Microstructural characterization of simulated heat affected zone in a nitrogen-containing 2205 duplex stainless steel. *Mater. Sci. Eng. A* **2002**, *338*, 166–181. [CrossRef]
5. Shek, C.H.; Lai, J.K.L.; Wong, K.W.; Dong, C. Early-stage widmanstatten growth of the γ phase in a duplex steel. *Met. Mater. Trans. A* **2000**, *31*, 15–19. [CrossRef]
6. Shtansky, D.V.; Nakai, K.; Ohmori, Y. Crystallography and structural evolution during reverse transformation in an Fe–$_{17}$Cr–$_{0.5}$C tempered martensite. *Acta Mater.* **2000**, *48*, 1679–1689. [CrossRef]
7. Zhang, M.-X.; Kelly, P. Accurate orientation relationship between ferrite and austenite in low carbon martensite and granular bainite. *Scr. Mater.* **2002**, *47*, 749–755. [CrossRef]
8. Brückner, G.; Pospiech, J.; Seidl, I.; Gottstein, G. Orientation correlation during diffusional α→γ phase transformation in a ferritic low carbon steel. *Scr. Mater.* **2001**, *44*, 2635–2640. [CrossRef]
9. Bugat, S.; Besson, J.; Gourgues, A.-F.; N'Guyen, F.; Pineau, A. Microstructure and damage initiation in duplex stainless steels. *Mater. Sci. Eng. A* **2001**, *317*, 32–36. [CrossRef]
10. Gourgues, A.-F.; Flower, H.M.; Lindley, T.C. Electron backscattering diffraction study of acicular ferrite, bainite, and martensite steel microstructures. *Mater. Sci. Technol.* **2000**, *16*, 26–40. [CrossRef]
11. Morito, S.; Tanaka, H.; Konishi, R.; Furuhara, T.; Maki, T. The morphology and crystallography of lath martensite in Fe-C alloys. *Acta Mater.* **2003**, *51*, 1789–1799. [CrossRef]
12. Suh, D.-W.; Kang, J.-H.; Oh, K.H.; Lee, H.-C. Evaluation of the deviation angle of ferrite from the Kudjumov–Sachs relationship in a low carbon steel by EBSD. *Scr. Mater.* **2002**, *46*, 375–378. [CrossRef]
13. Ueda, M.; Yasuda, H.; Umakoshi, Y. Stress-induced martensitic transformation in Fe–Ni bicrystals. *Acta Mater.* **2001**, *49*, 4251–4258. [CrossRef]
14. Sato, H.; Zaefferer, S. A study on the formation mechanisms of butterfly-type martensite in Fe–30% Ni alloy using EBSD-based orientation microscopy. *Acta Mater.* **2009**, *57*, 1931–1937. [CrossRef]
15. Shibata, A.; Morito, S.; Furuhara, T.; Maki, T. Local orientation change inside lenticular martensite plate in Fe–33Ni alloy. *Scr. Mater.* **2005**, *53*, 597–602. [CrossRef]
16. Yardley, V.; Payton, E. Austenite–martensite/bainite orientation relationship: Characterisation parameters and their application. *Mater. Sci. Technol.* **2014**, *30*, 1125–1130. [CrossRef]
17. Brodusch, N.; Demers, H.; Gauvin, R. Nanometres-resolution Kikuchi patterns from materials science specimens with transmission electron forward scatter diffraction in the scanning electron microscope. *J. Microsc.* **2013**, *250*, 2635–2640. [CrossRef]
18. Nolze, G. *Determination of Orientation Relationships between Fcc/Bcc Lattices by the Use of Pole Figures*; HKL Usermeeting: Ribe, Denmark, 2004; pp. 1–9.
19. Nishiyama, Z. *Science Reports of Tohoku Imperial University Tokyo*; University of Tokyo: Tokyo, Japan, 1934; Volume 23, pp. 637–664.
20. Wassermann, G. *Über den Mechanismus der Alpha-Gamma-Umwandlung des Eisens*; Stahleisen: Düsseldorf, Germany, 1935.
21. Kurdjumow, G.; Sachs, G. Über den Mechanismus der Stahlhärtung. *Z. Phys.* **1930**, *64*, 325–343. [CrossRef]
22. Gardiola, B.; Esling, C.; Humbert, M.; Hensger, K.E. EBSD Study of the γ to α phase transormation in an CSP–HSLA Steel. *Adv. Eng. Mater.* **2003**, *5*, 583–586. [CrossRef]
23. Maki, T. Microstructure and mechanical behaviour of ferrous martensite. In *Materials Science Forum*; Trans Tech Publications Ltd.: Zurich, Switzerland, 1990.
24. Umemoto, M.; Yoshitake, E.; Tamura, I. The morphology of martensite in Fe-C, Fe-Ni-C and Fe-Cr-C alloys. *J. Mater. Sci.* **1983**, *18*, 2893–2904. [CrossRef]
25. Maki, T.; Shimooka, S.; Umemoto, M.; Tamura, I. The Morphology of Strain-Induced Martensite and Thermally Transformed Martensite in Fe–Ni–C Alloys. *Trans. Jpn. Inst. Met.* **1972**, *13*, 400–407. [CrossRef]
26. Maki, T.; Wayman, C. Effect of coherent precipitates in austenite on the martensite substructure in an Fe-Ni-Ti-C alloy. *Acta Met.* **1977**, *25*, 695–710. [CrossRef]
27. Nishiyama, Z.; Shimizu, K.; Sugino, K. The martensite transformation in thin foils. *Acta Met.* **1961**, *9*, 620–622. [CrossRef]
28. Sun, D.; Guo, Z.; Gu, J. The microstructure and crystallography of lath martensite with Greninger-Troiano orientation relationship in a Fe-$_{12.8}$Ni-$_{1.5}$Si-$_{0.22\%}$C steel. *Mater. Charact.* **2021**, *181*, 111501. [CrossRef]
29. Sun, D.; Li, C.; Xue, X.; Liu, Y.; Guo, Z.; Gu, J. Optimization scheme of the orientation relationship from crystallographic statistics of variants and its application to lath martensite. *Mater. Des.* **2020**, *195*, 109022. [CrossRef]
30. Wang, C.; Qiu, H.; Kimura, Y.; Inoue, T. Morphology, crystallography, and crack paths of tempered lath martensite in a medium-carbon low-alloy steel. *Mater. Sci. Eng. A* **2016**, *669*, 48–57. [CrossRef]
31. Koumatos, K.; Muehlemann, A. A theoretical investigation of orientation relationships and transformation strains in steels. *Acta Crystallogr. Sect. A Found. Adv.* **2017**, *73*, 115–123. [CrossRef]
32. Pitsch, W. The martensite transformation in thin foils of iron-nitrogen alloys. *Philos. Mag. A J. Theor. Exp. Appl. Phys.* **1959**, *4*, 577–584. [CrossRef]
33. Greninger, A.B.; Troiano, A.R. The mechanism of Martensite formation. *JOM* **1949**, *1*, 590–598. [CrossRef]
34. Shibata, A.; Murakami, T.; Morito, S.; Furuhara, T.; Maki, T. The Origin of Midrib in Lenticular Martensite. *Mater. Trans.* **2008**, *49*, 1242–1248. [CrossRef]

35. Mola, J.; Luan, G.; Brochnow, D.; Volkova, O.; Wu, J. Tempering of Martensite and Subsequent Redistribution of Cr, Mn, Ni, Mo, and Si Between Cementite and Martensite Studied by Magnetic Measurements. *Met. Mater. Trans. A* **2017**, *48*, 5805–5812. [CrossRef]
36. Scheer, L. *Was ist Stahl?: Einführung in die Stahlkunde für Jedermann*; Springer: Berlin, Germany, 2013.
37. Sherman, D.H.; Cross, S.M.; Kim, S.; Grandjean, F.; Long, G.J.; Miller, M.K. Characterization of the Carbon and Retained Austenite Distributions in Martensitic Medium Carbon, High Silicon Steel. *Metall. Mater. Trans. A* **2007**, *38*, 1698–1711. [CrossRef]
38. Bachmann, F.; Hielscher, R.; Schaeben, H. Texture Analysis with MTEX—Free and Open Source Software Toolbox. *Solid State Phenom.* **2010**, *160*, 63–68. [CrossRef]
39. Seehaus, M.; Pei, R. ORs from EBSD. 2022. Available online: https://github.com/Mattis-Seehaus/ORs_from_EBSD (accessed on 31 July 2022).
40. Verbeken, K.; Barbé, L.; Raabe, D. Evaluation of the crystallographic orientation relationships between FCC and BCC phases in TRIP steels. *ISIJ Int.* **2009**, *49*, 1601–1609. [CrossRef]
41. Haralick, R.M.; Shapiro, L.G. *Computer and Robot Vision*; Addison-Wesley Reading: Boston, MA, USA, 1992; Volume 1.
42. Lewis, J. *Fast Normalized Cross-Correlation 1995*; Industrial Light & Magic: San Francisco, CA, USA, 2011.
43. Buchheit, T.E.; Wert, J.A. Predicting the orientation-dependent stress-induced transformation and detwinning response of shape memory alloy single crystals. *Metall. Mater. Trans. A* **1996**, *27*, 269–279. [CrossRef]
44. Nishida, M.; Nishiura, T.; Kawano, H.; Inamura, T. Self-accommodation of B19′ martensite in Ti–Ni shape memory alloys—Part I. Morphological and crystallographic studies of the variant selection rule. *Philos. Mag.* **2012**, *92*, 2215–2233. [CrossRef]
45. Lv, S.; Lu, X.; Li, Y.; Meng, F.; Hua, X.; Yang, Q.; Qiu, X.; Meng, J.; Duan, Q. Crystallographic orientation relationships between the aggregated intermetallic phases in a casting Mg-Ag-Al alloy. *Mater. Des.* **2020**, *190*, 108561. [CrossRef]
46. Miyamoto, G.; Takayama, N.; Furuhara, T. Accurate measurement of the orientation relationship of lath martensite and bainite by electron backscatter diffraction analysis. *Scr. Mater.* **2009**, *60*, 1113–1116. [CrossRef]
47. Kinney, C.C.; Pytlewski, K.R.; Khachaturyan, A.G.; Morris, J.W., Jr. The microstructure of lath martensite in quenched 9Ni steel. *Acta Mater.* **2014**, *69*, 372–385. [CrossRef]
48. Thome, P.; Schneider, M.; Yardley, V.A.; Payton, E.J.; Eggeler, G. Crystallographic Analysis of Plate and Lath Martensite in Fe-Ni Alloys. *Crystals* **2022**, *12*, 156. [CrossRef]
49. Jafarian, H.R.; Borhani, E.; Shibata, A.; Terada, D.; Tsuji, N. Martensite/austenite interfaces in ultrafine grained Fe–Ni–C alloy. *J. Mater. Sci.* **2011**, *46*, 4216–4220. [CrossRef]
50. Zilnyk, K.; Junior, D.R.D.A.; Sandim, H.; Rios, P.; Raabe, D. Misorientation distribution between martensite and austenite in Fe-31 wt%Ni-0.01 wt%C. *Acta Mater.* **2017**, *143*, 227–236. [CrossRef]

Chapter 7

Estimation of directional single crystal elastic properties from nano-indentation by correlation with EBSD and first-principle calculations

M. Seehaus[1], S.-H. Lee[1], T. Stollenwerk[1], J.-M. Wheeler[2], S. Korte-Kerzel[1]
[1]Institute of Physical Metallurgy and Materials Physics, RWTH Aachen University, Germany
[2]ETH Zürich, Switzerland

Materials & Design 234 (2023) 112296
Received: 30 June 2023
Accepted: 30 August 2023

The candidate carried out the conception, experimental work, formal analysis, data management and drafting of the manuscript for this publication. In collaboration with the co-authors, the methodology and software were developed and the final version of the manuscript was completed.

(Online availability: j.matdes.2023.112296)

Materials & Design 234 (2023) 112296

Contents lists available at ScienceDirect

Materials & Design

journal homepage: www.elsevier.com/locate/matdes

Estimation of directional single crystal elastic properties from nano-indentation by correlation with EBSD and first-principle calculations

Mattis Seehaus [a,1,*], Sang-Hyeok Lee [a,1], Tobias Stollenwerk [a], Jeffrey M. Wheeler [b,c], Sandra Korte-Kerzel [a]

[a] Institut für Metallkunde und Materialphysik, RWTH Aachen University, 52074 Aachen, Germany
[b] Laboratory of Metal Physics and Technology, Department of Materials, ETH Zürich, 8093 Zurich, Switzerland
[c] FemtoTools AG, Furtbachstrasse 4, CH-8107 Buchs/ZH, Switzerland

ARTICLE INFO

Keywords:
Nano-indentation
Stiffness tensor
Least-squares optimisation
Austenitic steel
Meteorite
DFT
EBSD
EDS

ABSTRACT

In this study, a two-step optimisation process for the estimation of the single crystal stiffness tensor from the indentation modulus is presented. This was accomplished by using a 2-dimensional data correlation method for nano-indentation, EBSD and ab initio data, as well as EDS for phase separation in a multi-phase material. Here, a single-phase Fe-24Ni-0.4C austenitic steel and a two-phase Fe-9.5Ni-0.5Co Seymchan meteorite were used as example materials.

In a first step, the combination of high-speed nano-indentation mapping data with elemental and orientation distribution maps allowed the estimation of indentation moduli along specific crystal surface planes normal directions, (001), (011) and (111) using a least squares optimisation based on starting values from DFT or experimentally determined stiffness tensors. A second global optimisation step to estimate the single crystal stiffness tensor using pre-solved solution parameters of the Vlassak-Nix equations yielded reasonable correspondence between the experimentally determined stiffness tensors from correlative nano-indentation data and other methods. The presented method demonstrates generally the possibility to derive directionally sensitive elastic properties from high-speed nano-indentation for cubic materials statistically.

1. Introduction

The development of new materials, whether for structural or functional applications, increasingly focuses on smaller scales and includes the representation of all individual components making up advanced, multi-phase microstructures. For this, many conventional methods of material characterisation have been extended to provide data at small scales and efforts to achieve characterisation across large areas while combining different types of information [1,2]. For example, research methods such as orientation imaging and chemical analysis inside the scanning electron microscope (SEM), first-principle and atomistic simulations as well as nano-indentation have provided new insights and enable multi-scale approaches to measure, predict and interrelate local properties [3–7].

The nano-indentation technique has become particularly effective in evaluating the mechanical properties of materials in combination with a variety of other methods, such as finite element simulations [8,9] or first-principle calculations [10] to correlate plastic and elastic properties or energy dispersive spectroscopy (EDS) to achieve phase mapping [11,12]. Efforts were also made to correlate not only with a single technique, but with two or more methods. Using the example of a $Mn_{15}Si_{26}$ compound, combined nano-indentation, electron backscatter diffraction (EBSD) and elastic moduli calculated from first principles were used to analyse the elastic properties across several grains [13]. Furthermore, correlative nano-indentations were conducted to elucidate the orientation-dependent elastic modulus in conjunction with EBSD analysis. Commercially pure titanium was indented with different indenter geometries to obtain the reduced modulus represented in an inverse pole figure (IPF) [14]. Similarly, EBSD and nano-indentation measurements for lithium metal have been correlated and also used to extract directional variations of the indentation modulus visualised by plotting in an IPF [15].

Although high-speed nano-indentation (NIT) is steadily gaining popularity, correlative research using NIT is still limited due to a lack of

* Corresponding author.
E-mail address: seehaus@imm.rwth-aachen.de (M. Seehaus).
[1] These authors contributed equally to this work.

https://doi.org/10.1016/j.matdes.2023.112296
Received 30 June 2023; Received in revised form 30 August 2023; Accepted 30 August 2023
Available online 9 September 2023

easily accessible tools and the challenges in error-correction. Especially the correction of spatial sampling errors can be a tedious process for data from independent measurements for correlative analysis, as distortions in property maps, EBSD and a NIT grid, are considered independently. Even though the measurement of the EBSD data itself is convenient, the associated distortions caused by thermal drift, electromagnetic field and sample tilt often lead to spatial discrepancies between NIT- and EBSD-results [16]. In a previous study, the XPCorrelate library was developed based on the MATLAB® environment to solve some of these correlation and correction issues [17].

Once spatial correlation is achieved, the next objectives often involve making predictions or comparisons of the identified correlations with theory.

The main objective of this study is therefore to develop a versatile and extendable open-source Python-based point-to-point correlation library for orientation/phase analysis from EBSD/EDS with nano-indentation data. Ultimately, the goal is to enable the estimation of a directional indentation modulus for specific crystal orientations and the single-crystal stiffness tensor from further analysis.

Therefore, the analysis will expand beyond the visualisation of directional elastic properties in IPFs to quantitative estimates of directional and single crystal elastic properties. Nano-indentation is very well suited to acquire the sub-grain mechanical data required for this. However, it is limited in resolving orientation-dependent properties, as the three-dimensional stress field includes contributions from many crystallographic directions. On the other hand, the stiffness tensor is perhaps the mechanical property with the largest theoretical data available or most straightforwardly obtainable from ab initio predictions. Therefore, the main focus is not only to achieve spatial correlation but also use the correlative orientation and indentation modulus data to extract the experimental stiffness tensor from large high-speed NIT data sets and compare it with first principles calculations.

There have been several attempts to estimate the stiffness tensor of a single crystal based on indentation tests [13,15,18]. Most of these approaches are based on the Vlassak-Nix model [19] (V-N), but a major disadvantage of the complex V-N model is that the evaluation of the equation is computationally intensive. One way to overcome this complex evaluation of the constituting equations of the V-N model is using a pre-compiled solution for cubic materials. In this case, the precise evaluation of the indentation modulus for specific low-index planes is required, which is not always convenient.

In order to work around this limitation, a two-step optimisation process is proposed in this study. In the first optimisation step, the indentation stiffness tensor is constructed to determine the indentation moduli along specific (0 0 1), (0 1 1), and (1 1 1) planes normal directions and in a second optimisation step, the elastic constants C_{11}, C_{12} and C_{44} are predicted by applying sets of correction factors proposed by Vlassak and Nix [19].

The developed library presented in this paper enables a self-documenting correlation procedure between experimental and simulative methods, e.g., EBSD, high-speed NIT, SEM, optical microscopy, first-principle calculations and other scientific techniques, using a single phase Fe-24Ni-0.4C austenitic steel and a two-phase Fe-9.5Ni-0.5Co Seymchan meteorite as example materials. The latter was chosen as an intentionally challenging material for the alignments and it contains microstructural features on length scales of the order of interaction volumes of the measurement methods used.

2. Experimental procedure

Two different types of specimens were investigated in this study, an austenitic FeNiC (Fe-24Ni-0.4C) steel and a Seymchan meteorite (Fe-9.5Ni-0.5Co). The FeNiC steel represents a single-phase material, whereas the meteorite specimen was selected to represent a dual-phase material to demonstrate various correlation limitations.

The FeNiC steel and the meteorite samples were extracted with a size of about 1x1x0.5 cm^3, respectively, by electrical discharge machining or with a diamond saw. A metallographic preparation was then carried out to ensure an appropriately flat and deformation-free surface suitable for both, combined EBSD-EDS and nano-indentation experiments. Initially, the samples were mechanically ground and then polished using a water-based diamond suspension to a final 1 μm particle size. In order to minimise the surface relief which can affect the nano-indentation experiments, a short mechanical polishing was performed with 0.25 μm colloidal silica (OP-S, Struers, Denmark) on a neoprene polishing cloth (OP-Chem, Struers).

Microstructural analyses were performed by means of SEM, back-scattered electron (BSE) imaging and combined EBSD-EDS mapping in a dual-beam focused ion beam (FIB)-SEM Helios Nanolab 600i (FEI) (Hikari, EDAX Inc.) and a Hitachi SU-5000 in ETHZ ScopeM (Oxford UltimMax 100 EDS) at 20 kV. They were recorded with a step size of 1.3 μm across an area of 702x525 μm^2 for the steel and 1 μm step size across an 1280 × 769 μm^2 area for the Seymchan meteorite and were analysed using the EDAX OIM 7.3.1 software as well as the free MTEX 5.7.0 toolbox based on MATLAB® [20]. The EDS-mapping results were later quantified by the EDAX TEAM software using the e-ZAF method with binning option. The compositions of the austenitic FeNiC steel and the Seymchan meteorite based on preliminary studies and EDS investigations are shown in Table 1.

Nano-indentation experiments were performed on a FT-I04 Femto-Indenter (FemtoTools AG, Switzerland) equipped with an FT-S20,000 sensor and a diamond Berkovich tip. The indentation tests were performed in native displacement control to ensure a uniform maximum indentation depth for all indents. This also helps to control the inter-indent spacing to prevent strain field interactions and minimise the variations in elastic recovery between indents. The elastic portion of the recovery is determined through fast oscillation (150 Hz) of the indenter tip with a proportionally scaled oscillation amplitude. This continuous stiffness measurement (CSM) allows a stiffness measurement as a function of depth. For the two samples, the indentation depth and spacing were scaled relative to the microstructure of the samples. For the Seymchan meteorite fragment, a map of 384 by 216 indentations was performed with a maximum depth of 190 nm and a 2 μm spacing. For the austenitic FeNiC sample, a map of 250 by 200 indentations was carried out with a maximum depth of 95 nm and a 1 μm spacing. Representative values for each indentation were determined from the mean of values measured at contact depths above 50% of the target depth for elastic modulus and 80% for hardness to minimize errors from indentation size effects. By taking representative values at these relatively larger depths, influences from initial intermittent flow and indenter tip imperfection (observed at contact depths < 25 nm in this case) are avoided.

By NIT, the reduced modulus E_r is obtained and used to calculate the indentation modulus of the specimen E_{NI} considering the Poisson's ratio ν_S of the sample (Eq. (1)).

$$\frac{1}{E_r} = \frac{1-\nu_0{}^2}{E_0} + \frac{1-\nu_{S,isotropic}{}^2}{E_{NI}} \tag{1}$$

Eq. (1) is derived from the unloading stiffness in elastic deformation by a flat cylindrical punch of elastic materials [23,24], with the Young's modulus and Poisson's ratio for the diamond indenter, taken as E_0 =

Table 1
Reported and measured compositions in [wt.-%] of the austenitic steel and the Seymchan meteorite by means of EDS.

Specimen	Fe	Ni	Co	C	
FeNiC	Bal.	22.74		0.93 ± 0.2 [21]	Present study
Seymchan meteorite	Bal.	11.41 ± 0.24	0.48 ± 0.06		Present study
Seymchan meteorite	Bal.	9.5	0.5		[22]

1140 GPa and $\nu_0 = 0.07$, respectively.

The such measured indentation modulus is a weighted average of the material's single crystal elastic constants, where the weights depend on the crystal orientation, and are not necessarily the same for every indenter shape [19]. Later, it was shown that small deviations from a general axisymmetric indenter shape do not affect the obtained values of the indentation modulus, so that it is also applicable to Berkovich indenters [25] and elastic–plastic contact [26].

2.1. Point-to-point correlation

To achieve point-to-point correlations between nano-indentation, EBSD and EDS measurements, a dedicated Python library 'PyXC' was developed [57]. The library 'PyXC' corrects systematic distortions that occur with various measurement methods, aligns the data layers to a reference image and queries the data by an arbitrary x-/y-coordinate. In Fig. 1 the data query and the associated correlation procedure is depicted schematically.

Due to the flexibility of the library, almost any 2-dimensionally sampled data with or without x/y-coordinates can be correlated. However, to achieve the correlation without x/y-coordinate information (e.g. an image from an optical microscope or a scanning electron microscope) an assignment of missing x/y-coordinates based on respective pixel indices is required. Any data with x/y-coordinates can directly be loaded into the library.

In order to perform a point-to-point correlation, each layer must be accurately aligned. In general, this operation is difficult to automate since the representation of the data differs considerably between the various measurements, such that manual alignment is unavoidable. In some cases, the distortion of the collected data is of such complexity that the correction procedure cannot be achieved with simple translation and rotation operations due to the spatial distortion as demonstrated in Fig. 2. To deal with these distortions, either an affine transformation or homography is required. The transformation matrices for the 2-dimensional affine transformation and homography are given in Eq. (2) and Eq. (3), respectively [27].

$$\begin{bmatrix} x' \\ y' \\ 1 \end{bmatrix} = \begin{bmatrix} m_{11} & m_{12} & x_t \\ m_{21} & m_{22} & y_t \\ 0 & 0 & 1 \end{bmatrix} \begin{bmatrix} x \\ y \\ 1 \end{bmatrix} \tag{2}$$

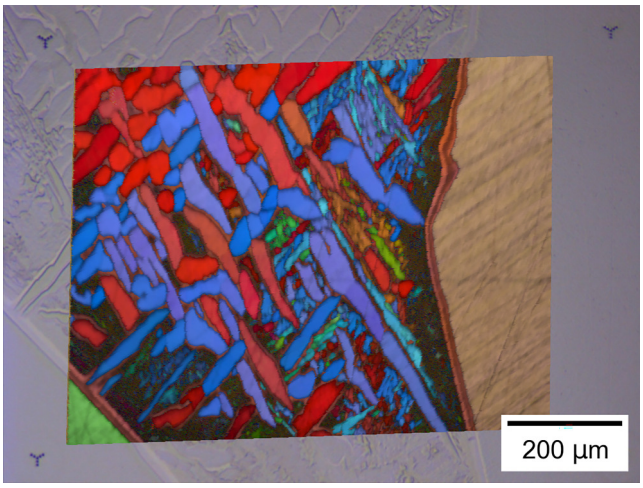

Fig. 2. Example of a spatially distorted EBSD map of the Seymchan meteorite calibrated using the 2-dimensional homography and aligned on top of an optical microscope image.

$$\begin{bmatrix} x' \\ y' \\ 1 \end{bmatrix} = \begin{bmatrix} h_{11} & h_{12} & h_{13} \\ h_{21} & h_{22} & h_{23} \\ h_{31} & h_{32} & 1 \end{bmatrix} \begin{bmatrix} x \\ y \\ 1 \end{bmatrix} \tag{3}$$

Here, x/y are an original point coordinate and x'/y' represent a new point coordinate after the transformation. The matrix components m_{ij} and h_{ij} denote the elements of the respective transformation matrix.

The correlation process is based on the evaluation of the Euclidean distance pairs. A schematic diagram that illustrates the point-to-point correlation process is given in Fig. 3. First, the distance between an arbitrary point x/y (e.g. from the nano-indentation layer) and all coordinates in the target layer (e.g. EBSD) is evaluated. Then, a calculated set of distance pairs is filtered out by a cut-off radius as well as the maximum nearest neighbour number. Values that are outside a certain cut-off radius around the query centre point (x,y) are not included in the correlation which reduces the computational costs to determine the Euclidean distance pair. Optionally, any statistical analysis (e. g. mean, standard deviation) can be performed for the experimental data points

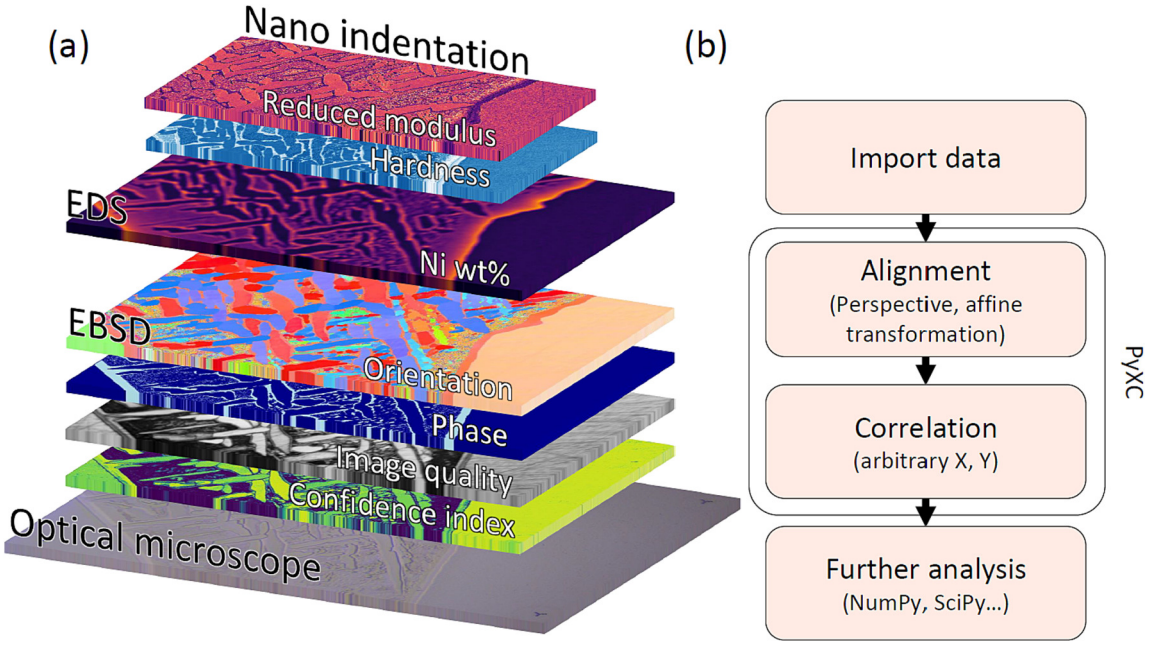

Fig. 1. (a) Schematic representation of the data query process on the example of the Seymchan meteorite data and (b) the methodological correlation procedure.

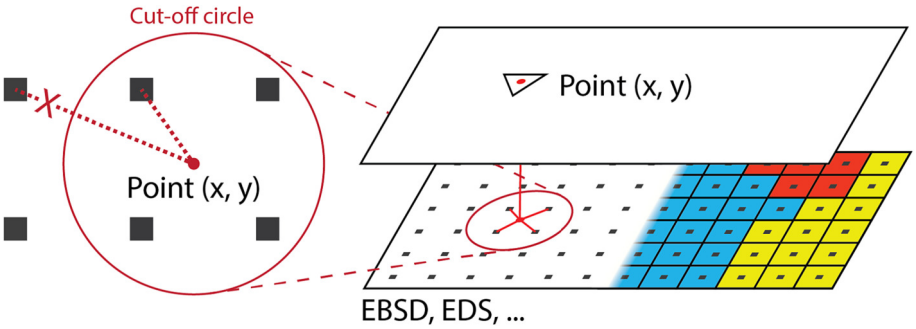

Fig. 3. Schematic diagram illustrating the point-to-point correlation process. Data points from the data layer can be obtained based on the Euclidean distance between the desired point locations.

that fulfil the cut-off condition (e.g. the 4 data points inside the red cut-off circle in Fig. 3). This correlation procedure is not only limited to nano-indentation and EBSD analysis, but also applicable for any 2-dimensionally sampled data.

Reading of the required scientific data such as EBSD, EDS, and nano-indentation was performed by a custom-developed in-house library and the IPF colouring was achieved by using the orix library [28]. Further analysis after the correlation step was realised with SciPy (least-squares and differential evolution minimisation) and the Scikit-learn (DBSCAN clustering) libraries, respectively [29,30].

2.2. Correlation with experimentally or DFT-based elastic moduli

A two-step procedure for predicting the single crystal stiffness tensor by correlated high-speed NIT, EBSD and EDS data is proposed. This approach begins with DFT-based (here using pure iron [31] to demonstrate the practicability, even if simplified initial data are used) interpolation of the optimised indentation moduli along (0 0 1), (0 1 1) and (1 1 1) planes normal directions. These indentation moduli are then applied in a second step to the mathematical relationship described by Vlassak and Nix to estimate the correct C_{11}, C_{12} and C_{44} values. A schematic representation of this procedure is shown in Fig. 4.

The estimation of the orientation-dependent indentation moduli begins with a point-to-point correlation of the EBSD, EDS and nano-indentation data, which relates crystallographic orientation to mechanical properties, resulting in sets of Euler angles, composition and indentation moduli. Here, the elastic modulus can be calculated in two ways. On the one hand, the nano-indentation based indentation modulus $E_{NI}(E_r, \nu)$ can be derived from E_r using Eq. (1) with the condition of $\nu = 0$ (according to V-N). On the other hand, the orientation-dependent elastic modulus $E_{OD}(C_{11}, C_{12}, C_{44}, \phi_1, \Phi, \phi_2)$ for the investigated cubic material can be calculated from the Euler angles (ϕ_1,Φ,ϕ_2)

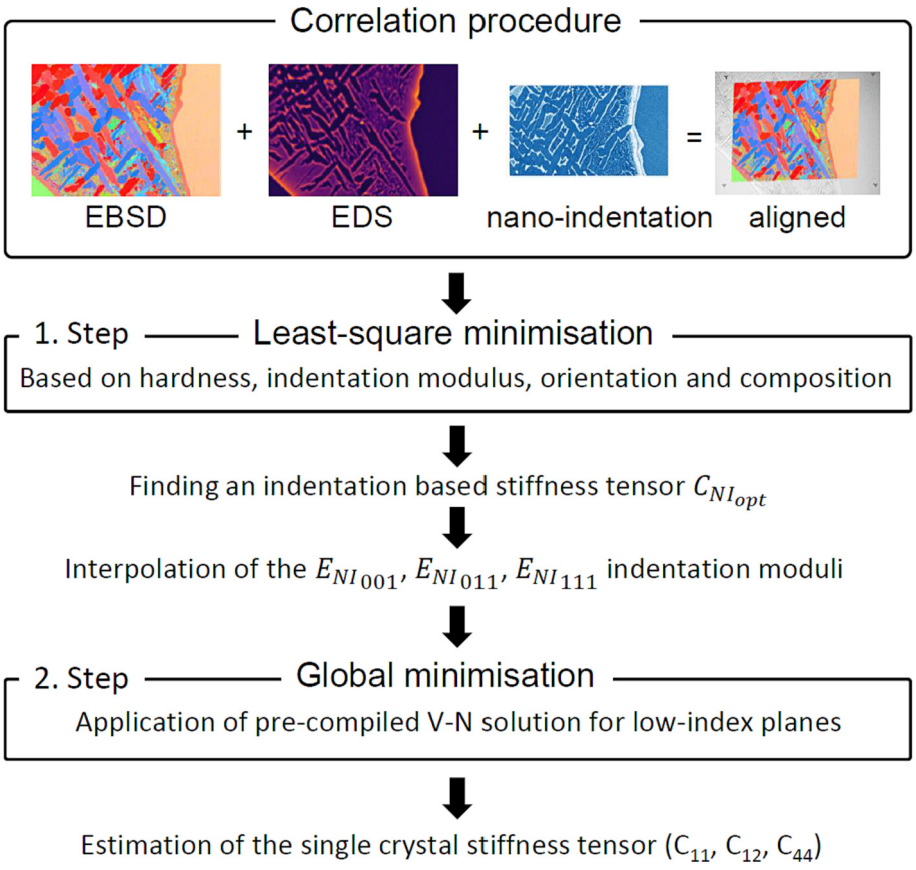

Fig. 4. Concept of the two-step estimation scheme.

and the stiffness tensor C in Voigt notation (in cubic crystal systems dependent on the elastic constants C_{11}, C_{12}, C_{44}) with Eq. (4).

$$\frac{1}{E_{OD}} = S_{11} - 2\left(S_{11} - S_{12} - \frac{S_{44}}{2}\right)\bullet\left(l_1^2 l_2^2 + l_2^2 l_3^2 + l_1^2 l_3^2\right) \tag{4}$$

S_{ij} denote the independent entries of the elastic compliance matrix obtained from the stiffness tensor, while l_1, l_2 and l_3 represent the direction cosines for an arbitrary crystallographic direction l which can be calculated from the rotation matrix R_{ZXZ} (according to Bunge) that is described in Eq. (5).

$$R_{ZXZ} = R_Z(\theta) \bullet R_X(\theta) \bullet R_Z(\theta) \text{ with } R_Z(\theta) = \begin{bmatrix} cos\theta & -sin\theta & 0 \\ sin\theta & cos\theta & 0 \\ 0 & 0 & 1 \end{bmatrix} \text{ and } R_X(\theta) = \begin{bmatrix} 1 & 0 & 0 \\ 0 & cos(\theta) & -sin(\theta) \\ 0 & sin(\theta) & cos(\theta) \end{bmatrix} \tag{5}$$

With the given E_{OD} and E_{NI} values, it is possible to perform a least-squares optimisation to find out the best C_{11}, C_{12}, and C_{44} values which describe the optimised indentation-based stiffness tensor $C_{NI_{opt}}$. For this purpose, the least-squares optimiser minimises the cost function given in Eq. (6). The cost function F equals the sum of absolute differences between E_{OD} and E_{NI}.

$$F = \sum_i |E_{OD,i} - E_{NI,i}| \tag{6}$$

However, since there are several local minima, a proper initial guess is crucial to ensure a reliable solution. The initial values for the elastic constants C_{11}, C_{12}, and C_{44} can be set by either available experimental ($C_{exp_{initial}}$) or DFT-based ($C_{DFT\,initial}$) data. In this study data for pure iron from DFT was used [31].

Before, it was necessary to accurately determine the indentation moduli along the (001), (011), (111) planes normal directions experimentally for this solution, which is not always possible, particularly if the exact crystal orientations are not contained in a polycrystalline sample of interest. However, based on the proposed approach, the indentation moduli along the (001), (011), and (111) planes normal directions, respectively $E_{NI(001)}$, $E_{NI(011)}$, and $E_{NI(111)}$, were interpolated from the optimised $C_{NI_{opt}}$. Subsequently, these specific indentation moduli could be applied to the V-N solution for cubic materials (Eq. (7) [19]), eliminating the need for indentation tests in these specific low-index planes.

$$E_{NI\,(hkl)} = \beta_{(hkl)}\left(\frac{E}{1-\nu_{VRH}^2}\right)_{isotropic} \tag{7}$$

The correction factor β is given by Eq. (8) [19].

$$\beta = a + c(A - A_0)^B = a + c\left(\frac{2C_{44}}{C_{11} - C_{12}} - A_0\right)^B \tag{8}$$

The terms a, c, A_0 and B denote fitting parameters which are valid for a fixed Poisson's ratio $\nu_{<001>}$ in the $\langle 001 \rangle$ direction (Eq. (9)) given in the V-N model [19] and the term A reflects the Zener ratio (often referred to as anisotropy factor) according to Eq. (10) [32].

$$\nu_{<001>} = -\frac{S_{12}}{S_{11}} \tag{9}$$

$$\mathrm{A} = \frac{2C_{44}}{C_{11} - C_{12}} \tag{10}$$

The elastic modulus can be calculated from the stiffness tensor C_{ij} and its compliance tensor S_{ij} using the Voigt-Reuss-Hill (VRH) average [33], where the respective Voigt [34] and Reuss [35] arithmetic averages of the bulk and shear moduli are taken into account. The VRH-average of the elastic modulus is given by Eq. (11).

$$E_{VRH} = \frac{9K_{VRH}G_{VRH}}{3K_{VRH} + G_{VRH}} = \frac{\overbrace{3(c_{11}+2c_{12})}^{9K_{VRH}}\overbrace{\left(\frac{3\,c_{11}^2 - 6\,c_{11}c_{12} + 3\,c_{12}^2 + 38\,(c_{11}-c_{12})c_{44} + 12\,c_{44}^2}{10\,(3\,c_{11} - 3\,c_{12} + 4\,c_{44})}\right)}^{G_{VRH}}}{\underbrace{(c_{11}+2c_{12})}_{3K_{VRH}} + \underbrace{\left(\frac{3\,c_{11}^2 - 6\,c_{11}c_{12} + 3\,c_{12}^2 + 38\,(c_{11}-c_{12})c_{44} + 12\,c_{44}^2}{10\,(3\,c_{11} - 3\,c_{12} + 4\,c_{44})}\right)}_{G_{VRH}}} \tag{11}$$

From isotropic elasticity theory, the Poisson's ratio of a given crystal can be calculated from the respective averaged shear and bulk moduli according to Eq. (12).

$$\nu_{VRH} = \frac{3K_{VRH} - 2G_{VRH}}{2(3K_{VRH} + G_{VRH})} = \frac{\overbrace{c_{11}+2\,c_{12}}^{3K_{VRH}} - \frac{\overbrace{3\,c_{11}^2 - 6\,c_{11}c_{12} + 3\,c_{12}^2 + 38\,(c_{11}-c_{12})c_{44} + 12\,c_{44}^2}^{2G_{VRH}}}{5(3\,c_{11} - 3\,c_{12} + 4\,c_{44})}}{\underbrace{2\,c_{11}+4\,c_{12}}_{6K_{VRH}} + \underbrace{\frac{3\,c_{11}^2 - 6\,c_{11}c_{12} + 3\,c_{12}^2 + 38\,(c_{11}-c_{12})c_{44} + 12\,c_{44}^2}{5(3\,c_{11} - 3\,c_{12} + 4\,c_{44})}}_{2G_{VRH}}} \tag{12}$$

In order to estimate the single crystal stiffness tensor, a global minimisation [30] was performed based on Eq. (13) as well as Eq. (14) and the relating cost function Eq. (15).

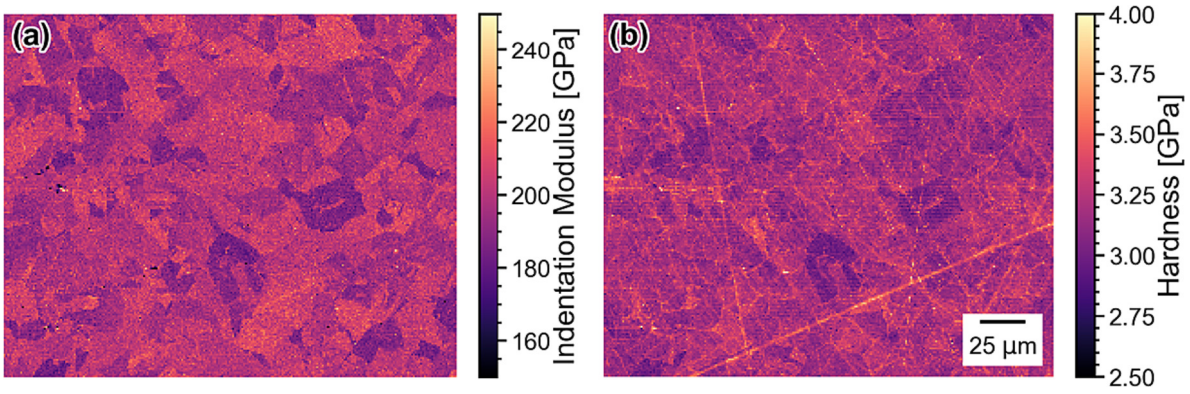

Fig. 5. (a) Indentation modulus map and (b) hardness map of the austenitic FeNiC steel. The lines indicate locally work-hardened sub-surface deformation zones caused by initial scratches resulting from metallographic preparation.

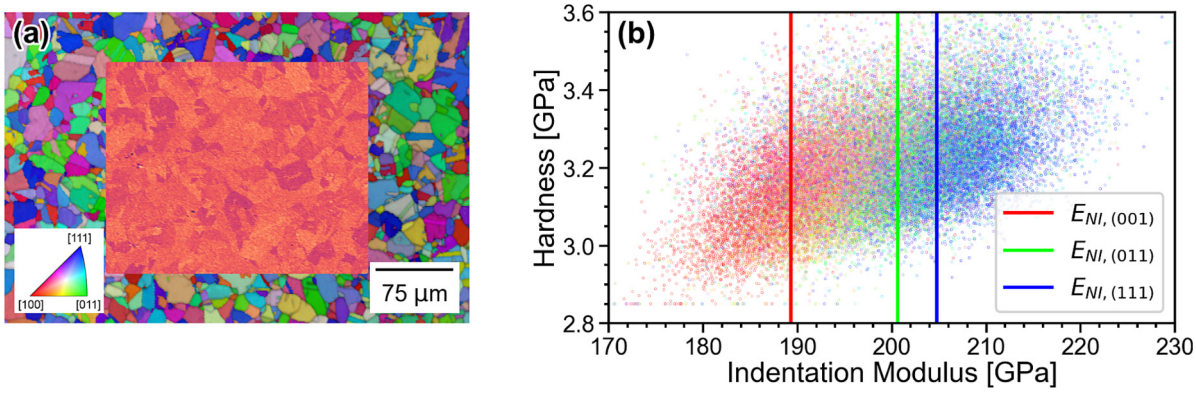

Fig. 6. (a) EBSD with the indentation mapped area indicated and (b) orientation-dependent hardness vs. indentation modulus plot of the austenitic FeNiC steel sample coloured with respect to crystal orientation and predicted indentation moduli along the (001), (011) and (111) planes normal directions.

$$F_{(hkl)}(C_{11}, C_{12}, C_{44}) = \beta_{(hkl)} \left(\frac{E_{VRH}}{1 - \nu_{VRH}^2} \right)_{isotropic} - \overbrace{E_{NI(hkl)}}^{from\ 1.\ Step} \quad for\ hkl = 001,\ 011\ and\ 111 \tag{13}$$

$$F_\nu = \nu_{<001>_{proposed}} - \nu_{<001>} \tag{14}$$

$$F_c = |F_{(001)}| + |F_{(011)}| + |F_{(111)}| + |F_\nu| \tag{15}$$

Using this approach with these preconditions and solely being dependent on the elastic constants C_{11}, C_{12} and C_{44}, a global minimum could be estimated and predict the stiffness tensor taking into account the pre-compiled fitting parameter sets for a proposed Poisson's ratio in ⟨001⟩ direction $\nu_{<001>_{proposed}}$(FeNiC = 0.35 / Seymchan meteorite = 0.3) based on the V-N method.

3. Results

3.1. Single phase material - FeNiC steel

3.1.1. Alignment between EBSD/nano-indentation data and first assessment of the single crystal stiffness tensor by the two-step approach

The crystallographic orientation significantly affects the local elastic response. Correlative nano-indentation and EBSD measurements were applied to reveal the orientation-dependent elastic properties. High-speed NIT maps on the FeNiC steel are presented in Fig. 5 for the measured indentation modulus and hardness. These clearly display the underlying grain structure beneath the sample surface, which correlates well with the EBSD results, as shown in Fig. 6a). Some scatter can be observed in the indentation modulus map, which can be a function of either subsurface damage from imperfect surface preparation, remnant roughness [36] or local variations in dislocation density in cold-worked materials. The former is more likely in this case, as illustrated by the subsurface deformation zones or 'scratches' noticeable in the hardness map in Fig. 5b). Due to the larger size of the elastic strain field from which the indentation modulus is measured, relative to the plastic strain field measured by hardness, the effect of subsurface damage on the data is significantly less pronounced in the indentation modulus map than the hardness map.

E_{OD} was calculated assuming a samplés Poisson's ratio of 0, resulting in sets of correlated indentation modulus, hardness and orientation information. The orientation-dependent hardness and indentation modulus (E_{NI}) distribution of the indented area from Fig. 6a) as well as the predicted specific indentation moduli along the (001), (011) and (111) planes normal directions (Table 2) are presented in Fig. 6b).

As a first step, a least-squares optimisation technique (Sec 2.2) was applied to find the optimal C_{11}, C_{12} and C_{44} values that best predict the orientation-dependent indentation modulus. An initial stiffness tensor C was optimised, here taking into account $C_{DFT\,initial}$(Fe) of pure iron [31] and E_{NI} (Sec 2.2). By applying the resulting optimised $C_{NI_{opt}}$ entries, the directional indentation moduli at each data point were predicted using the related Euler angles with Eq. (4). The visualisation of the predicted, direction-dependent indentation modulus following the optimisation

Table 2
Least-squares fitted indentation moduli for the (001), (011) and (111) planes, respectively.

E_{NI001}	E_{NI011}	E_{NI111}
189.3 GPa	200.6 GPa	204.7 GPa

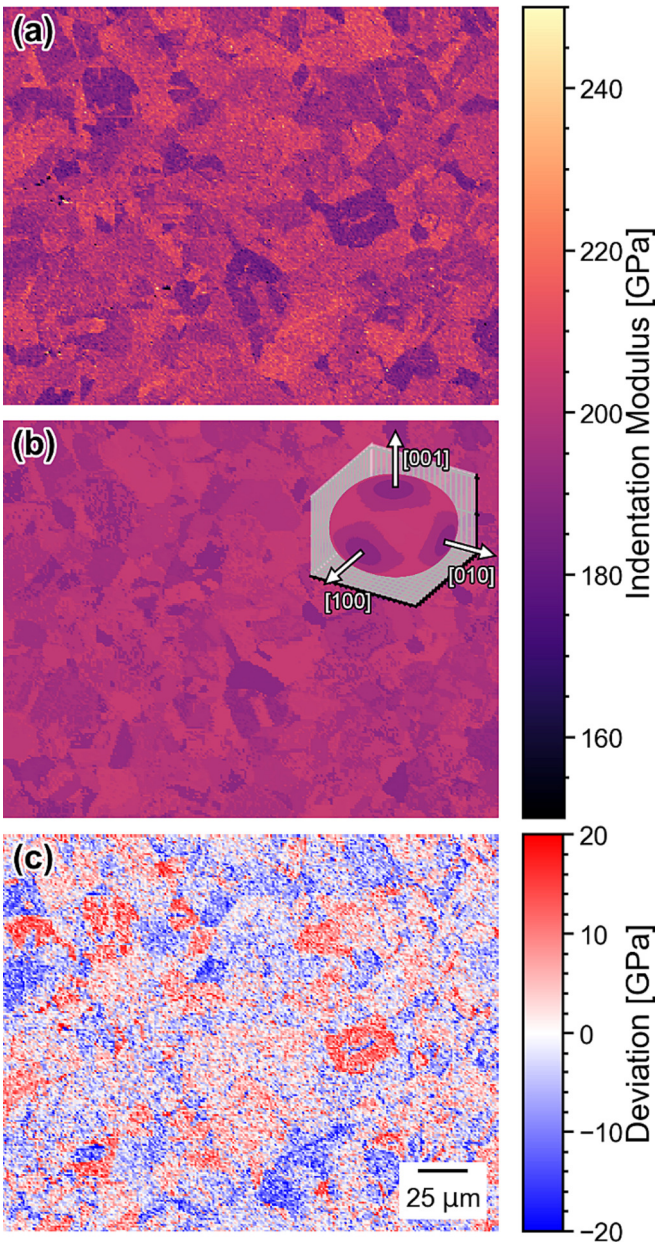

Fig. 7. First optimisation step using the austenitic FeNiC steel data showing (a) the experimentally obtained indentation modulus, (b) the predicted directional indentation moduli and the underlying spatial representation of $C_{NI_{opt}}$ visualised as inset in cartesian coordinates aligned with the [0 0 1] axes of the unit cell; (c) the differences between the predicted indentation modulus and the experimentally obtained indentation modulus.

procedure is illustrated in Fig. 7. In the first optimisation step the indentation modulus could be reproduced with good accuracy (average deviation = ±6 GPa), as shown in Fig. 7a) and Fig. 7b).

A second global minimisation step allowed further refinement of the obtained indentation modulus for low index planes in order to predict the single crystal stiffness tensor. For this purpose, the indentation moduli of the specific planes were determined on the basis of the first optimisation step using Eq. (7) and are presented in Table 2.

The values of the resulting indentation moduli and stiffness tensors $C_{NI_{opt}}$ and $C_{NI_{opt2}}$, respectively, are given in Table 3.

The tensor-based approach is particularly useful when the measurements ideally involve high-speed NIT, as it provides good statistics. However, it can also be useful in cases where there is no possibility to specifically measure different crystallographic planes or different sized data sets are to be correlated. As demonstrated using a subset of the steel sample in Fig. 8, the converged value of the $C_{NI_{subset}}$ exhibited similar values compared to the full dataset refinement if a good grain orientation distribution is ensured, as shown in Table 4.

3.2. Multi-phase material - Seymchan meteorite

3.2.1. Layer alignment for optical microscopy, EBSD, EDS and hardness data

The Seymchan meteorite sample was used in order to demonstrate the combined capabilities and limitations of the correlation procedure. In the present investigation, a plessite region that comprises a fine mixture of body-centered-cubic kamacite (referred to hereafter as α_m) and thin seams of taenite/ tetrataenite (referred to hereafter as γ_m) around the α_m grains was studied [27]. In addition, fine-grained intermediate domains of α_m and γ_m are visible. The mechanical properties within the plessite region were investigated using high-speed NIT and are also discussed in terms of the multimodal alignment of the correlated methods in Sec. 4.2. In Fig. 9 the indentation area of the analysed microstructure is shown using optical microscopy (Fig. 9a)) with aligned EBSD, EDS and hardness data given in Fig. 9b).

The mechanical properties of the corresponding region of the meteorite sample were plotted in the hardness-indentation modulus space (Fig. 10). The α_m and the γ_m clusters were visually determined by a correlation with EBSD/EDS phase information, which are indicated in Fig. 10a) and Fig. 10b) exhibiting the respective mechanical properties. In between these clusters, an intermediate zone is revealed and a clear orientation dependence can be observed for the α_m region. However, the orientation dependence of the other regions is not clearly visible. Furthermore, the cross-contamination between α_m and γ_m due to residual misalignment of the data should also be removed as far as possible (which will be discussed in detail in Sec. 4).

In order to facilitate the consecutive investigation of the orientation-dependent elastic response data on the meteorite sample, it is necessary to appropriately filter the correlated nano-indentation data based on the aligned microstructural information to isolate the α_m cluster.

The application of filtering techniques based on the confidence index, EBSD phase information, and DBSCAN clustering enable the exclusion of phases such as γ_m and the intermediate zone. Thereby, a further analysis solely on the α_m phase can be performed using the least-

Table 3
Initial and optimised DFT/indentation-based elastic constants as well as Zener ratio with varying Poisson's ratios and experimental data from the literature.

Ni	C	C_{11}	C_{12}	C_{44}	E_{VRH}	Zener ratio	ν_{VRH}	$\nu_{<001>}$	Reference
[wt%]		[GPa]							
0	0	266.63	122.63	104.5	229.7	1.45	0.28	0.32	Pure Fe [31] (Initial values from DFT)
24	0.4	246.3	99.2	80.6	198.4	1.10	0.28	0.29	1st optimisation ($C_{NI_{opt}}$ tensor)
24	0.4	199.8	107.5	87.7	174.7	1.90	0.29	0.35	2nd optimisation ($C_{NI_{opt2}}$ tensor)

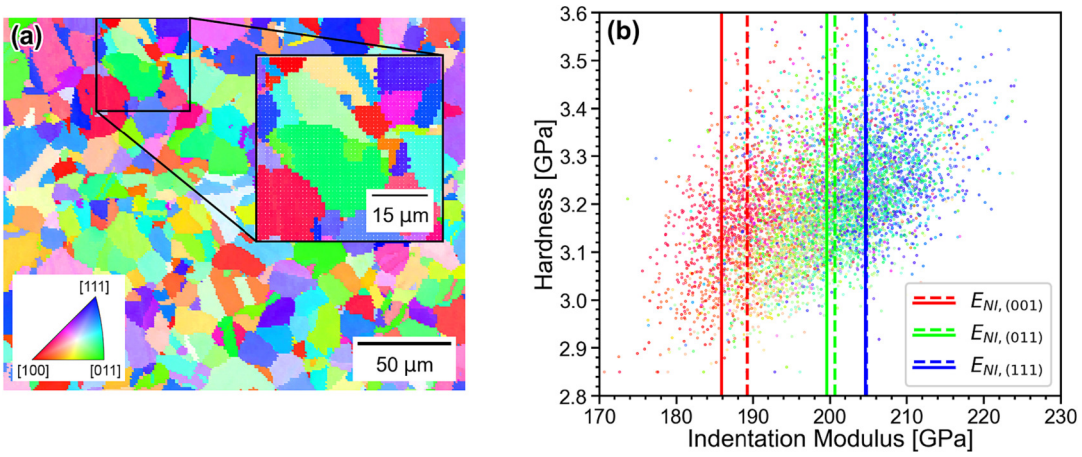

Fig. 8. (a) Location and (b) data distribution of a selected subset region of the austenitic steel data highlighting the predicted indentation moduli for the specific (0 0 1), (0 1 1) and (1 1 1) planes as vertical lines. The dashed lines represent the predicted indentation moduli of the entire map for comparison.

Table 4
Total (grain size filtered > 20) data set compared to a subset used for optimisation. The estimated single crystal stiffness tensor components exhibit similar values when the subset contains sufficient grains with orientations spanning the full orientation range.

Sample	No. of points	No. of grains	$C_{11\,opt^2}$	$C_{12\,opt^2}$	$C_{44\,opt^2}$
FeNiC (full)	49,800	approx. 400	199.8	107.5	87.7
FeNiC (subset)	2369	approx. 25	186.0	100.1	92.7

squares method described in Sec 2.2.

The consequence of the used filtering operations is illustrated in Fig. 11. In the present study, the contributions from the intermediate zone (depicted in Fig. 10a)) and the γ_m phase were removed by applying a sequence of filtering. This procedure is covered and discussed in more detail in Sec. 4.2.

Using this approach, it is possible to estimate the angular dependent indentation modulus E_{NI} by the optimised $C_{NI\,opt}$ based on a stiffness tensor $C_{DFT\,initial}(Fe)$ as shown in Fig. 12. The predicted E_{NI} (Fig. 12b)) was found to reproduce E_{NI} (Fig. 12a)) accurately.

4. Discussion

In this study, a method for the estimation of the orientation-dependent indentation modulus and the subsequent estimation of the single crystal stiffness tensor using correlative multi-modal investigations is described. For this purpose, measurement modalities including EBSD, EDS, nano-indentation and first-principle investigations were correlated in order to combine orientation, composition and indentation information using a newly developed Python library "PyXC". Based on a least squares minimisation, by using either initial experiment- or DFT-based stiffness tensors, the best fitting values for the orientation-dependent indentation modulus tensor $C_{NI_{opt}}$ could be estimated. Further, $C_{NI_{opt}}$ was used to obtain predictions of the indentation moduli along the (0 0 1), (0 1 1) and (1 1 1) planes normal directions in order to estimate the complete stiffness tensor of the single crystal from these indentation moduli determined on the basis of the V-N solution for cubic materials.

Previously, the evaluation of the constitutive equations could be performed using the V-N model to achieve accurate results for most indentation experiments. However, a solution of these constitutive equations from the V-N model is not available analytically. Consequently, computationally intensive numerical simulations are often required and their evaluation is difficult for many researchers using nano-indentation experiments.

The method proposed in this study enables an estimation of the single-crystal stiffness tensor without solving the V-N model by using pre-compiled solutions for cubic materials. Using the examples of a single phase austenitic FeNiC steel and a two-phase nickel-bearing Seymchan meteorite, the capabilities, limitations and methods for overcoming the deficiencies of the newly developed combinatorial analysis are demonstrated.

4.1. FeNiC steel

Qualitatively, the mechanical properties that are revealed by the indentation maps are consistent with earlier observations by Vlassak and Nix as well as other observations [11,19]. Here, the indentation modulus of the (1 0 0) plane is the lowest, while for the (1 1 1) plane it is the highest. Furthermore, the measured hardness values of the sample showed a different degree of variation over the varying orientations. However, most importantly, the indentation moduli were predicted reasonably from the indentation modulus tensor as shown in Table 2 and illustrated in Fig. 6b).

In the second optimisation step, the C_{11}, C_{12}, C_{44} values of the single crystal stiffness tensor were estimated by applying the pre-compiled solutions of the V-N model. The optimised $C_{NI_{opt^2}}$ entries resulting from the second optimisation is compared with other experimental results [37] in Fig. 13 revealing a good agreement.

Overall, the tensor-based two-step approach yielded good results and it is particularly useful when high-speed NIT is involved, as it provides good statistics for applying the least-squares optimisation.

4.2. Seymchan meteorite

In general, correlation is particularly difficult if there is insufficient statistical data or if it is performed on multi-phase materials. The difficulties are demonstrated here using a dual phase meteorite as an example. The correlation of the meteorite sample was challenging for the following reasons: (i) the contribution from regions of no interest must be properly filtered out to avoid cross-contamination, (ii) the relatively coarse grain size did not provide a good grain orientation distribution, (iii) the grain size difference and complex grain boundary regions between the α_m and γ_m made alignment difficult, (iv) the indentation spacing was similar-sized to the fine-scale features in the microstructure, (v) indentations placed on lateral or subsurface interfaces between phases yield mixed results. Hereinafter these limitations will be referred to as filtering, statistics or alignment problem, respectively.

The combination of nano-indentation and microscopy-based analysis provides the possibility of a complex filtering process to exclude any

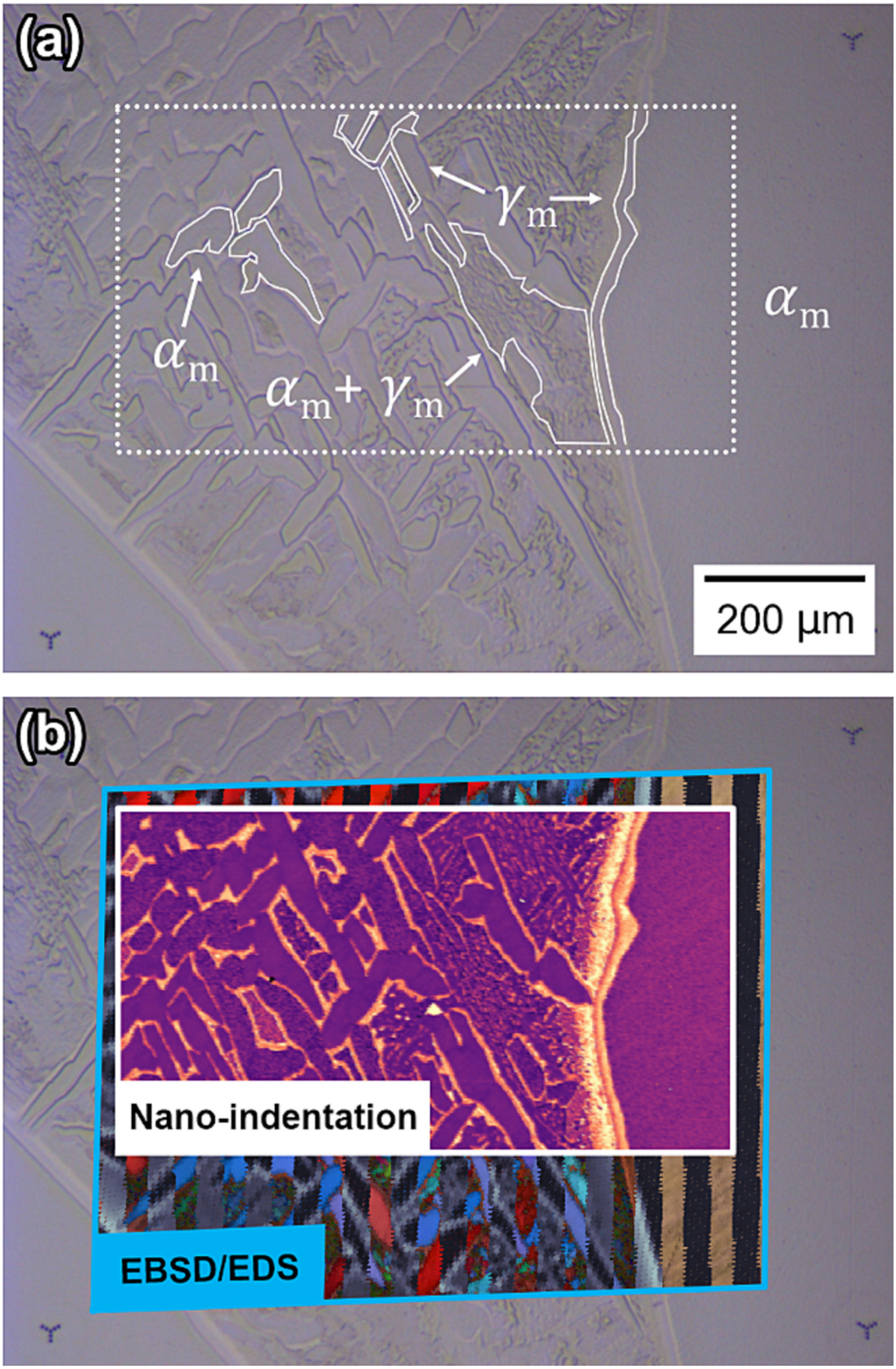

Fig. 9. (a) Optical microscopy of the region of interest in the plessite region of the Seymchan meteorite and (b) alignment result for the optical micrograph, EBSD, EDS and hardness data.

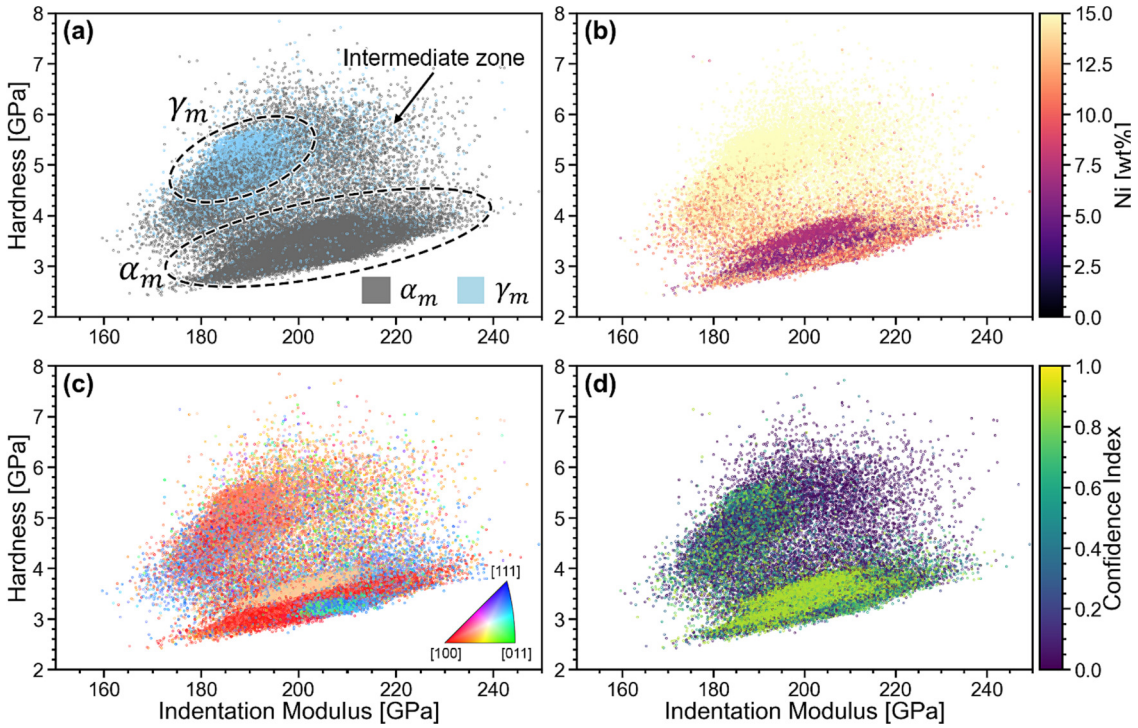

Fig. 10. Hardness vs. indentation modulus plots of the Seymchan meteorite sample showing (a) phase separation, (b) nickel content from aligned EDS data, (c) IPF coloring from aligned EBSD data (the green [0 1 1] orientations are intentionally plotted in the foreground for better visualization) and (d) confidence index values from aligned EBSD data.

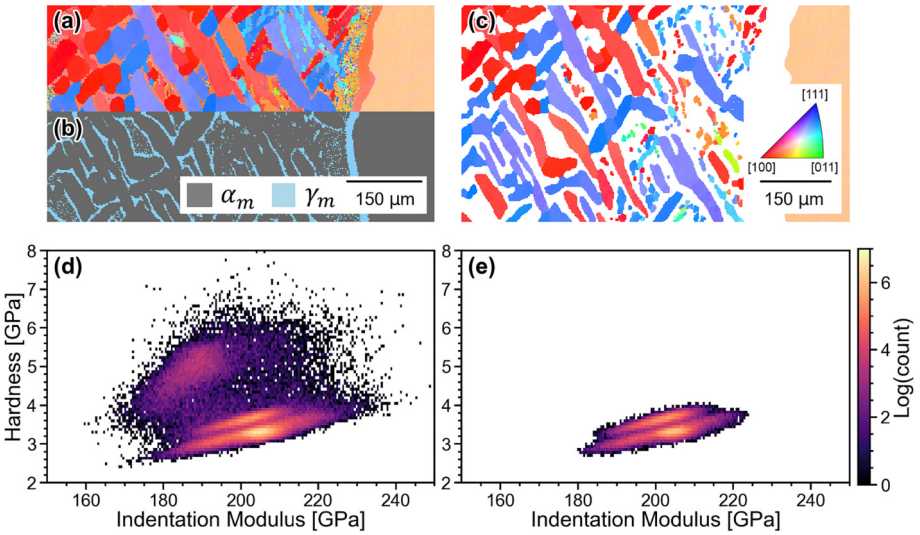

Fig. 11. Filtering procedure applied for the Seymchan meteorite to enable separate analysis of the α_m phase. EBSD data filled by nearest-neighbour approach (a) before combination with a (b) phase map and (c) after filtering. (d) Unfiltered and (e) filtered intensity plots for the Seymchan meteorite.

undesired phase, but it depends strongly on the material system and is therefore very individual. As the Seymchan meteorite consists of a complex microstructure, it requires appropriate filtering for further correlation. By combining several filtering conditions, the contribution from γ_m and the fine-grained mixture region were removed. First, the EBSD-based phase filter (phase = kamacite) was applied to extract the γ_m, but due to misalignment, covered later in this section, the γ_m could not be fully filtered out. Therefore, by applying a composition based (Ni wt% $<$ 10 wt%) and a confidence index filter (CI $>$ 0.5), almost all contributions from the γ_m phase were successfully removed. As a final processing step, a DBSCAN clustering with a minimum cluster size of 50 data points and a maximum distance of 0.08 between the data points was applied to eliminate data points with a large predefined distance to the cluster. This series of filtering operations as depicted in Fig. 14 was used to determine the mechanical responses of the correlated pure α_m phase.

4.2.1. Grain orientation statistics

A challenge resulting from a lack of grain orientation statistics is that a frequent occurrence of the specific crystallographic orientations can bias the least squares minimisation. For example, in Fig. 15, the predicted indentation moduli along the (0 0 1) and (1 1 1) planes normal

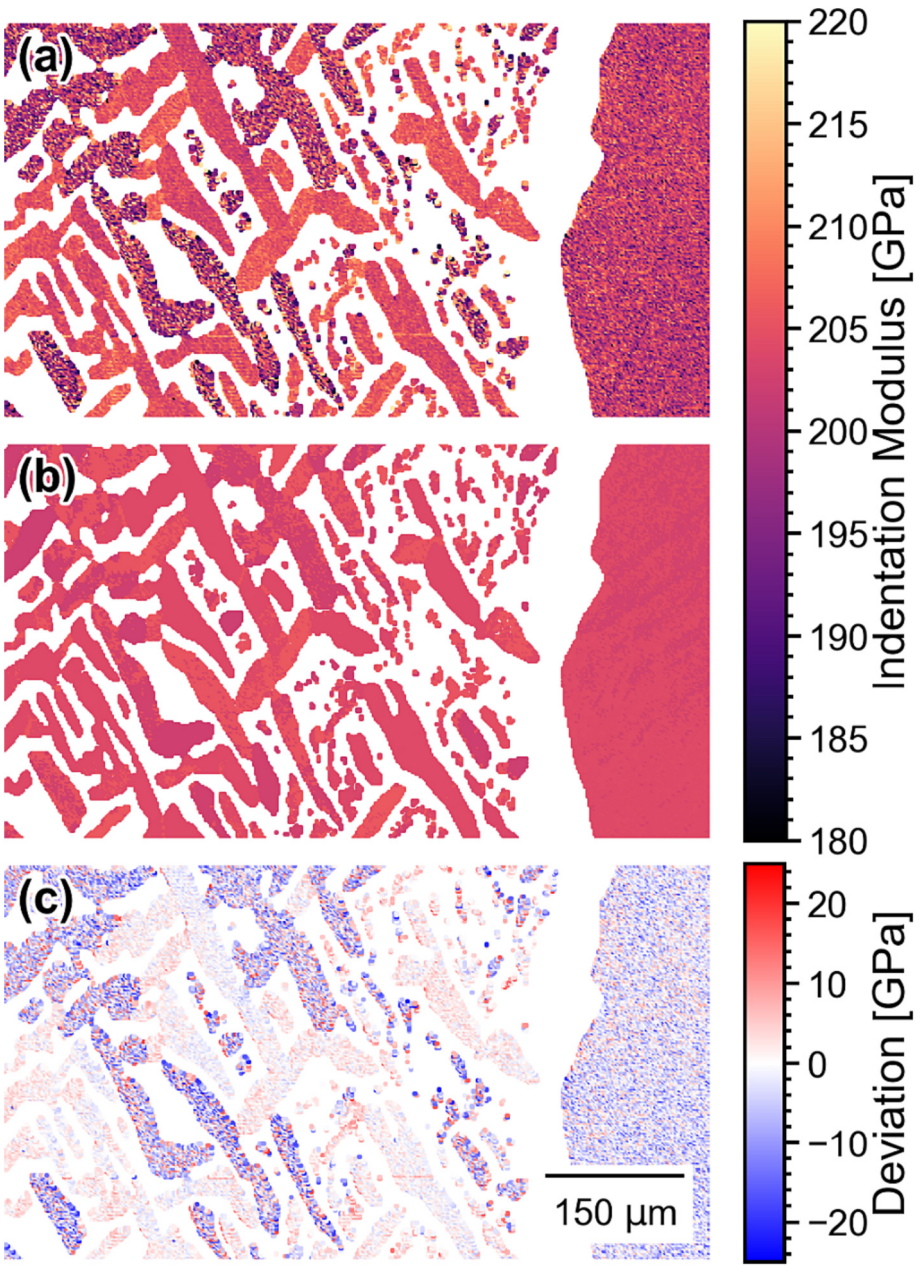

Fig. 12. (a) E_{NI} calculated from experimental E_r using a Poissońs ratio of$\nu = 0$, (b) predicted E_{NI} from $C_{NI\,opt}$ for the α_m phase of the Seymchan meteorite and (c) deviation between (a) and (b).

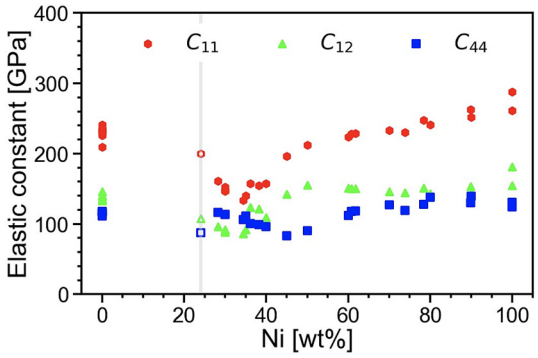

Fig. 13. Single crystal elastic constants from different pulse-echo-overlap measurements (Fe-Ni) [37–52] compared with the predicted values for the FeNiC derived from the two-step method presented in this study.

directions are well identified, as they are represented well by measurements on grains oriented accordingly, but the indentation modulus of the (011) plane could not be verified easily.

In this case for the Seymchan meteorite, the validation of the predicted indentation modulus of the (011) plane is not well achievable due to the relatively small number of orientations near the (011) plane, as shown in Fig. 11c). As a result, it is not possible to determine or confirm the indentation modulus of the (011) plane with certainty, which could be improved by a more homogeneous orientation distribution, e.g. by measuring across several areas or generally a larger area if the overall texture is not too strong. Most measurements were taken on grains with a surface plane near (001) and (111). Greater deviations from the predicted modulus are present in the near (001) orientations, as indicated by the purple colouring in Fig. 12c) as a result of a mix of larger deviations from the predicted value towards the red and blue ends of the colour scheme. This is related to the wider distribution around the average value in these grains visible in Fig. 15. It occurs with a

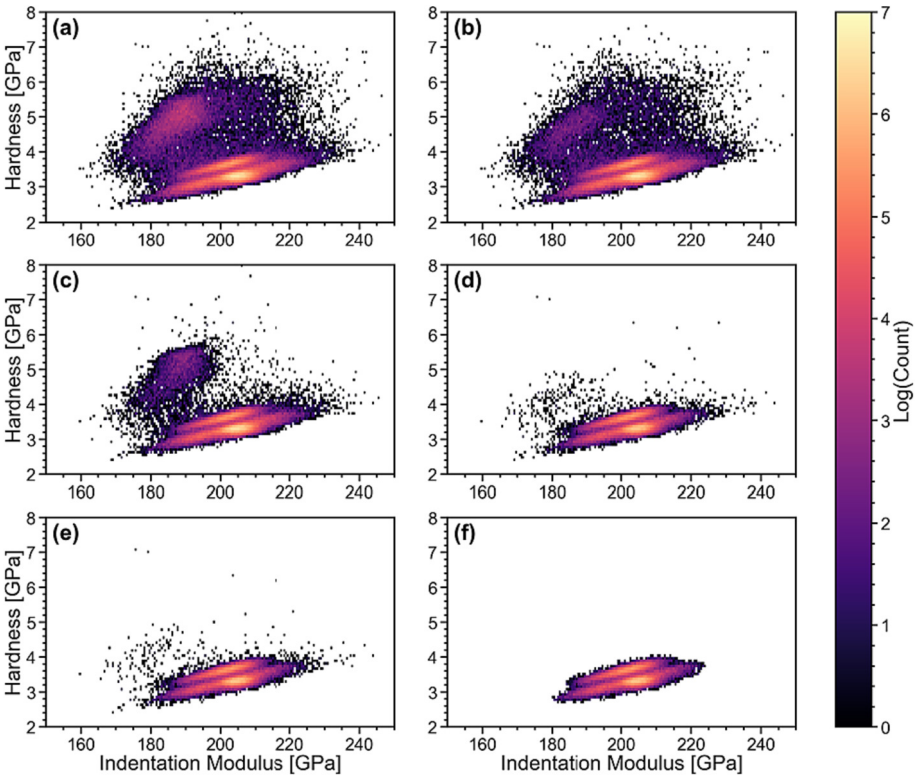

Fig. 14. (a) Raw data set without filtering and (b)-(f) sequential filtering steps to reveal respective filter effects. (b) Phase (here Kamacite), (c) CI (here > 0.5), (d) composition (here Ni < 10 wt%), (e) combined (here Phase + CI + composition) and (f) refined clustering (here DBSCAN) + combined filter methods.

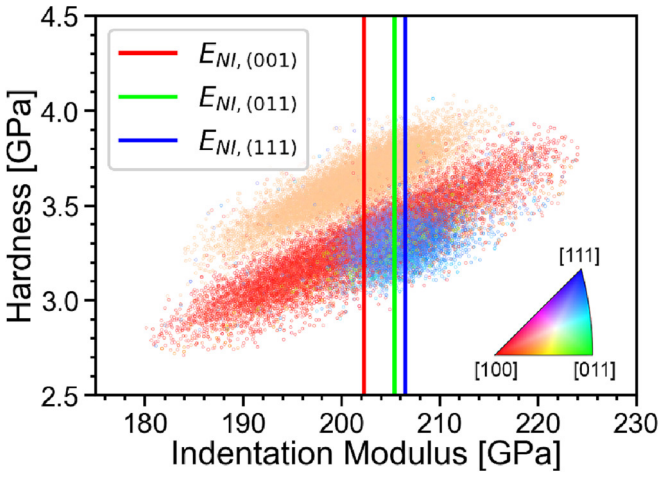

Fig. 15. Hardness vs. indentation modulus plot for the Seymchan meteorite, colourised according to the corresponding orientations (IPF colour code) and highlighted predicted indentation moduli for the three specific crystallographic planes (0 0 1), (0 1 1) and (1 1 1), respectively.

systematic relationship between hardness and modulus in the sense of a constant H/E and this phenomenon does not appear to be related to a local gradient in Ni concentration as shown in Fig. 10b). It is, however, correlated with a stronger variation in surface height as extracted from the contact height measurements during indentation. It is therefore assumed that the increased scatter of the modulus mapping at constant ratio H/E originates from an orientation dependent etching topography encountered in this meteorite phase during the last metallographic preparation steps. Clarification of the origin of the orientation dependent etching and its exact nano-scale morphology are beyond the scope of this work, but are in principle well documented in the literature for different materials [53] and also used for crystal orientation mapping [54].

4.2.2. Alignment and interpretation of data sets with small features

For the microstructure of the meteorite sample, the most difficult part is the alignment. In Fig. 10 it can be seen that the γ_m region does not only consist of γ_m points. It also contains a certain amount of α_m points. This is due to the challenges anticipated and indeed presented by this microstructure. The existence of two phases and small single phase regions makes alignment much more challenging than in a single phase polycrystal, as long as the grain size is significantly larger than the minimum indentation spacing. In addition, near the interphase boundary, even small misalignments can make the correlated data inaccurate. Furthermore, the orientation, chemical and mechanical analyses suffer from averaging effects related to their respective interaction volumes (visualised indirectly in terms of the EBSD confidence index (CI) in Fig. 10d)) as well as possible distortions in the signal due to surface topography originating from the metallographic preparation and mechanical contrast between the phases. For the thin γ_m phase, in contrast to the bulky α_m phase, the major part of the data is visibly contaminated by α_m due to the misalignment.

Although the two-dimensional correlation technique has proven to be quite serviceable, correlative nano-indentation is challenging under special circumstances. Several of these issues for single phase materials have already been discussed in detail by Magazzeni et al. for the XPCorrelate tool which provides similar capabilities within the MATLAB® environment [17]. The limitations were divided into two categories, alignment and interpolation, where the alignment limitation originated from misalignment of the different measurements, while the interpolation limitation resulted from interpolation between the datasets with different data characteristics.

The correlation between the different datasets requires consideration of the limitations of the respective measurement methods. For example, high-speed NIT can be less precise than classical nano-indentation due

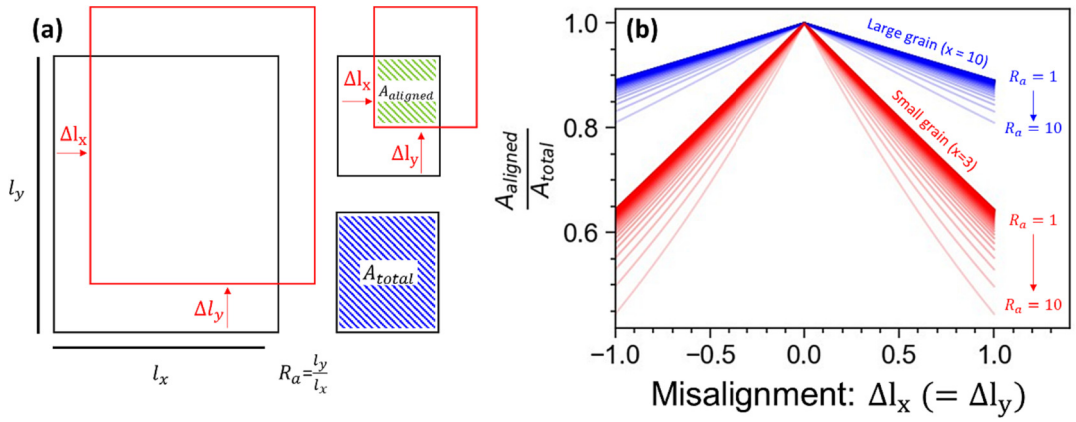

Fig. 16. (a) Assumed geometries with similar aspect ratio, but different sizes for (b) calculation results of the fraction of the correctly aligned area depending on the grain/area size.

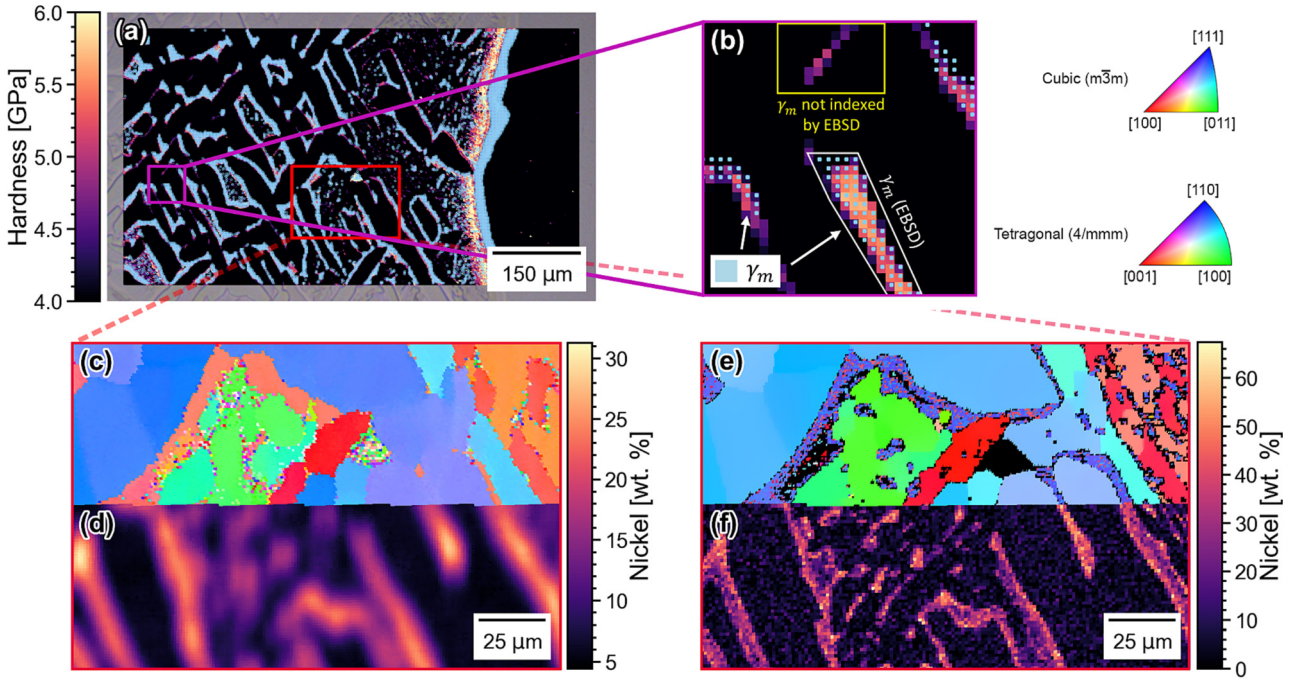

Fig. 17. (a) Hardness plot of the meteorite sample, superimposed with an indentation pattern coloured according to the γ_m phase; (b) indentation map overlayed with correlated EBSD spots revealing a thin γ_m band not indexed by the EBSD measurement highlighted in yellow. The region of this methodological limitation is depicted within the red rectangle. Spatial resolution discrepancy of (c) EBSD and (d) EDS with a detector area window of 60 mm^2. In comparison (e) EBSD (where γ_m is indexed as tetrataenite) with correlated (f) higher precision EDS detected with two large area window detectors of 100 mm^2 after indentation that allowed quantification without binning.

the general speed of the measurement, the sampling rate or due to the high strain rate and closer spacing between the indents [17,55,56]. Consequently, potential sources of error include alignment, interpolation and methodological limitations, whereby alignment could be critical for multi-phase materials if the grain size distribution of the given sample is multi-modal or the aspect ratio of the grains is high. The degree of misalignment was quantified to demonstrate the alignment problems by calculating the proportion of a well aligned rectangular area. Therefore, two surfaces of different sizes but with the same shape are used for demonstration. Exemplary geometries for this calculation are given in Fig. 16 and the corresponding equation is presented in Eq. (16).

Here, l_x and l_y are the lengths of the statistically homogeneous rectangular area along the x- and y-directions, respectively. R_a represents the aspect ratio of the rectangular area, where $\Delta\, l_y$ and $\Delta\, l_x$ denote the displacement of the geometry along the x- and y-directions, respectively.

Assuming that the misalignment in x- and y- direction is equal ($\Delta l_x = \Delta l_y$), the proportion of the correctly aligned surface can be calculated by Eq. (16).

$$\frac{A_{aligned}}{A_{total}} = \frac{\max(0,\ l_x - |\Delta l_x|) \bullet \max(0,\ R_a l_x - |\Delta l_y|)}{R_a {l_x}^2} \tag{16}$$

For a given misalignment Δl in either direction, the well-aligned area scales with the absolute difference between the area's length l and the misalignment. This implies in particular, that the accurately aligned area of the phase with smaller grains or domains tends to decrease faster than that of the phase with larger grains or domains, as shown in Fig. 16b). In addition, the higher the aspect ratio, the faster the well-aligned area decreases for isotropic misalignment. For this reason,

microstructures with a multi-modal grain size distribution or high aspect ratios are challenging to correlate.

Methodological differences also need to be considered. Using the correlated EBSD and nano-indentation data of the meteorite in Fig. 17 as an example, it becomes apparent that a perfect correlation was not feasible, especially within the region containing thin γ_m seams, as some were partially not indexed by EBSD.

Additionally, the incompatibility of different spatial resolutions affects the correlation and needs to be considered. For example, the quantified e-ZAF EDS data of the Seymchan meteorite exhibited a relatively high degree of blur compared to the EBSD data due to binning for better e-ZAF quantification, as shown in Fig. 17c) and d). However, this can be effectively corrected by using improved equipment or acquisition parameters, as shown in Fig. 17e) and f). In addition, it could be that the correlation is less accurate when the point-to-point correlation is performed for fine structures or grain boundary regions. It is also necessary to take into account the intrinsic spatial resolution limitation of the elemental analysis due to the larger interaction volume of the characteristic X-ray emission compared to the backscattered electron emission.

In conclusion, the point-to-point correlation should ideally be performed either between data with similar spatial resolution or with appropriate data filtering methods to avoid erroneous correlations. In general, the observations and results of the two materials investigated in this study were analysed mainly to demonstrate the potential of the newly developed library rather than for scientifically accurate extraction of unknown elastic constants.

Despite the limitations encountered with respect to the fine, two-phase and textured meteorite microstructure, the combinatorial approach of the nano-indentation and the EBSD measurement can provide valuable insights. It was demonstrated that the high-speed NIT can elucidate the single crystal stiffness tensor without the need to solve the complex constitutive equations of the V-N model. As a result of the statistical advantage of high-speed NIT, a reliable estimation of the indentation moduli of low-index planes was possible. Therefore, this study presents further possibilities, such as the use of pre-compiled equation databases for other crystal systems, even if the numerical solutions for other crystallographic systems are not yet fully established.

5. Conclusions

Using a specifically developed point-to-point correlation method between nanoindentation, EBSD and EDS, it was demonstrated that the elastic stiffness tensor can be extracted from indentation data with good agreement between measurement and estimation. For this, we used two different materials, a single phase polycrystal with weak texture and a two-phase material with a strong texture as well as small features compared with the spatial resolution of the correlated measurements. This highlighted both the potential and the limitations of the approach, which are summarised as follows:

1. Using the correlation between the EBSD measurements and high-speed NIT experiments on a single phase austenitic steel demonstrated that the orientation-dependent indentation moduli could be fitted successfully using DFT data for pure iron as starting values.
2. In a second step, this enabled the estimation of the single crystal stiffness tensor based on the pre-solved equation parameters of the V-N model that showed good correspondence with other experimentally obtained single crystal stiffness tensor estimates.
3. Importantly, this analysis is possible without computationally expensive solving of constitutive equations underlying the V-N model.
4. In multi-phase materials with complex microstructures, difficulties are encountered, particularly where the uncertainty in alignment approaches the spatial resolution of the least accurate correlated measurement. However, appropriate filtering allows the extraction of correlated data from suitable regions of interest even if embedded in a microstructure that is ill-suited for correlative analysis as a whole.

Overall, the presented method therefore demonstrates great potential to derive more directionally sensitive elastic properties from indentation with relative ease in the future.

Declaration of Competing Interest

The authors declare that they have no known competing financial interests or personal relationships that could have appeared to influence the work reported in this paper.

Data availability

Data will be made available on request.

Acknowledgement

The authors gratefully acknowledge the Deutsche Forschungsgemeinschaft (DFG, German Research Foundation) for funding their project 406912286 (C-TRAM). This project has also received funding from the European Research Council (ERC) under the European Union's Horizon 2020 Research and Innovation Programme (Grant Agreement No. 852096 FunBlocks). The authors also thank the Scientific Center for Optical and Electron Microscopy (ScopeM), ETH Zurich, for access to its facilities. Additionally, the authors express their gratitude to Prof. Jörg F. Löffler and Dr. Indranil Basu for his assistance with the HR-EDS.

References

[1] J. Gong, A.J. Wilkinson, A microcantilever investigation of size effect, solid-solution strengthening and second-phase strengthening for< a> prism slip in alpha-Ti, Acta Mater. 59 (15) (2011) 5970–5981.
[2] W.C. Oliver, G.M. Pharr, Nanoindentation in materials research: Past, present, and future, MRS Bull. 35 (11) (2010) 897–907.
[3] Y.M. Arısoy, L.E. Criales, T. Özel, B. Lane, S. Moylan, A. Donmez, Influence of scan strategy and process parameters on microstructure and its optimization in additively manufactured nickel alloy 625 via laser powder bed fusion, Int. J. Adv. Manuf. Technol. 90 (5-8) (2017) 1393–1417.
[4] Britton, T., et al., *The effect of crystal orientation on the indentation response of commercially pure titanium: experiments and simulations.* Proceedings of the Royal Society A: Mathematical, Physical and Engineering Sciences, 2010. **466**(2115): p. 695-719.
[5] S. Das, F. Hofmann, E. Tarleton, Consistent determination of geometrically necessary dislocation density from simulations and experiments, Int. J. Plast 109 (2018) 18–42.
[6] M. Quaresimin, Modelling the fatigue behaviour of bonded joints in composite materials, in: Multi-scale Modelling of Composite Material Systems, Elsevier, 2005, pp. 469–494.
[7] H.N. Southworth, Scanning electron microscopy and microanalysis, in: A.W. Nicol (Ed.), Physicochemical Methods of Mineral Analysis, Springer US, Boston, MA, 1975, pp. 421–450.
[8] S.C. Schwarm, R.P. Kolli, E. Aydogan, S. Mburu, S. Ankem, Characterization of phase properties and deformation in ferritic-austenitic duplex stainless steels by nanoindentation and finite element method, Mater. Sci. Eng. A 680 (2017) 359–367.
[9] P. Tao, J.-M. Gong, Y.-F. Wang, Y. Jiang, Y. Li, W.-W. Cen, Characterization on stress-strain behavior of ferrite and austenite in a 2205 duplex stainless steel based on nanoindentation and finite element method, Results Phys. 11 (2018) 377–384.
[10] R. Li, et al., Anisotropy in the elasticity of α-U from first-principles calculations and nanoindentation, J. Nucl. Mater. 558 (2022), 153351.
[11] J.M. Wheeler, Mechanical phase mapping of the Taza meteorite using correlated high-speed nanoindentation and EDX, J. Mater. Res. 36 (1) (2021) 94–104.
[12] J.M. Wheeler, B. Gan, R. Spolenak, Combinatorial investigation of the Ni–Ta system via correlated high-speed nanoindentation and EDX mapping, Small Methods 6 (2) (2022), 2101084.
[13] M. Mejri, et al., Investigation of the mechanical properties of Mn15Si26 via EBSD-nanoindentation coupling and ab-initio calculation, J. Alloy. Compd. 900 (2022), 163458.
[14] C. Fizanne-Michel, M. Cornen, P. Castany, I. Péron, T. Gloriant, Determination of hardness and elastic modulus inverse pole figures of a polycrystalline commercially pure titanium by coupling nanoindentation and EBSD techniques, Mater. Sci. Eng. A 613 (2014) 159–162.

[15] J. Aspinall, D.E.J. Armstrong, M. Pasta, EBSD-coupled indentation: nanoscale mechanics of lithium metal, Mater. Today Energy 30 (2022), 101183.
[16] G. Nolze, Image distortions in SEM and their influences on EBSD measurements, Ultramicroscopy 107 (2–3) (2007) 172–183.
[17] C.M. Magazzeni, H.M. Gardner, I. Howe, P. Gopon, J.C. Waite, D. Rugg, D.E. J. Armstrong, A.J. Wilkinson, Nanoindentation in multi-modal map combinations: a correlative approach to local mechanical property assessment, J. Mater. Res. 36 (11) (2021) 2235–2250.
[18] J. Everaerts, C. Papadaki, W. Li, A.M. Korsunsky, Evaluation of single crystal elastic stiffness coefficients of a nickel-based superalloy by electron backscatter diffraction and nanoindentation, J. Mech. Phys. Solids 131 (2019) 303–312.
[19] J.J. Vlassak, W.D. Nix, Measuring the elastic properties of anisotropic materials by means of indentation experiments, J. Mech. Phys. Solids 42 (8) (1994) 1223–1245.
[20] F. Bachmann, R. Hielscher, H. Schaeben, Texture analysis with MTEX – Free and open source software toolbox, Solid State Phenom. 160 (2010) 63–68.
[21] L. Zou, Q. Zhou, Quantitative analysis of carbon in carbon steel using SEM/EDS followed by error correction approach, Microsc. Microanal. 19 (S2) (2013) 1048–1049.
[22] D. Van Niekerk, et al., Seymchan: a main group pallasite-not an iron meteorite, Meteorit. Planet. Sci. Suppl. 42 (2007) 5196.
[23] M.F. Doerner, W.D. Nix, A method for interpreting the data from depth-sensing indentation instruments, J. Mater. Res. 1 (4) (1986) 601–609.
[24] I.N. Sneddon, The relation between load and penetration in the axisymmetric Boussinesq problem for a punch of arbitrary profile, Int. J. Eng. Sci. 3 (1) (1965) 47–57.
[25] H. Gao, T.-W. Wu, A note on the elastic contact stiffness of a layered medium, J. Mater. Res. 8 (12) (1993) 3229–3232.
[26] C.-M. Cheng (Zheng Zhemin) Institute of Mechanics, Chinese Academy of Sciences, Beijing 100 080, People's Republic of China Y.-T. Cheng Physics and Physical Chemistry Department, General Motors Research and Development Center, Warren, Michigan 48090 On the initial unloading slope in indentation of elastic-plastic solids by an indenter with an axisymmetric smooth profile Applied physics letters 71 18 1997 1997 2623 2625.
[27] S. Marschner, et al., Fundamentals of computer graphics. (2018) 183–231.
[28] Ånes, H.W., et al., *pyxem/orix: orix 0.11.1*. Zenodo.
[29] Pedregosa, F., et al., *Scikit-learn: Machine learning in Python.* Journal of machine learning research. **12**(Oct): p. 2825-2830.
[30] Virtanen, P., et al., *SciPy 1.0: Fundamental algorithms for scientific computing in Python.* Nature Methods. **17**: p. 261-272.
[31] O. Kapikranian, et al., Point defect absorption by grain boundaries in alpha-iron by atomic density function modeling, Phys. Rev. B 92 (22) (2015), 224106.
[32] C. Zener, Ring diffusion in metals, Acta Crystallogr. 3 (5) (1950) 346–354.
[33] R. Hill, The Elastic Behaviour of a Crystalline Aggregate, Proc. Phys. Soc. A 65 (5) (1952) 349–354.
[34] W. Voigt, Lehrbuch der Kristallphysik (Textbook of crystal physics), BG Teubner, Leipzig und Berlin, 1928.
[35] A. Reus, Berechnung der Fliessgrenze von Mischkristallen auf Grund der Plastizitätsbedingungen für Einkristall, Z. Angew. Math. Mech. 9 (1929) 49–58.
[36] M. Laurent-Brocq, E. Béjanin, Y. Champion, Influence of roughness and tilt on nanoindentation measurements: A quantitative model, Scanning 37 (5) (2015) 350–360.
[37] H.M. Ledbetter Cryogenics Division, Institute for Basic Standards, National Bureau of Standards, Boulder, Colorado 80302 R.P. Reed Cryogenics Division, Institute for Basic Standards, National Bureau of Standards, Boulder, Colorado 80302 Elastic properties of metals and alloys, I. Iron, Nickel, and Iron-Nickel alloys Journal of Physical and Chemical Reference Data 2 3 1973 1973 531 618.
[38] G. Alers, J. Neighbours, H. Sato, Temperature dependent magnetic contributions to the high field elastic constants of nickel and an Fe-Ni alloy, J. Phys. Chem. Solid 13 (1–2) (1960) 40–55.
[39] D. Bower, E. Claridge, I. Tsong, Low-temperature elastic constants and specific heats of fcc nickel–iron alloys, physica status solidi (b) 29 (2) (1968) 617–625.
[40] D.E. Diesburg, The elastic constants of iron-nickel-carbon alloys, Iowa State University, 1971.
[41] N.G. Einspruch Texas Instruments Incorporated, Dallas, Texas L.T. Claiborne Texas Instruments Incorporated, Dallas, Texas Elastic Constants of a (73.8% Ni-26.2% Fe) Ferromagnetic Alloy Journal of Applied Physics 35 1 1964 1964 175 175.
[42] E. Goens, E. Schmid, Über die elastische Anisotropie des Eisens, Naturwissenschaften 19 (23–25) (1931) 520–524.
[43] M.W. Guinan, D.N. Beshers, Pressure derivatives of the elastic constants of α-iron to 10 kbs, J. Phys. Chem. Solid 29 (3) (1968) 541–549.
[44] R. Kimura, K. Ohno, On the elastic constants of single crystals of iron, Sci. Rept. Tohoku Univ. (1934) 359–364.
[45] Kimura, R.i., *On the elastic moduli of ferromagnetic materials. Part I. Dynamical measurements of the elastic moduli of iron crystals.* Nippon Sugaku-Buturigakkwai Kizi Dai 3 Ki, 1939. **21**(8-11): p. 686-706.
[46] J. Leese Metals Research Laboratory, Brown University, Providence, Rhode Island A.E. Lord Metals Research Laboratory, Brown University, Providence, Rhode Island Elastic stiffness coefficients of single-crystal iron from room temperature to 500° C Journal of Applied Physics 39 8 1968 1968 3986 3988.
[47] M.F. Markham, Measurement of elastic constants by the ultrasonic pulse method, Br. J. Appl. Phys. 8 (S6) (1957) S56–S63.
[48] J.A. Rayne, B.S. Chandrasekhar, Elastic constants of iron from 4.2 to 300 K, Phys. Rev. 122 (6) (1961) 1714–1716.
[49] C. Rotter, C.S. Smith, Ultrasonic equation of state of iron: I. low pressure, room temperature, J. Phys. Chem. Solid 27 (2) (1966) 267–276.
[50] K. Salama, G. Alers, Elastic moduli variations at the martensitic transformation of a Fe–Ni alloy, J. Appl. Phys. 39 (10) (1968) 4857–4859.
[51] Y. Shirakawa, et al., Elastic constants of Ni and Ni-Fe–fcc– alloys, J Japan Inst. Metals 33 (10) (1969) 1196–1202.
[52] M. Yamamoto, On the elastic constants of iron single crystals, J. Jpn. Inst. Met. 7 (1943) 346–348.
[53] K. Sangwal, Etching of crystals: theory, experiment and application, Elsevier, 2012.
[54] M. Wittwer, M. Seita, A machine learning approach to map crystal orientation by optical microscopy, npj Comput. Mater. 8 (1) (2022) 8.
[55] E.D. Hintsala, U. Hangen, D.D. Stauffer, High-throughput nanoindentation for statistical and spatial property determination, JOM 70 (4) (2018) 494–503.
[56] C.-H. Yu, K.-P. Lin, C.-S. Chen, Nanoindentation and indentation size effects: Continuum model and atomistic simulation, in: S. Schmauder, C.-S. Chen, K. K. Chawla, N. Chawla, W. Chen, Y. Kagawa (Eds.), Handbook of Mechanics of Materials, Springer Singapore, Singapore, 2019, pp. 759–794.
[57] S. Lee, M. Seehaus, PyXC, 2023, Available online: https://zenodo.org/record/8322342 (accessed on 1. September 2023).